Solution Processed PbS Quantum Dot Tandem Solar Cells

Author:
Gao, Yijun

Publication Date:
2020

DOI:
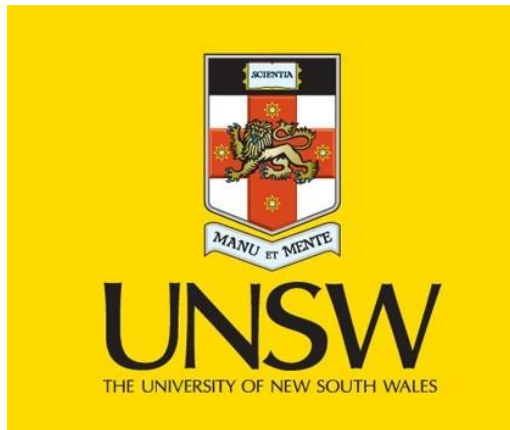https://doi.org/10.26190/unsworks/2083

License:
https://creativecommons.org/licenses/by-nc-nd/3.0/au/
Link to license to see what you are allowed to do with this resource.

UNIVERSITY OF NEW SOUTH WALES

SCHOOL OF PHOTOVOLTAIC AND RENEWABLE ENERGY ENGINEERING

Solution Processed PbS Quantum Dot Tandem Solar Cells

Author: Yijun Gao

Supervisors: Shujuan Huang & Robert Patterson

Co-supervisor: Gavin Conibeer

Thesis

(Engineering Postgraduate Research)

THE UNIVERSITY OF NEW SOUTH WALES
Thesis/Dissertation Sheet

Family name: Gao   First name: Yijun

Abbreviation for degree as given in the university calendar: PhD

School: Photovoltaic and Renewable Energy Engineering   Faculty: Engineering

Title: SOLUTION PROCESSED PBS QUANTUM DOT TANDEM SOLAR CELLS

Abstract 350wrods maximum: (PLEASE TYPE)

Colloidal quantum dot solar cells have drawn great attention in the past decade due to their easy synthesis, tunable bandgaps and low cost. However, the quantum dots' low absorbance together with limits placed on the thickness of the absorbing layer due to poor transport properties is hindering the development of quantum dot solar cells. In this research, for further developing quantum dot solar cells, a tandem solar cell strategy was utilised to address the above problem. A tandem solar cell stacks materials with different bandgaps to more efficiently convert the energy of a wider range of photons to electricity for higher solar cell efficiency.

This project developed high performance monolithic tandem solar cells based on PbS colloidal quantum dots. Firstly, single junction colloidal quantum dot cells were optimised as the building blocks of the tandem cells. $MgCl_2$ passivated ZnO-NP electron transporting layers were applied to improve single junction colloidal quantum dot cells by increasing both fill factor FF and short circuit current J_{sc}. Significant efficiency improvement has been observed based on single-junction PbS solar cells. Secondly, an optical modelling tool was created for the first time to simulate tandem colloidal quantum dot solar cells. This model could offer exact simulation on photon absorbance and current generation in tandem cells' functional layers. The model provided very instructive and quite essential guidance for designing the tandem cell structure and experimental works of fabricating quantum dot tandem cells. Thirdly, based on improved single-junction PbS solar cell and an established directive model, high performance tandem colloidal quantum dot solar cells were successfully fabricated with different interlayers of both Au and ITO. A graded band alignment employing both ZnO-doping and quantum dot size tuning has been applied to further improve tandem cell performance. Due to improved carriers extraction, this strategy successfully pushed the efficiency of a tandem quantum dot solar cell to be around 7%.

FOR OFFICE USE ONLY   Date of completion of requirements for Award:

THIS SHEET IS TO BE GLUED TO THE INSIDE FRONT COVER OF THE THESIS

Statement of Originality

'I hereby declare that this submission is my own work and to the best of my knowledge it contains no materials previously published or written by another person, or substantial proportions of material which have been accepted for the award of any other degree or diploma at UNSW or any other educational institution, except where due acknowledgement is made in the thesis. Any contribution made to the research by others, with whom I have worked at UNSW or elsewhere, is explicitly acknowledged in the thesis.

I also declare that the intellectual content of this thesis is the product of my own work, except to the extent that assistance from others in the project's design and conception or in style, presentation and linguistic expression is acknowledged.'

Signed: ……………………………………….

Date: ………………………………………

Copyright Statement

UNSW is supportive of candidates publishing their research results during their candidature as detailed in the UNSW Thesis Examination Procedure.

Publications can be used in their thesis in lieu of a Chapter if:

- The candidate contributed greater than 50% of the content in the publication and is the "primary author", ie. the candidate was responsible primarily for the planning, execution and preparation of the work for publication
- The candidate has approval to include the publication in their thesis in lieu of a Chapter from their supervisor and Postgraduate Coordinator.
- The publication is not subject to any obligations or contractual agreements with a third party that would constrain its inclusion in the thesis

Please indicate whether this thesis contains published material or not:

☐ This thesis contains no publications, either published or submitted for publication
(if this box is checked, you may delete all the material on page 2)

☐ Some of the work described in this thesis has been published and it has been documented in the relevant Chapters with acknowledgement
(if this box is checked, you may delete all the material on page 2)

☐ This thesis has publications (either published or submitted for publication) incorporated into it in lieu of a chapter and the details are presented below

CANDIDATE'S DECLARATION

I declare that:

- I have complied with the UNSW Thesis Examination Procedure

- where I have used a publication in lieu of a Chapter, the listed publication(s) below meet(s) the requirements to be included in the thesis.

Candidate's Name	Signature	Date (dd/mm/yy)

Copyright Statement

Signed: ……………………………………….

Date: ………………………………………

To my parents and my lovely family

ACKNOWLEDGEMENTS

When I start writing acknowledge part of my thesis, this means I have headed into the very ending part of my PbD stage. Doing a PhD is a process always full of challenges and difficulties. Fortunately, I could have obtained great help and support from my dear supervisors and a bunch of fellows.

Firstly, I would like to thank my primary supervisor Dr. Shujuan Huang who brought me into this exciting career. I can still remember the first time I met her when she was in a hurry but thankfully she was still willing to squeeze a few minutes for a talk with me. In the following period, she helped me making plans and revising plans. Every steps moving forward and progresses in my project were achieved under her guidance and were full of both of our endeavours. Every paper, conference draft, and all kinds of applications were revised by Shujuan multiple times. She is definitely a super supportive supervisor. Thank Shujuan for her great and warm help as well as her rich academic intelligence and experience again.

Then, I must thank my supervisor Dr. Robert Patterson for his tremendous help. Rob introduced me into the lab and he can explain all aspects of the project, from the very basic principles to the projected future applications. Rob is always good at explaining things, maybe the best I have ever met. No matter how complicated and obscure the issue is, Rob can help me figure it out. Rob's great patience is a virtue that rarely shown on others, which I admire very much. At quite a few key points of my project, Rob's opinions were very constructive for directing my research.

Also, I feel honoured to be supervised by Dr. Gavin Conibeer, a world renowned scientist. My every talk with Gavin was informative and illuminating to my study. His precise and foreseeing insight into a certain issue is quite impressive. His broad knowledge and extraordinary farsightedness provided me more than general guidance. My experience with Gavin will have a lifelong influence to me which I appreciate very much.

Besides, post-doctors Long Hu and Jianghui Zheng in our group provided solid skill support and Dr. Wejian Chen helped with data fitting work, for which I thank very much. Still, I am grateful for the help from my fellows Lin Yuan, Zhilong Zhang, Jianfeng Yang, Zhili Teh, Xin Cui, Stefan Tabernig and visiting fellows Yanmei Xu and Yang Li all together.

Lastly, working at SPREE that has a reputation at photovoltaic field is a quite unique experience and thank UNSW for its hospitable service to students.

ABSTRACT

Colloidal quantum dot solar cells have drawn great attention in the past decade due to their easy synthesis, tunable bandgaps and low cost. PbS quantum dot solar cell efficiency has developed from 3% in 2010[1] to 12.5% (Reported record in 2018)[2]. However, the quantum dots' low absorbance together with limits placed on the thickness of the absorbing layer due to poor transport properties is hindering the development of quantum dot solar cells. In this research, for further developing quantum dot solar cells, a tandem solar cell strategy was utilised to address the above problems. A tandem solar cell stacks materials with different bandgaps to more efficiently convert the energy of a wider range of photons to electricity to overcome the Shockley–Queisser limit.

This project developed solution processed monolithic tandem solar cells based on PbS colloidal quantum dots. Firstly, single-junction PbS quantum dot solar cells were investigated as building blocks for constructing tandem cells. $MgCl_2$ treated ZnO nanoparticle electron transport layers were applied to improve single-junction PbS quantum dot solar cells by increasing both fill factor FF and short circuit current J_{SC}. Significant efficiency improvement of 2% has been observed based on single-junction PbS quantum dot solar cells. Secondly, an optical modelling was performed to simulate PbS quantum dot tandem solar cells. This modelling could offer exact simulation on photon absorbance and current generation in tandem cells' functional layers. The modelling provided instructive and essential guidance for designing the tandem cell's structure. By this modelling, subcells' bandgaps, absorbing layers' thicknesses and interlayers' thicknesses were investigated and optimised for experimental fabrication of PbS quantum dot tandem solar cells. Thirdly, based

on improved electron transport layer and an established directive modelling, PbS quantum dot tandem solar cells were successfully fabricated with different interlayers of both Au and ITO. A graded band alignment employing both $MgCl_2$ treated ZnO nanoparticle electron transport layer and quantum dots with different bandgaps has been applied to further improve tandem cell performance. Due to improved carrier extraction, this strategy successfully pushed the efficiency of the PbS quantum dot tandem solar cell to around 7%.

The successful construction of PbS quantum dot tandem solar cell provides a solution for further developing PbS quantum dot based solar cells. The $MgCl_2$ treated ZnO electron transport layer can be more widely used on other single-junction as well as tandem solar cells. The optical modelling introduced in this research can be used to provide guidance for optical devices' design. The graded band alignment was firstly used on PbS quantum dot tandem solar cells, which shows effectiveness on improving the tandem cell's performance and hold a potential to be further applied on other kinds of tandem solar cells.

Table of Contents

List of Figures

List of Tables

Chapter 1. Introduction

For all human beings, global-warming is a common problem which has shown more intense influence in recent years on many regions on earth including but not restricted to polar areas. In the meantime, reducing carbon emission and developing green renewable clean energy have become world-wide aims and desires for sustainable human development and protecting the environment. For solving these problems, solar energy technology has been developed as an effective approach which could offer essentially unlimited clean energy for human long-term future. The sun continuously offers 173,000 terawatts (trillions of watts) of solar energy to earth and solar cells could convert this power to electricity at a certain power conversion efficiency (PCE) while, importantly, emitting zero carbon to the atmosphere.

Colloidal quantum dot (CQD) solar cells are a third generation solar cell technology which has shown its potential for reducing solar cell manufacturing cost and to further spread solar energy application and utilization. The in-solution processed material synthesis and room-temperature in-air processed cell fabrication provide potential for low cost manufacturing and future industrial commercialisation. The relatively high stability of PbS quantum dots over many other thin film solar cell material candidates is another important advantage of this kind of solar cell. In the past decade, PbS quantum dot solar cells have developed from power conversion efficiency of 3% in 2010[1] to 12.5%[2] (single-junction cell record reported in 2018).

Indeed, single-junction quantum dot solar cells have undergone significant development in the past ten years and drawn growing attention from both academic and industry due to quantum dots' unique properties including tunable bandgaps, solution-processed synthesis, low processing temperature and low material cost. Colloidal quantum dots are perfect candidate materials for making tandem solar cells not only because of their tunable bandgaps, which offer great convenience for tandem cell designation, but also because tandem cell strategy is a dedicated solution for quantum dot single-junction cells' fundamental problem of short diffusion length combined with the quantum dot films' poor absorbance.

However, the research for quantum dot tandem solar cells, which have greater potential to achieve a much higher efficiency, has lagged far behind its single-junction counterpart. A tandem cell utilises two subcells, responding to different solar spectrum ranges, connected in

series to boost the absorbance of a cell from solar irradiance, so that the thermalisation loss for a single-junction solar cell can be alleviated by applying a large bandgap front subcell while the transmission loss can also be much reduced by introducing a narrow bandgap rear subcell. Nonetheless, the fabrication of high performance solution processed thin film tandem cells is not nearly as developed as single-junction cells and remains much more challenging. The reasons for this are the limited temperature and solvent tolerance of thin film front cells during the subsequent interlayer and rear cell fabricating process, the difficulty in achieving subcells current matching and under-developed interlayer selection and design. This research tries to address these problems for quantum dot tandem solar cells and finally a working PbS quantum dot tandem solar cell with an efficiency of ~7% was achieved successfully.

1.1 Introduction to solar cells and colloidal quantum dot solar cells

1.1.1 Current solar cell development and potential limitation

Solar energy is the fastest developing type of clean renewable green energy, the development of which is especially beneficial for minimising the increasingly severe global-warming and emerging energy-crisis[3-12]. Solar cells are specially designed photovoltaic devices for converting sun-light energy into electrical energy.[13-20] Due to great contributions of researchers such as Shockley [21-23], Prince [24], Green [25, 26] and so on [27-30], a variety of photovoltaic technologies were invented [31-42] and successful commercialized[43-47]. A variety of cell structures has been developed based on different materials system such as Silicon, GaAs, organic polymers, perovskite and quantum dots. Figure 1-1(a-e) shows structures of these solar cells.

The current solar cell market is dominated by silicon based solar cells.[48] Commercial crystalline-silicon solar cells achieved an efficiency of >20%, while an all-back contacted silicon solar cell reached a lab efficiency record of 26.7%, which is approaching the theoretical limit of 29.4% for crystalline silicon cells.[49, 50] Recently, the previously high cost of solar cells has been significantly reduced to be competitive with the commercial market electricity price and mass production has been made realistic thanks to great efforts that previous and current generations of researchers and industry leaders have made.[51, 52]
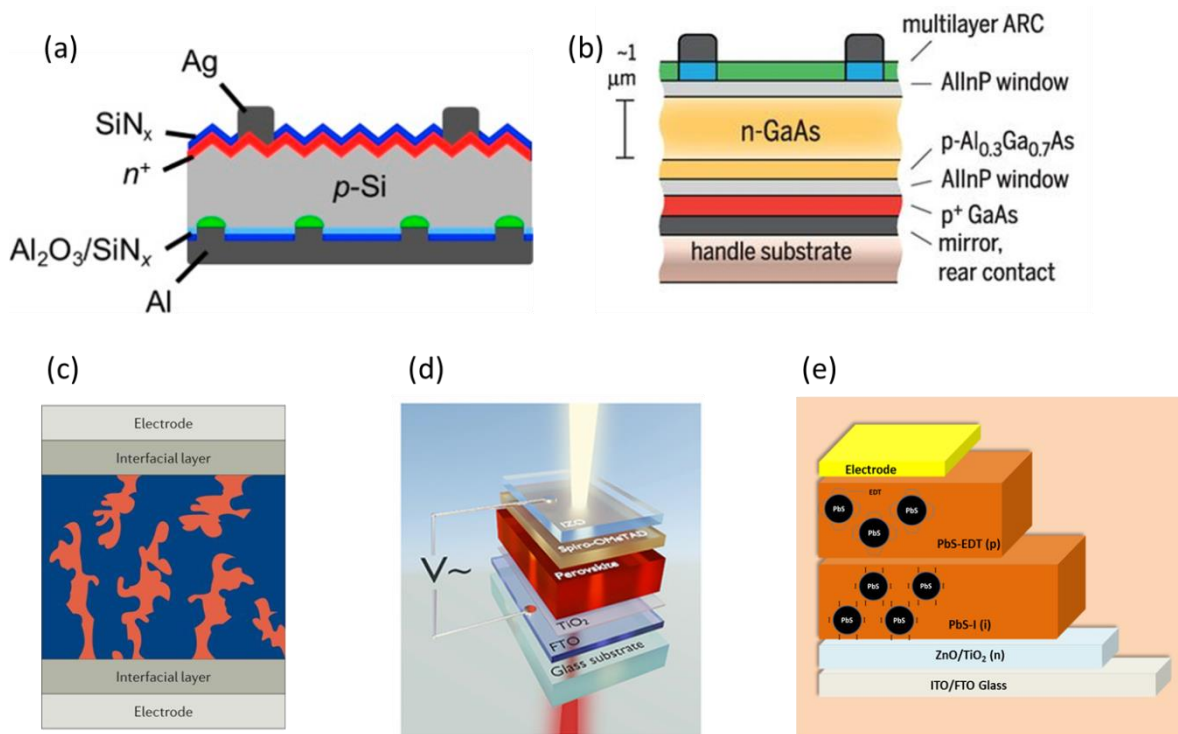
Figure 1-1 (a) Structure of Perc silicon solar cell.[53] (b) Structure of Alta GaAs solar cell.[54] (c) Structure of organic solar cell. The absorbing layer is composed of donor (blue) and acceptor (red) materials.[55] (d) Structure of perovskite solar cell.[56] (e) Structure of PbS quantum dot solar cell.

1.1.2 Advanced concepts in photovoltaics for high efficiency solar cells

To further improve solar cell performance, researchers have developed novel concepts such as multi-exciton-generation, up-conversion, tandem cells and hot carrier solar cells. Multi-exciton-generation (MEG) aims at generating two or more electrons by absorbing one high energy photon while up-conversion (UC) means combining the energy of two or more low energy photons to generate one high energy excited electron. The former tackles the carrier thermalisation loss while the latter tackles the transmission loss in a single-junction cell. The hot carrier solar cell aims at using selective contacts to drain out electrons and holes while they are still "hot", i.e. not being thermalised. Tandem solar cells combine two subcells with different bandgaps to form one cell, so that the trade-off between below bandgap loss due to a high bandgap and thermalisation due to a low bandgap can be broken. Ideally, high energy photons are absorbed in the subcell with the higher bandgap, thus experiencing less

thermalisation, and low energy photons transmitted to the subcell with a lower bandgap, thus enabling the device to harvest more photons.

Quantum dots have been viewed as ideal material for generating MEG effect, and this has been observed in a PbSe quantum dot material system with an EQE that reached 114%.[57] Graphene quantum dots have been reported to be able to produce up-conversion photoluminescence (PL). [58] Recent research shows that hot carrier thermalisation time can be largely extended by surface modification on PbSe quantum dots.[59]

Nonetheless the tandem solar cell is the only strategy for overcoming the Shockley-Queisser (S-Q) limit that has to date been realised by using III-V group compound. Epitaxial growth is a commonly used method for processing III-V group matreials.[60-63] A very high efficiency of 46.1% (at 312×AM1.5d) has been reported for a wafer-bonded GaInP/GaAs//GaInAsP/GaInAs solar cell grown on InP-engineered substrate.[64] The work in this thesis aims to take advantage of the tandem solar cell concept strategy to further develop low-cost solution processed quantum dot based tandem devices toward approaching and eventually overcoming the S-Q limit.

1.1.3 Colloidal quantum dot solar cells

The next generation solar cells with easily synthesised and low-cost new materials such as quantum dots, perovskite and polymer have been developed. Among these thin film solar cells, polymer solar cells are the earliest emerging kind of cell. The absorbing layer of a polymer solar cell is a blend of electron-rich and hole-rich organic semiconductors.[65] With their limited absorption, tandem organic solar cells have been studied extensively.[66, 67] Perovskite solar cells have achieved a fast development in recent years. With a super high efficiency, the stability of perovskite has also been improved in these years [68], but remains a concern.

Colloidal quantum dots (CQDs) are solution-processed nanocrystal semiconductors with a diameter smaller than the exciton Bohr radius. CQD solar cells possess three unique advantages: tunable-bandgaps, facile-synthesis and low-cost. The problem for this material is the small diffusion length limiting absorbing layer thickness, which can be solved by utilising a tandem cell structure.[67] Quantum dot solar cells, the topic of this thesis, take advantage of

the quantum confinement effect to create bandgaps in materials. Different ligands are used to form n- and p- type quantum dots, leading to tunable properties for functional layers and design flexibility for making solar cells. Colloidal quantum dot solar cells are also developing swiftly with efficiency increasing from 3% to 16.6% (NREL's efficiency chart at https://www.nrel.gov/pv/cell-efficiency.html) in less than ten years and have drawn great attention because of the unique properties of quantum dots, namely tunable bandgaps, in-solution easy synthesis and much lowered fabrication cost. Hence, the unique properties and solution processed synthesis of quantum dots indicate a very promising future for a wider application in solar cells.

However, the efficiency of all these solar cells is bound by the Shockley-Queisser limit. Shockley-Queisser limit means that single-junction solar cell efficiency cannot reach above 33.7% even if the optimal bandgap is chosen and a perfect absorbing material can be made.[69] The reasons for this limit are that only photons with energy higher than the bandgap can be absorbed by semiconducting absorbing materials leaving unabsorbed photons transmitted and that charge carriers generated by absorbed photons far above the bandgap energy experience thermalisation which creates another portion of energy loss. In the meantime, bandgaps of CQD solar cells can be tuned by simply adjusting the nanocrystal size, allowing a bandgap range from 0.4 eV to 1.6 eV[70-72], which provides extreme flexibility for designing high performance tandem cells. Both synthesis and cell fabrication for this material are performed with an in-solution process. The facile-synthesis of quantum dots not only makes the cell fabrication easier but also offers potential for further reducing costs for commercial manufacture.[73]

1.2 Motivation for developing tandem PbS quantum dot solar cells

Currently, achieving a higher efficiency is a common goal for the whole solar cell research field and having a reduced mass production cost is a globally preferred scenario at the same time. As introduced above, a tandem cell structure is designed to achieve a much higher efficiency than single-junction cells, meanwhile, solution-processed room-temperature-fabricated quantum dots could achieve a much reduced production cost. So tandem quantum dots solar cell combining the tandem cell concept for high efficiency and quantum dot material for reducing cell fabrication cost is very promising for satisfying current high

efficiency and low cost demand in industry and research at the same time. In light of this, quantum dot tandem solar cells (and its single-junction counterparts) [74] are very appealing third-generation photovoltaic materials with low-cost and facile-synthesis and promising high-efficiency potential. Moreover, for the realistic consideration for solar cell development, quantum dot tandem solar cells, utilising quantum dots' solution processability, not only solves the short diffusion length problem for quantum dots, but also becomes a promising way toward a higher efficiency for quantum dot based solar cells.

Though tunable bandgaps and facile synthesis make CQDs perfect candidates for a multi-junction cell, only a few reports have been targeting quantum dot tandem solar cells [75-77]. Quantum dot tandem solar cells' efficiency has lagged far behind its single-junction counterpart. The reasons for this are the limited temperature and solution tolerance of thin film front cells, difficulty to achieve subcell current matching and the intricate interlayer selection and design. This research tries to address these problems for quantum dot tandem solar cells and finally a monolithic quantum dot tandem solar cell was achieved successfully.

1.3 Thesis outline

1. In Chapter 1, a broader background and motivation behind this research are introduced. This part introduced a broad background about quantum dot tandem solar cell, described current solar cell research field where solar cells with high efficiency potential and low cost fabrication are desired, and quantum dot tandem solar cells could meet these requirements once for all. Multiple motivations for developing quantum dot tandem solar cells are also explained in chapter 1.

2. Chapter 2 presents a comprehensive literature review on the development of single-junction quantum dot solar cells and quantum dot tandem solar cells. It covers the colloidal quantum dot synthesis methods, single-junction CQD cell fabrication and multi-junction CQD solar cell fabrication.

3. Chapter 3 introduces an important fundamental work of improving single-junction cell for making quantum dot tandem solar cells. In this part, $MgCl_2$ passivated ZnO-NP electron transport layer was developed for improving single-junction cell performance. UPS, XPS, XRD, Raman-PL, FT-IR, UV-vis and SEM were used for

characterising the treated electron transport layer. The single-junction cell's performance was increased due to both increased J_{SC} and FF.

4. Another important foundation work of modelling for quantum dot tandem solar cells is illustrated in chapter 4. In this part, an optical modelling was performed for simulating tandem colloidal quantum dot solar cells. Assisted by this model, the influences of absorbing layer bandgaps and thicknesses as well as interlayer thicknesses on tandem cell performance were investigated for designing and optimising quantum dot tandem solar cell structure. Optimal values for absorbing layer bandgaps and thicknesses and interlayer thicknesses are suggested in this chapter. The model provided instructive and essential guidance for designing the tandem cell structure.

5. Chapter 5 reports on the successful fabrication of PbS quantum dot tandem solar cells based on the fundamental preparatory works described in chapter 3 and 4. PbS quantum dot tandem solar cells with different interlayers of both Au and ITO were fabricated and investigated. For the first time, a graded band alignment strategy was applied to further improve the performance of the PbS quantum dot tandem solar cell. Finally, a monolithic quantum dot tandem solar cell with power conversion efficiency around 7% was fabricated in this research.

6. Chapter 6 summarises the whole research and draws conclusions for the thesis. This part points out a few aspects that can be further studied and the main challenges for further studying quantum dot tandem solar cells. Based on this chapter, more research directions are suggested and are listed in the last part and a blueprint was drawn for the future of quantum dot tandem solar cells.

Chapter 1
Background and Motivation

Chapter 2
Literature Review

Chapter 3
Single-junction CQDs solar cells

Novelty 1: MgCl$_2$ dopted ZnO electron transporting layer was introduced.

Chapter 4
Modelling and optimisation of tandem cell structure

• Tandem cell with Au interlayer
• Tandem cell with ITO interlayer

Novelty 2: Optical modelling was established for guiding the design for tandem PbS quantum dot solar cells.

Chapter 5
Fabricating high performance tandem CQD solar cells

• Tandem CQDs solar cell with Au interlayer

• Tandem CQDs solar cell with ITO interlayer

Novelty 3: A graded band-alignment strategy was introduced for developing tandem cell performance.
Novelty 4: A simplified ITO interlayer was introduced.

Chapter 6
Conclusion and future work

Figure 1-1 Brief outline of the research contents and novelties for this thesis.

Chapter 2. Literature Review

In this chapter, a thorough literature review is conducted covering the whole manufacturing process from synthesising colloidal quantum dots (CQDs), fabricating single-junction CQD solar cells to constructing CQD tandem cells. The current situation of quantum dot solar cells and the development history are both reviewed. With a general review of all kinds of quantum dot materials, this chapter mainly focuses on reviewing PbS quantum dots which are the most widely studied QD material and are also the absorbing materials in this tandem cell research. Figure 2-1 is a road-map of this review showing the main aspects reviewed in this chapter.
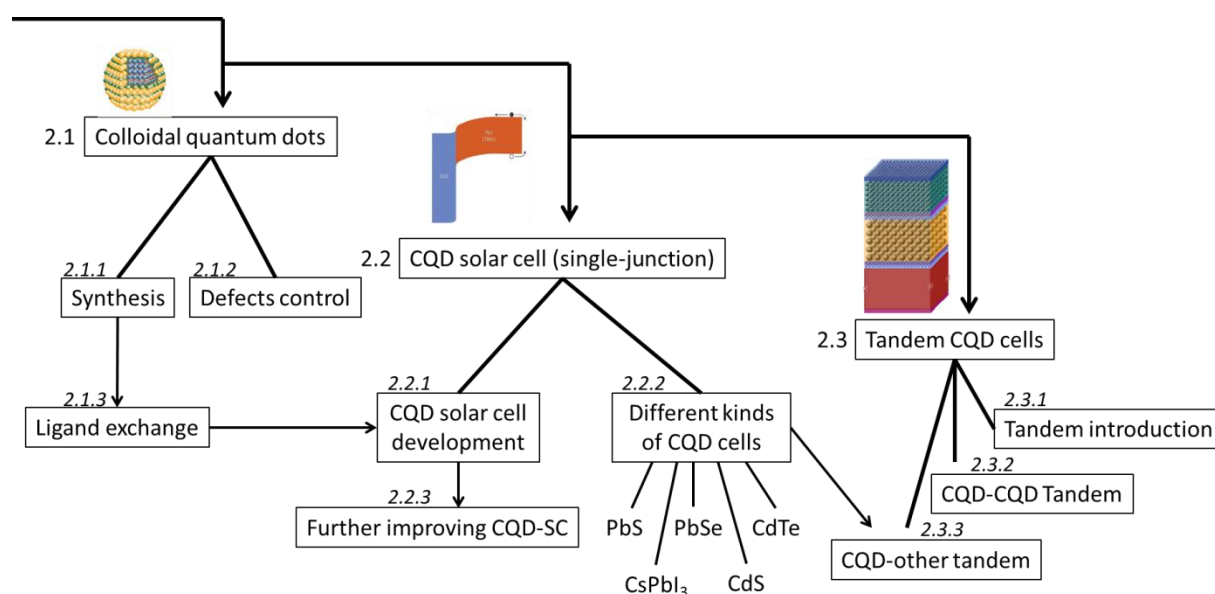
Figure 2-1 Literature review road-map. It shows reviewed aspects of colloidal quantum dots, single-junction CQDs solar cell and tandem CQD solar cells and relationships between those aspects.

2.1 Solution-processed CQDs for developing solar cells

Colloidal quantum dots are artificially manufactured semi-conductive clusters of atoms confined within the exciton Bohr radius. Solution-processed synthesis and tunable bandgaps have made colloidal quantum dots widely-used in many fields [78-84] such as photovoltaics, light-emitting diodes and photo detectors. The unique property of tunable bandgaps drives from quantum confinement effect, which means when the size of a nanocrystal is smaller than its exciton Bohr radius, the movement of electrons is confined and the energy spectrum becomes discrete.[85] For quantum dot based solar cells, the quantum dot's quality is a critical factor for single-junction and multi-junction photovoltaic devices to approach a higher performance. The quality of quantum dots is determined by quantum dot synthesis and purification processes which have been greatly improved these years leading to the highly mono-dispersed well-passivated quantum dots nowadays.

A typical colloidal quantum dot is usually composed of a crystal core and surface ligands (Figure 2-1-1 shows a scheme for a PbS quantum dot). Ligands (also known as surface-surfactants) are usually long chain or short chain molecules which could passivate as-synthesised quantum dots by passivating dangling chemical bonds on the quantum dot surface. The ligands usually consist of a hydrophilic head and a hydrophobic tail (such as the long chain ligand of oleic acid, oleyl amine) [86, 87] which contains a hydroxide hydrophilic head and a long carbon chain based hydrophobic tail. Such a structure enables quantum dots to be passivated by ligands and the quantum dots with surface ligands are able to disperse uniformly in hydrophobic solutions. Long ligands are usually exchanged by short ones (such as MPA [88], EDT [89]) in the cell-making process, which is reviewed in the following parts in this chapter.
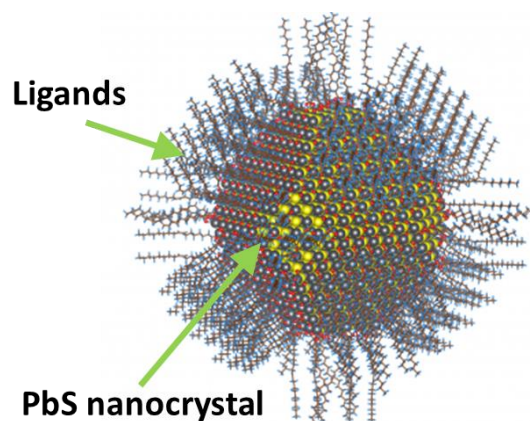
Figure 2-1-1 A scheme of a PbS colloidal quantum dot (Picture copyright from Oak Ridge National Laboratory, https://www.olcf.ornl.gov/2015/05/05/demystifying-quantum-dot-conundrums/). A typical quantum dot is usually composed of a crystallised core and passivating ligands. The ligands usually can be oleic acid, oleyl amine or hydroxyl ligands. The size of a quantum dot is confined within its exciton Bohr radius.

2.1.1 Synthesis development for high quality quantum dots

For making high-quality quantum dot solar cells, high-quality colloidal quantum dots are a necessary prerequisite. The currently prevailing method for achieving high quality quantum dots is the hot-injection method. The hot-injection method is illustrated in Figure 2-1-2(a). A two-step reaction is involved in this synthesis process [90-92]. Firstly, the sulfur source precursor is hot-injected into a solution containing lead source with a pre-settled reaction temperature. In this stage, a nucleation reaction occurs, rapidly forming uniform quantum dot nuclei. A focusing model [93] can explain the reaction in this stage. In this stage, the concertation of ligands (such as Oleic acid ligands) needs to be controlled as it affects the quantum dot size. When the concentration of ligands is high, the critical size for forming quantum dots is small, (The critical size is the smallest size for a nanocrystal to grow-up stably.) more and smaller size quantum dots would form.[94] In contrast, when a low ligand concentration is applied, the critical size is larger, small nucleis could not exist stably while only large quantum dots could form, so large size quantum dots are formed. The pre-settled injection temperature is also critical as different injection temperatures lead to quantum dots with different crystal sizes.[71, 94] A lower reaction temperature produces smaller quantum dots with larger bandgaps.[71, 94, 95] Secondly, growth happens following the rapid nucleation. Prolonging the growth time[71] in

this stage could also adjust the size of synthesised quantum dots. In addition, a heat-up method shown in Figure 2-1-2(b) is also an optional way to obtain quantum dots via heating a precursor solution continuously[96, 97].
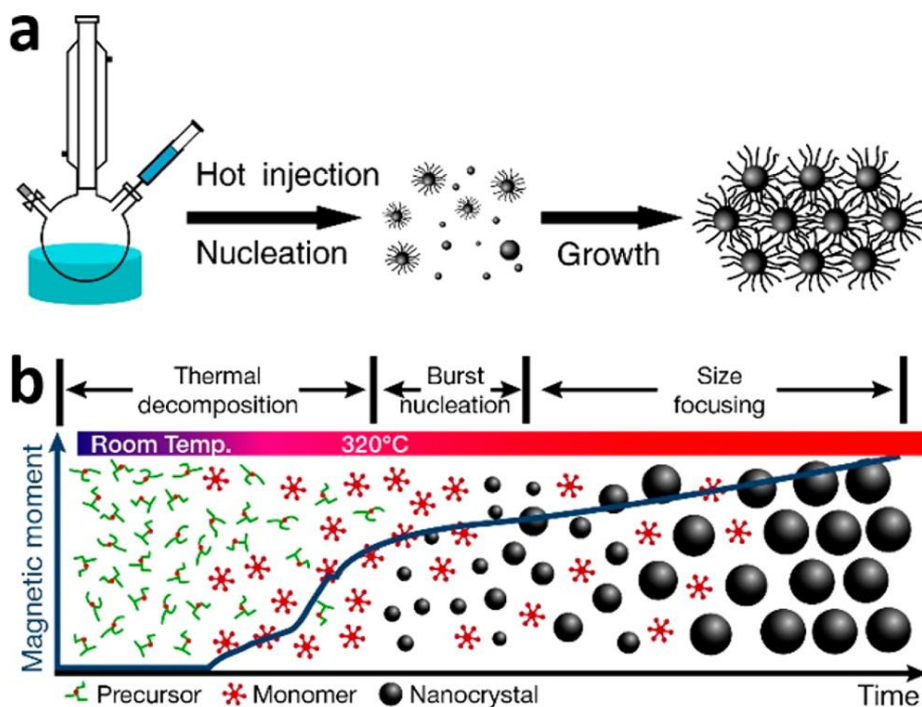
Figure 2-1-2 Synthesis methods for colloidal quantum dots [97] (a) Illustration of the hot-injection method for synthesising colloidal quantum dots. (b) The heating-up method for synthesising colloidal quantum dots.

For the widely used hot-injection method for PbS quantum dots, currently there are two synthesis routes available. The first route is based on lead oleate reacting with bis(trimethylsilyl)- sulfide in octadecene (referred to as the Hines synthesis from here on).[98] This offers monodispersed quantum dots over a wide size range (2.6-7.2 nm, corresponding to an absorption peak of 825-1750 nm). Figure 2-1-3 shows the absorbance and TEM images of the synthesised quantum dots. One thing worth a note is that post-synthesis self-narrowing of the particle size distribution was observed in Hines' research. With storing the synthesised quantum dots sample in the dark sealed in a cuvette for a period, the exciton peak blue-shifts and sharpens, suggesting a narrowing of the size dispersion and a decrease in average particle size. Figure 2-1-3(d) shows the absorbance of the sample stored at different time period and TEM images before and after storing are shown in Figure 2-1-3(e, f).
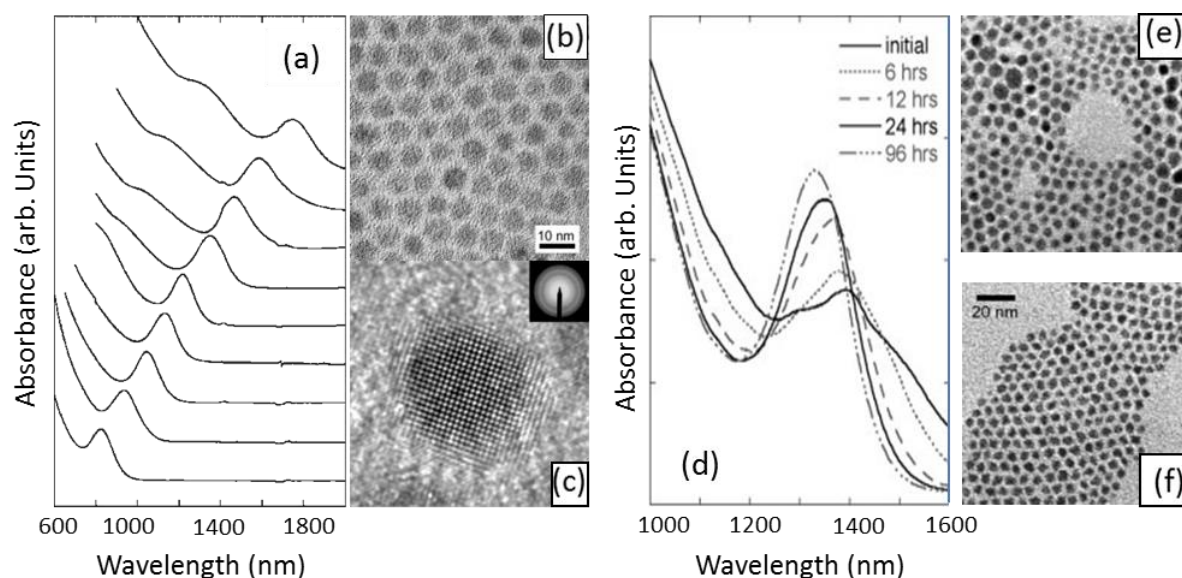
Figure 2-1-3 Absorbance and TEM for PbS quantum dots.[98] **(a) Absorption spectra spanning the range of tunable sizes with absorbance peak ranging from 825 nm to 1750 nm. (b) TEM images of colloidal PbS nanocrystals. (c) HRTEM images of colloidal PbS nanocrystals. (d) Absorption spectra of of PbS nanocrystals stored in toluene solution measured at time intervals spanning up to 96 h. The spectral evolution indicates a post-synthesis self-focusing of the size dispersion. (e,f) TEM images of the nanocrystal solution taken initially (e) and after 24 h storage (f).**

The second route employs lead chloride ($PbCl_2$) and elemental sulfur (S) in oleylamine (OlAm) as precursors and OlAm as the solvent (Cademartiri synthesis).[99] Moreels et al [71] modified this synthesis by incorporating tri-n-octylphosphine (TOP). A much enlarged range of quantum dot size (3-10 nm) can be obtained by this modified method and the available bandgaps span from 1.34 eV (925 nm) to 0.59 eV (2100 nm). Quantum dots with their peak absorption below 1200 nm and above 1600 nm were obtained with the assistance of TOP. In addition, a simple purification process was introduced in Moreel's research. By adding a small amount of ethanol (EtOH) to the suspension of PbS quantum dots until precipitation starts, the large clusters can be efficiently removed and the size-dispersion can be much narrowed. Figure 2-1-4 shows the absorption spectra of quantum dots synthesised with this approach and the TEM images of quantum dots before and after size-selection.
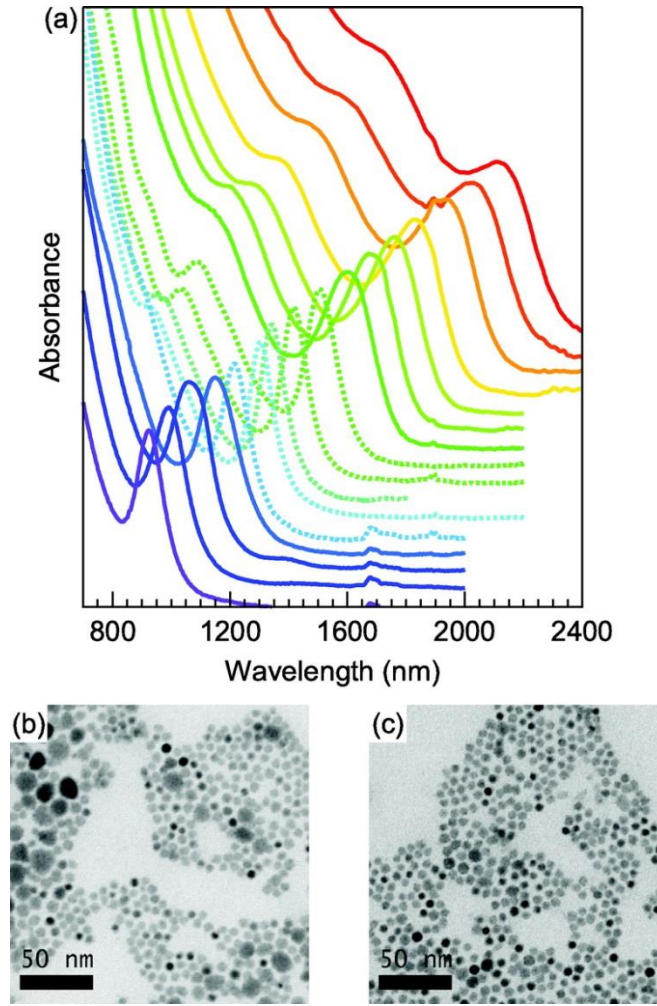
Figure 2-1-4 Absorbance spectra and TEM images of PbS quantum dots.[71] (a) Typical absorbance spectra of PbS quantum dot suspensions. Full lines are quantum dots synthesized with TOP, while dotted lines are those without TOP. (b,c) TEM images of typical PbS quantum dots before (b) and after (c) size-selective precipitation.

By adjusting the size of nanocrystals during the synthesis process, bandgaps of quantum dots can also be tuned and controlled [71, 100-102]. The relationship between bandgap and size of PbS quantum dots can be described by an empirical equation (1) introduced by Moreels et al[71].

$$E_0 = 0.41 + \frac{1}{0.0252d^2 + 0.283d}$$ (2-1)

In this equation, d is the diameter of a quantum dot (in *nm*) while E_0 is the width of the bandgap (in *eV*).

In order to understand the mechanism of quantum dot synthesis, models have been established that provide explanations for quantum dot formation at different stages of nucleation and growth. For now, different stages need to be explained separately by different models. Based on a diffusion-controlled growth assumption, a focusing model [93, 103, 104] was established which could offer an effective explanation for the nucleation stage. In the meantime, a defocusing model [105, 106] can explain the growth stage, which is also recognised as Ostwald ripening. Introducing those models helps understanding and then developing a quantum dot synthesis procedure for obtaining highly monodispersed colloidal quantum dots.

After synthesising quantum dots, a purification process needs to be introduced because the residues of precursors and impurities would decrease the performance of solar cells[107-109]. The purification can be conducted by performing solvent and anti-solvent treatments. The purification process is usually repeated multiple times for a higher purity. However, too extensive purification (i.e. repeating the washing process too much times) would cause PL reduction as ligands can be lost with too much solvents [110]. The PL reduction can be compensated by restoration of lost ligands [111, 112]. Effects of ligands and ligand exchange are reviewed in detail in the following section.

2.1.2 Ligand Exchange in solar cell fabrication

Ligand exchange is usually performed on synthesised quantum dots for making solar cells or other kinds of optoelectronic devices.[113-118]

In most cases, long-chain ligands need to be exchanged by shorter ligands for making optoelectronic devices. For example, in the typical PbS quantum dot synthesis, the ligands of oleic acid with a long carbon chain tail could indeed keep quantum dots stabilised in solution, however, these long ligands are also insulators between quantum dots which would hinder electron transport from dot to dot when those quantum dots are used in a solar cell. Hence, exchanging these long chains with shorter conductive ligands is a necessary step for quantum dot based solar cells to exhibit the high conductivity necessary for a high performance.[119-126]

One of the major reasons for ligand exchange is that a shortening distance between quantum dots are desired for achieving a high conductivity.[127] To achieve a high conductivity through ligand exchange, short ligands such as chalcogenide complexes and halides have been

extensively studied. Figure 2-1-5(a) shows the relationship between ligand length and spacing between quantum dots. With the carbon unit number n increasing from 2 to 10, the distance between quantum dots increases according to integrated GISAXS measurement. The advantage of metal chalcogenide complexes as ligands is that a full exchange of ligands can be achieved, leading to increased conductivity [128-134] as indicated in Figure 2-1-5(b). These studies provide a competing pathway to achieve ligands that lead to both high conductivity and hence high photovoltaic efficiency.[94] Meanwhile, halides, as atomic ligands, can provide solution-processed room-temperature ligand exchange leading to both increased conductivity and an increased quantum yield.[135-139] Besides, perovskite has been studied as ligand recently and its application on PbS quantum dots has shown its effectiveness for surface passivation and maintaining the cell stability under constant illumination.[140-142]
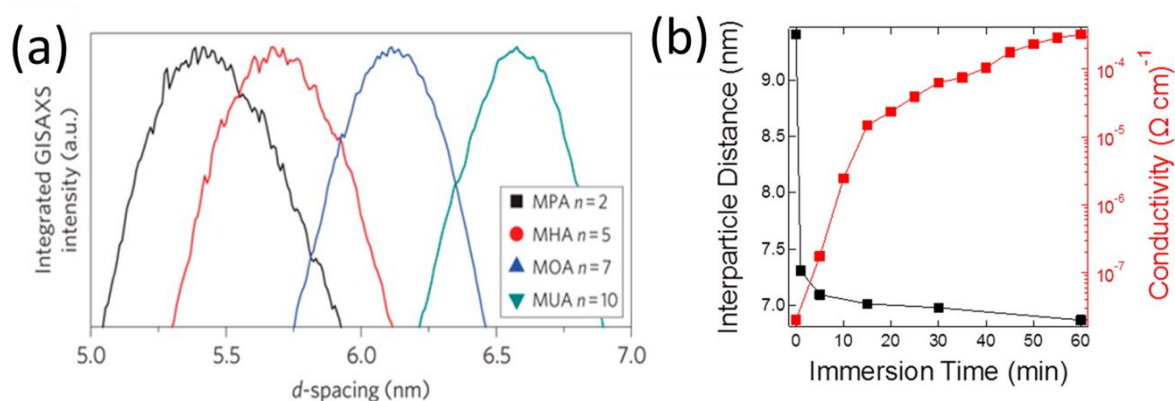
Figure 2-1-5 (a) Relationship between ligand length and inter PbS quantum dot spacing.[140] The organic ligands applied are 3-mercaptopropionic acid (MPA, HS(CH$_2$)$_2$COOH), 6-mercaptohexanoic acid (MHA, HS(CH$_2$)$_5$COOH), 8-mercaptooctanoic acid (MOA, HS(CH$_2$)$_7$COOH), and 11-mercaptoundecanoic acid (MUA, HS(CH$_2$)$_{10}$COOH). As the carbon unit number n increases, d-spacing between quantum dots increases. (b) Relationship between inter-particle distance and conductivity based on PbSe CQDs.[134] As inter-particle distance increasing, the conductivity increases significantly.

A second reason for performing ligand exchange is that surface-passivation is an important criterion for high performance solar cells which can be achieved by applying well-passivating ligands. High quality ligands should show effectiveness on passivating surface dangling-

bonds on quantum dots which can create detrimental traps and can act as highly efficient carrier recombination centres. The high surface-to-volume ratio of quantum dots makes passivating quantum dot surfaces a very important task as a large amount of traps tends to dominate solar cell performance. Mercaptopropionic acid (MPA), ethanedithiol (EDT) and halide atoms are successfully developed quantum dots surface passivators [89, 143, 144] which are quite extensively applied on solar cells. Highly passivated quantum dots can be realised by using these ligands which not only show passivation effects but also increased dot-to-dot conductivity.[145]

A third reason is that adjusting surface ligands can impact the energy levels of a quantum dot, leading to n-type or p-type behaviours.[146] Currently the n-type PbS quantum dots are obtained mainly using iodine ligands [147-149], while p-type quantum dots can be made by applying organic ligands [146, 150-152] such as ethanedithiol [152].

Current primary ligand exchange methods are solid-state ligand exchange and solution-phase ligand exchange. Figure 2-1-6 illustrates these two methods. For solid-state ligand exchange, a layer of CQDs with original long ligands is coated on an indium-doped tin oxide (ITO) or fluorine-doped tin oxide (FTO) substrate at first[153, 154], followed by applying a solution containing short-chain ligands in an optimised concentration on the as-coated quantum dot layer. The ligand-exchanged film is rinsed by harmless solvents for numerous times to remove the residual ligand molecules. Solid-state ligand exchange provides very efficient exchanging and facilitates high performance thin film devices [155] and there is more design freedom in solid-state exchange as well.[156] For example, each layer's quantum dot size and ligand type can be designed for achieving specific band off-set such as a graded band structure. Solution-phase ligand exchange is still a developing method compared to solid-state ligand exchange. In solution-phase ligand exchange, quantum dots with long ligands are mixed with short ligands in solution with the whole exchange process conducted in solution. After purification of ligand-exchanged quantum dots in solution, quantum dots with short ligands are spin-coated layer-by-layer directly to substrates without any further solid state process. The advantage of solution-phase exchange is that it could facilitate a more complete surface-passivation and that it greatly simplifies the solar cell manufacture process[144]. A recent work on one-step solution phase ligand exchange for PbS CQD solar cells has shown that an optimised spacing between quantum dots using 2D-matrix spacing improves quantum dot solar cell performance.[157]
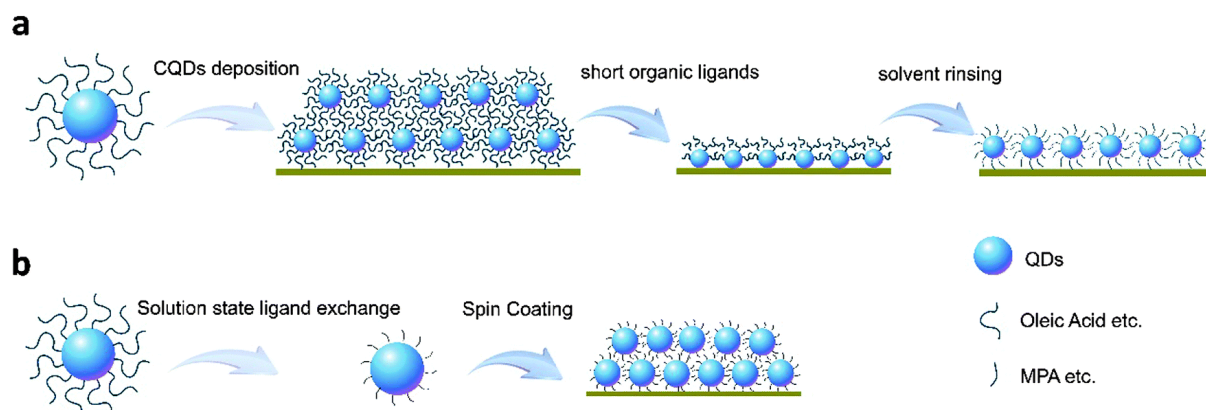
Figure 2-1-6 Illustration for (a) solid-state ligand exchange method and (b) solution-phase ligand exchange method.[156] For solid state ligand exchange in (a), the as-synthesised CQDs with long ligands are firstly spin-coated onto the substrate, then the spin-coated film is immersed into short ligand solution, where short ligands replace long ligands to form new surface passivation on quantum dots. After rinsing and drying the ligand exchanged film a quantum dot absorbing layer can be obtained. Usually this process is performed multiple times to obtain a desired film thickness. For solution state ligand exchange in (b), the ligand exchange process is performed by mixing the quantum dot (with long ligands) solution with short ligand solution, precipitating ligand exchanged quantum dots by adding anti-solvent and centrifuging, then directly spin-coat CQDs with short ligands onto the substrate to form a film. Thickness control can be realised by adjusting spinning speed and acceleration.

2.1.3 Defect control for developing high performance CQD solar cell

As discussed above, due to the high surface-to-volume ratio of quantum dots, surface defects can dominate solar cell performance. This is an issue worth addressing specifically. For dealing with this high defect density problem, theories explaining defect formation and nature have been developed widely in recent years.[158-163] Strategies for controlling defects have also been studied extensively.

Numerous studies have been conducted for understanding possible PbS CQD surface defect formation mechanism. Li et al [158] pointed out that dangling lead bonds on the quantum dot surface are mainly responsible for defect states forming in quantum dot absorbing layers. Another research further pointed out that for a PbS quantum dot crystal, facets (111) and (100) are primarily dominating the surface states of nanocrystals, where excess-Pb (111) facets could exhibit obvious non-stoichiometric effect, which would lead to excess charges which could be the main origin of in-gap defects.[159-162] Those defects could perform as efficient recombination centres and cause decrease in both carrier mobility and carrier lifetimes [162] as shown in Figure 2-1-7.[163] Hence, reducing quantum dot surface defects increases V_{OC}, J_{SC} and FF for quantum based solar cells at the same time, leading to a much improved solar cell performance[164].
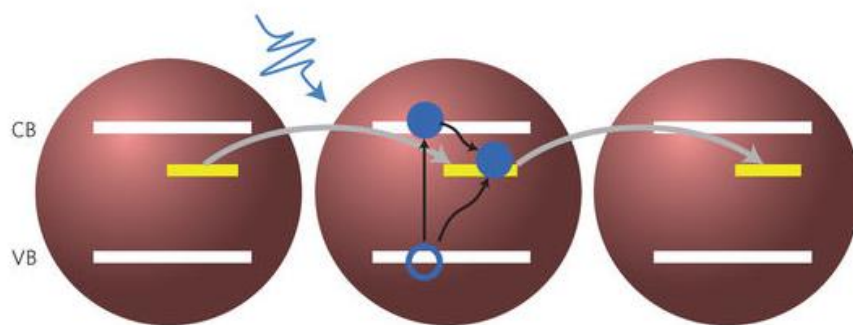
Figure 2-1-7 A scheme of recombination centres.[165] Mid-gap defects perform as recombination centres which leads to both reduced carrier mobility and lifetimes.

A series of strategies for eliminating surface mid-gap states have been investigated broadly. Introducing more efficient ligands [86, 166-170] (such as metal chalcogenide complex and halogen atoms) onto the nanocrystal surface has shown improvements on solar cell efficiency by reducing surface defects and increasing carrier diffusion lengths [167, 171]. In addition, solution-phase passivation has attracted attention recently, by which iodine element solution-phase ligand exchange has led to a certified record efficiency at 12.5% by passivating surface defects effectively.[172] Furthermore, atomic as well as hybrid ligand passivation approaches both provide optional and efficient strategies for substantially reducing surface defects and

effective surface passivation.[173-175] A scheme illustrating the density of states (DOS) before and after eliminating mid-gap states is shown in Figure 2-1-8.
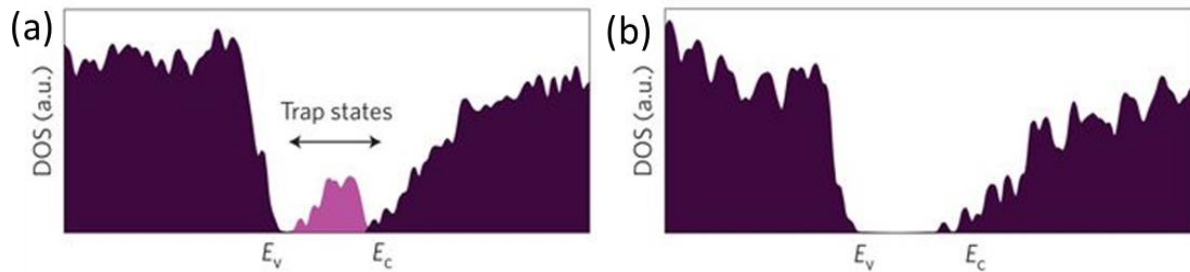
Figure 2-1-8 Density of states (DOS) before (a) and after (b) quantum dot surface passivation.[173] Traps states (a) sit right in-between bandgaps performing as detrimental recombination centres and can be eliminated (b) by surface passivation.

2.2 CQD solar cells

Due to the unique material properties of colloidal quantum dots (e.g. tunable bad-gaps, facile synthesis and low-cost), CQD solar cell efficiency has developed rapidly, on average, 1.1% per year (16.6% certified record in 2018, referring to NREL's efficiency chart at https://www.nrel.gov/pv/cell-efficiency.html) since the first successful CQD solar cell fabrication in 2005 [176]. This section illustrates the CQD solar cell development history, the most recent development strategies and various currently developed kinds of single-junction quantum dot solar cells.

2.2.1 PbS CQD solar cell development (structure evolution)

In 2005, Sargent et al [176] first applied quantum dots in a polymer solar cell to extend the width of the absorbed spectrum, which opened the gate for investigating quantum dots as photovoltaic absorbing materials. This solar cell employed a Schottky structure, where CQD-sensitised polymer was chosen as absorbing layer while ITO and metal magnesium were electrode contacts sandwiching the CQD-polymer composite. Soon enough, a solar cell employed pure quantum dots as absorbing layer and showed considerable efficiency

(~1%).[177] Inspired by this achievement, Schottky structured CQD solar cells were extensively studied by alternating the metal contacts [178-183] and the efficiency developed from 1.3% to 4.2%. A scheme of a Schottky quantum dot solar cell is shown in Figure 2-2-1.[184] In this work, Loi et al [184] used a post-synthesis "washing" treatment to develop the cell efficiency to 5.2%. Indeed, Schottky structure CQD solar cells have certain advantages such as easy-fabrication and fewer interfaces which potentially reduce the opportunities for interface defects. However, there is an intrinsic limitation in the Schottky CQD cell structure [185] due to fermi-level-pinning in the metal interface which could significantly suppress solar cell performance and a much lower voltage caused by a small depletion the amount of fixed charges generated in this structure.
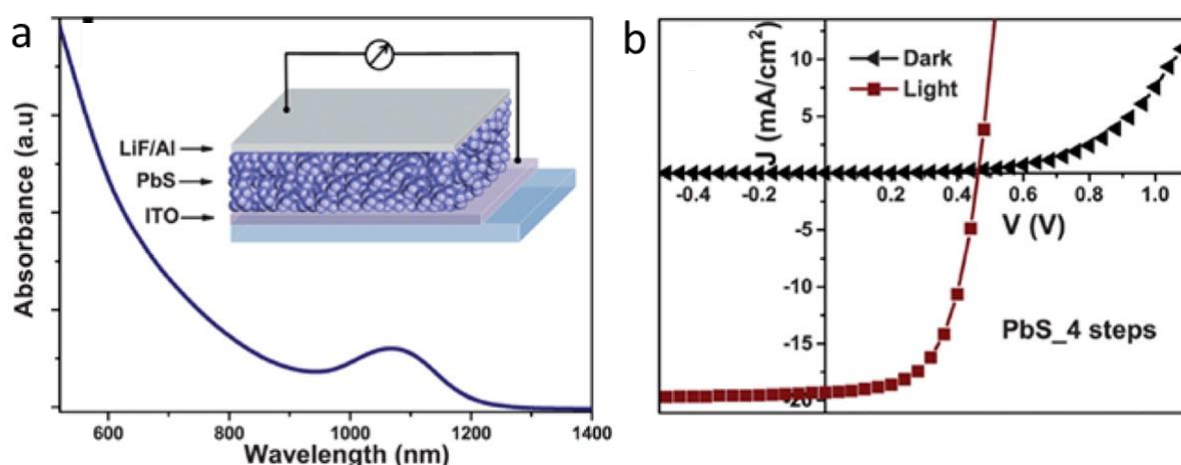
Figure 2-2-1 A scheme of the first pure CQD solar cell in a Schottky structure.[184] (a) Illustration of the cell structure and absorbance curve. (b) Dark and light J-V curves for PbS CQD Schottky-junction solar cell. This cell shown an efficiency of 5.2%.

To overcome the disadvantages of Schottky solar cells, heterojunction CQD solar cells were developed as the second stage of CQD solar cell development. Figure 2-2-2 shows the differences in the band diagrams between a heterojunction cell and a Schottky-junction cell. In a heterojunction structure, the junction is created by a n-type metal oxide and a p-type CQD layer. The advantage of this heterojunction structure is that the charge-carrier generation zone is in the vicinity of the depletion zone, meaning that more charge is separated across the junction. Compared to a Schottky structure solar cell in which the junction is located at the very rear part near the back contact, a heterojunction junction structure

facilitates more efficient carrier separation due to the carrier generation and depletion zones being closer. The heterojunction device provided an efficiency of 5.1%.[155] The developed charge-carrier separation enabled a higher efficiency for PbS-ZnO heterojunction solar cells.[186]
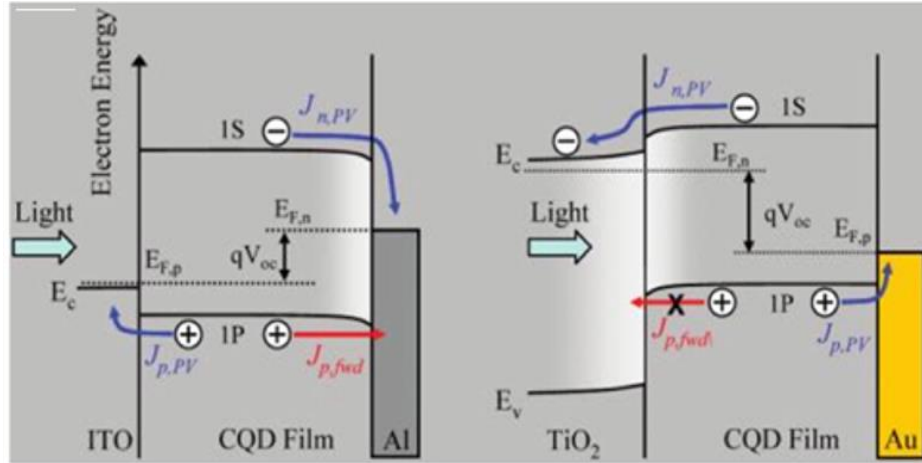
Figure 2-2-2 Band diagrams of Schottky-junction (left) and heterojunction structure (right).[155] In Schottky-junction structure, the junction is located at the rear side of a cell. In a heterojunction solar cell, the junction is located at the front part of the cell near the depletion region.

However, drawbacks limiting cell performance still exist in heterojunction structures, due to the band alignment and interface traps on the metal electrode-side, which is also hindering their application in multi-junction structures. For solving these problems, quantum junction CQD cells showing much improved performance (PCE=5.4%) were introduced and developed.[187] Figure 2-2-3 shows cell structures of both quantum junction and heterojunction cells. Figure 2-2-3 shows that in quantum junction cells, the carrier extraction is much improved because of elimination of barriers. PbS CQD solar cells in quantum junction structure have shown acceptable performance.[188-191]
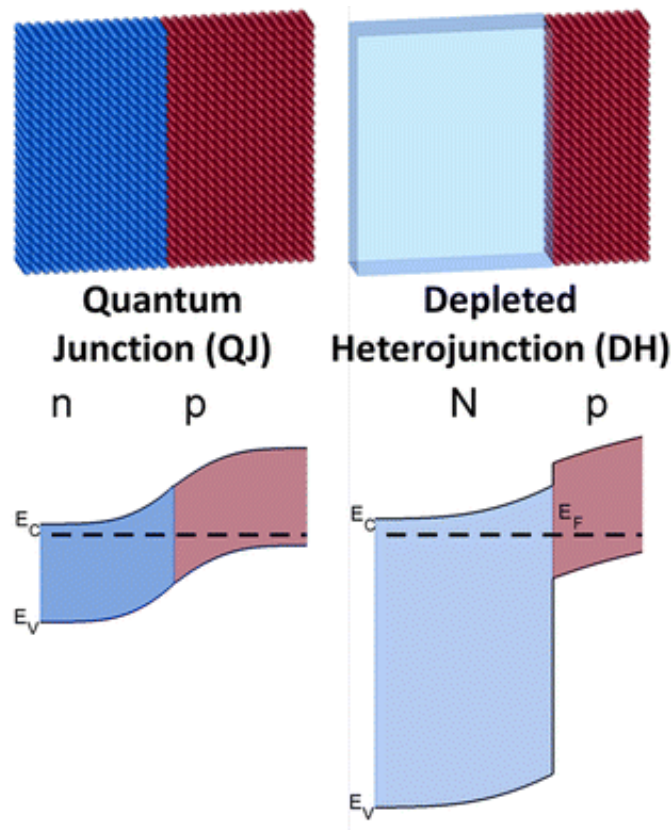
Figure 2-2-3 Comparing quantum junction and heterojunction quantum dot solar cells.[187] **In the quantum junction structure, an improved band offset is created which facilitates carriers' transport.**

In 2014, Bawendi et al [152] introduced a graded doping structure for assisting carrier extraction for quantum dot solar cells. The graded doping was achieved by employing different ligands in a quantum dot solar cell. Via graded doping, the improved cell performance was attributed to the introduced band offsets between the two PbS CQD layers, which efficiently block electron flow to the anode side while facilitating the hole extraction. Combining with novel ligands, this graded doping strategy yielded a certified efficiency record at 8.55%.[152] A graded doping structure is shown in Figure 2-2-4. In this structure, Tetrabutylammonium iodide (TBAI) was used on the ZnO electron transport side to provide iodine ligands for the PbS quantum dots, forming a more "n-type" quantum dot absorbing layer zone. On the hole transport side, PbS quantum dots with 1,2-ethanedithiol (EDT) ligands were applied forming a more "p-type" absorbing layer zone. The graded band-alignment structure was formed by using these two kinds of quantum dots with different ligands. The cell performance was improved because of enhanced carrier extraction and an enlarged depletion region due to this

graded band engineering. This graded doping cell structure has been widely used and has become a prevailing cell fabrication strategy and many following high performance quantum dot solar cell devices were based on this unprecedented structure.[192, 193]
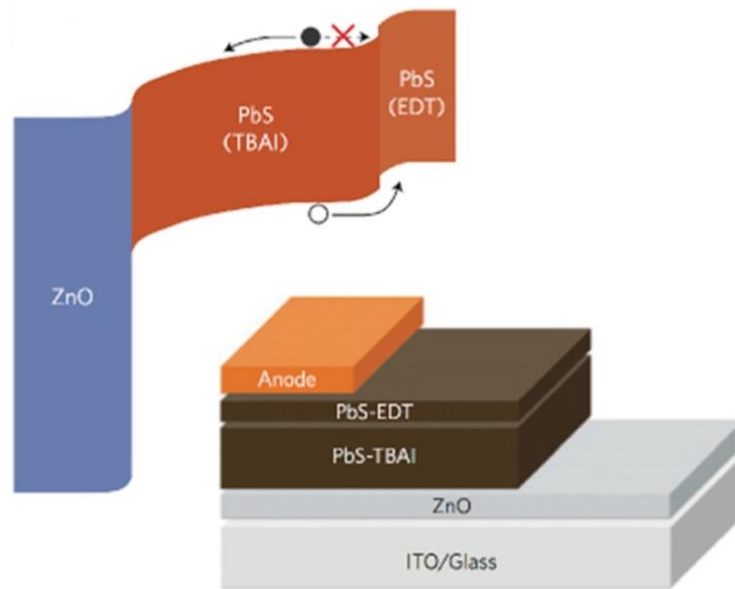
Figure 2-2-4 A graded doping structure.[152] This quantum dot solar cell is composed of a ZnO electron transport layer, a PbS-TBAI "n-type" quantum dot layer and "p-type" PbS-EDT quantum dot layer. This graded band structure developed PbS CQD solar cell performance to PCE=8.55% because of improved carrier extraction and a widened depletion region.

2.2.2 Further improving PbS CQD solar cells with various strategies

Due to quantum dots' attractive properties of tunable bandgaps, convenient solution-processed synthesis and low-cost as well as the fast developing solar cell efficiency, quantum dot based solar cells have become a promising research hot-spot in recent years. PbS is the mainstream material for quantum dot solar cells and numerous novel ideas have shown potential to further improve single-junction PbS CQD cell performance including structure evolution and other strategies introduced in this section.

One of the strategies is the graded bandgap structure which can be used to improve carrier extraction. Using tunable bandgaps of quantum dots, a graded bandgap structure based on PbS quantum dots has been created [194, 195], and the application of this concept on this PbS CQD solar cell has achieved improved current and voltage.[196] Figure 2-2-5 shows the scheme for the graded and anti-graded PbS CQD solar cells. The graded cell reached an efficiency of 2.7% while those of the ungraded and antigraded cells were 2% and 1.5% respectively.
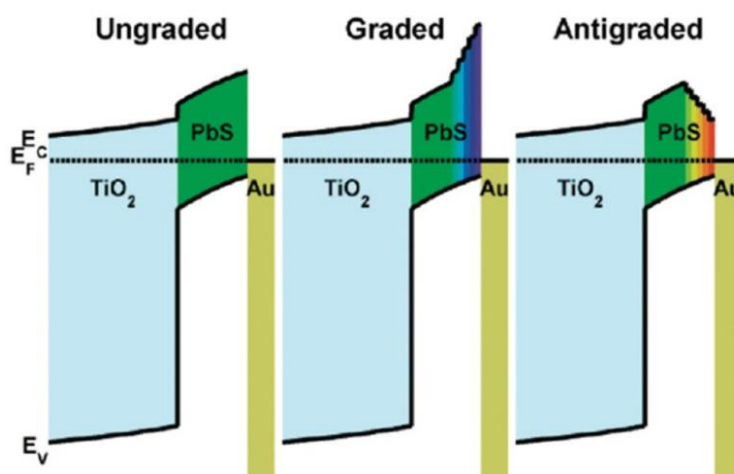
Figure 2-2-5 A scheme of graded and anti-graded solar cells based on PbS CQDs.[195] A graded band-offset structure facilitates carrier extraction and enlarges the depletion region so that this can enhance the cell performance while an anti-graded band-offset hinders carrier extraction and promotes recombination in the area near the Au contact leading to suppressed cell performance.

Another strategy about improving the cell structure is the inverted solar cell concept. An inverted structure moves the junction between n-type quantum dot layer and p-type quantum dot layer to the front side of the cell. As high energy photons which contribute the largest part of photon absorbance are mainly absorbed in the front part of solar cell, moving the p-n junction to the front side increases the cell performance by improving charge separation of excitons generated by high energy photons. Ruili et al [197] have introduced an inverted PbS CQD solar cell which exhibited a PCE>9%. Kunyuan et al [198] also fabricated an inverted CQD solar cell with different hole transport layers and the cells with inverted structure achieved an efficiency of >8%. Figure 2-2-6 shows an inverted CQD solar cell structure.
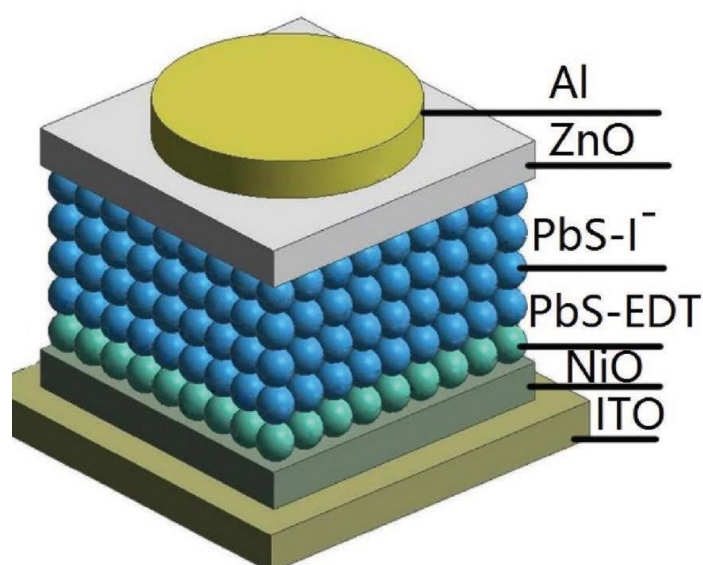
Figure 2-2-6 Structure scheme of an inverted CQD solar cell.[197] The junction between "p-type" PbS-EDT and "n-type" PbS-I was moved to the front side of this cell, which is favourable for charge separation of excitons generated by high energy photons, which are mainly absorbed in the front part of the cell.

Solution-phase one-step ligand exchange as a promising strategy has developed PbS CQD solar cell cell efficiency greatly. In 2016, Mengxia et al [191] developed solution phase ligand exchange and created a one-step quantum dot film fabrication method. This solution-phase-ligand-exchange method significantly reduced surface defects which are introduced largely when the solid-state-ligand-exchange method is applied. This is the first time solution-phase-ligand-exchange has been applied on PbS CQD solar cells to achieve high quality materials. For solid-state-ligand-exchange, repeating the film making process is necessary to reach a desired film thickness, where more interfaces can be created and more chances for forming defects. In contrast, solution-phase-ligand-exchange requires spin-coating only once for forming the film which tremendously reduces defects. Note that this one-step method is also a time-savings and convenient approach for cell fabrication, which provides greater potential for industrial manufacturing. An unprecedented 11.3% efficiency has been reached by this one-step method. Two years later, Jixian et al [157] introduced a modified one-step method and a new record PCE of 12.5% has been reached by this method. In the same year, Havid et al [199] achieved solid-state-ligand-exchange-free quantum dot inks and the cell made with these inks achieved a PCE of 11%. Figure 2-2-7 illustrates reactions and processes involved in

solution-phase-ligand-exchange. The achievement of one-step method is an important milestone in history of quantum dot solar cell development.
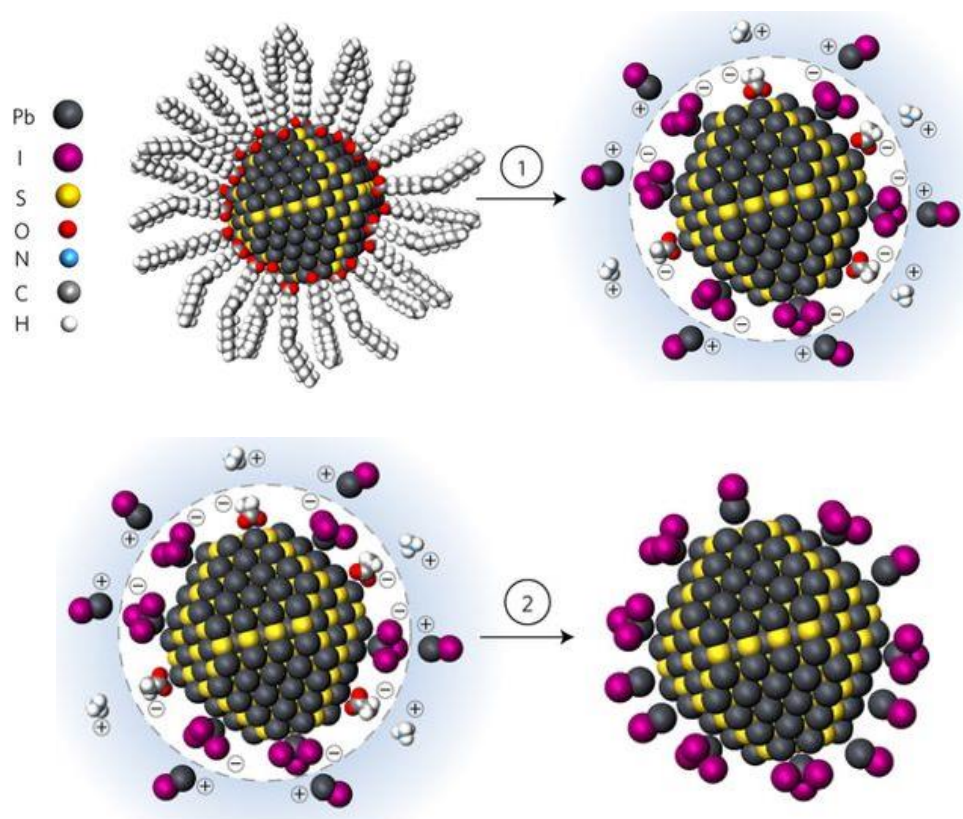
Figure 2-2-7 A scheme for the processes of solution-phase-ligand-exchange.[191] Process 1 (ligand exchange): the bulky oleic acid ligands are replaced by the PbI_2 with the aid of ammonium ions. Process 2 (CQD precipitation): after ligand exchange, CQDs are precipitated via the addition of toluene, an anti-solvent, and are separated by centrifugation.

In addition, developing p-type hole transport layer and n-type electron transport layer both improve solar cell performance. For hole transport layers, Hu et al [200] used an Ag doped hole transport layer and achieved above 10% efficiency. For n-type electron transport layer, recombination at the interface between metal-oxide and quantum dot absorber has been a concern. Making a trap-less interface with acceptable well aligned band-offset is a possible direction for further improving device efficiency. To solve this problem, inserting a buffer layer such as zinc oxide or [6,6]-phenyl-C61-butyric acid methyl ester (PCBM) decreases trap density and increases efficiency [201, 202] and a heavily doped n-type layer improved charge

carrier extraction significantly [203]. Besides, a post annealing process was introduced by Yiming et al [204] in 2016. This annealing process removed excess hydroxyl ligand so that an improved CQD solar cell performance was achieved. Figure 2-2-8 shows the increased performance after annealing.
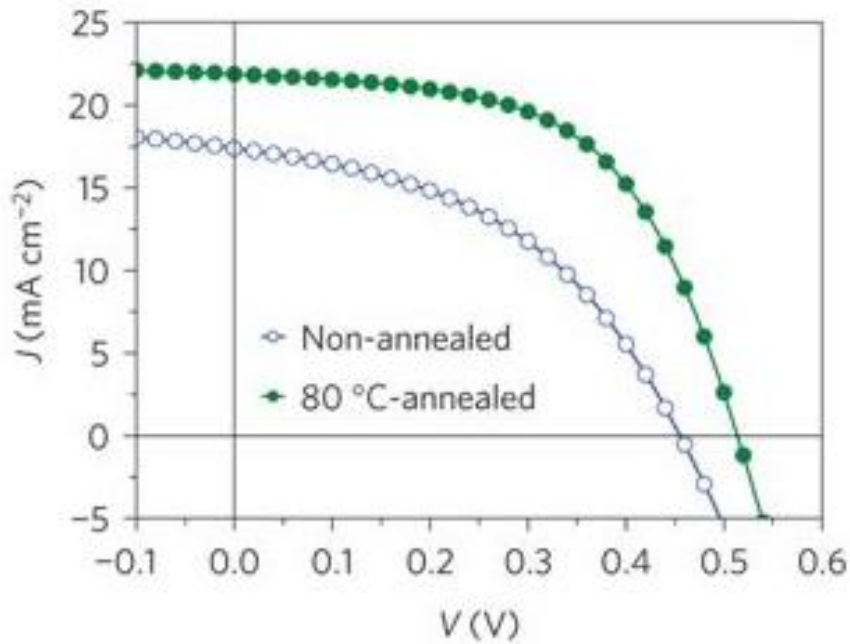
Figure 2-2-8 J-V curves of solar cells with and without annealing.[205] With 80 °C annealing, cell performance has been improved from 3.5% to 6.4% with tetrabutylammonium iodide (TBAI) and ethanedithiol (EDT) liangds.

2.2.3 Other CQD solar cells

Besides PbS quantum dots, PbSe is another extensively studied quantum dot material. PbSe quantum dots exhibit a strong multi-exciton generation effect (MEG effect) which has already resulted in external quantum efficiency (EQE) exceeding 100%.[57, 206-208] This is a very unique property which may lead to efficiency beyond Shockley-Queisser limit in the future. Huang et al [209] introduced a PbSe CQD cell using perovskite quantum dot as hole transport layer which has improved the cell's efficiency to 7.22% . Halpert et al [210] fabricated perovskite passivated PbSe quantum dots and the cell efficiency reached 9.2%. For a long time, low stability of PbSe CQD solar cell in ambient was a considerable problem compared to PbS CQD solar cells, which hinders the application of PbSe quantum dot in solar cells.[59,

[211, 212] In 2019, Huang et al [213] fabricated a SnO_2/PCBM electron transport layer improved PbSe CQD solar cell with 10.4% efficiency which can be stably stored for 30 days in ambient conditions. Figure 2-2-9 shows the band structure and J-V curve for this record high performance PbSe CQD solar cell.
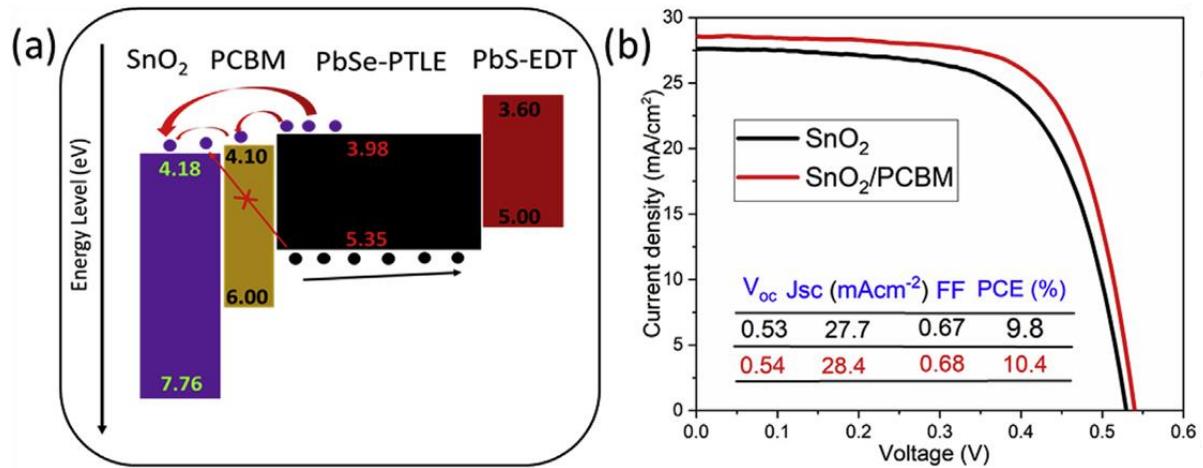
Figure 2-2-9 Band alignment scheme (a) and J-V curves (b) of a high performance PbSe CQD cell.[213] In this cell, the application of SnO_2/PCBM electron transport layer is in favour of electron transfer, so that the performance of the cell had been improved greatly.

Other kinds of chalcogenide (CdTe, CdS, PbSe) quantum dots are also promising materials for absorbing layers.[214-218] A novel ligand design has boosted CdTe CQD cell efficiency to be above 10% [219] while a doping strategy improved CdS CQD cell efficiency to be over 5%. Perovskite quantum dots have drawn a lot of attention alongside the research hotspot of perovskite as bulk material. Instability at room-temperature is a problem concerning perovskite bulk material research.[220-222] Recently, a perovskite CQD solar cell provided a potential solution to this problem. In 2016, Luther et al [223] shown that $CsPbI_3$ perovskite quantum dots exhibited much improved stability over bulk material at room temperature. In 2017, Luther et al [224] continuously pushed the efficiency of perovskite CQD solar cell to 13.4% using halite salt treatment, which settled a new record for CQD solar cells.

Alongside with chalcogenide-containing materials, non-toxic material elements such as bismuth, indium, tin, copper and silver are also very attractive research topics due to their

non-toxic, user-friendly characters [225-227]. Applying these non-toxic environmental friendly elements can be very appealing to materials and solar cell researchers. However, development of non-toxic materials for solar cells is in a very initial stage. The $CuInS_2$ CQD solar cell has just reached above 1% efficiency[228]. Though a remarkable 6.3% PCE has been achieved by a $AgBiS_2$ CQD solar cell [229], the stability of this material is a problem for further developing its application. Further applying these materials needs better understanding and investigation into their properties and processing techniques.

2.3 Application of CQD in tandem solar cells

2.3.1 Tandem solar cells

Tandem solar cells are, so far, the only realised strategy that has overcome the Shockley-Queisser limit to date.[64] The Shockley-Queisser limit was introduced by Shockley and Queisser in 1961 [21] using detailed balance limit (DBL) calculation to analyse single-junction solar cell efficiency potentials. Figure 2-3-1 illustrates the result of detailed balance limit calculation, where below bandgap transmission loss, high-energy carrier thermalisation loss, Boltzmann loss due to entropy generation, Carnot loss due to the finite temperature of the cell and emission loss due to modified black-body emission effect are all responsible for the power losses for a single-junction solar cell.[230] From the Figure 2-3-1 we can see that intrinsic losses of below-bandgap non-absorbed photons and carriers cooling to bandgap edge are the dominating primary loss mechanisms leading to this Shockley-Queisser limit for single-junction cells[230, 231]. Hence, tandem or multi-junction cells could provide a solution to alleviate these two primary losses by combining two or more cells corresponding to different spectral ranges with specially designed interlayers into one monolithic tandem structure. Figure 2-3-2 shows a scheme of the structure of a tandem cell. In this tandem cell, the front cell (high bandgap cell) responds to high energy short-wavelength light, while the rear cell (low bandgap cell) respond to lower energy long-wavelength light respectively, so that a more efficient utilisation of the solar spectrum can be obtained by this monolithic multi-junction tandem solar cell.
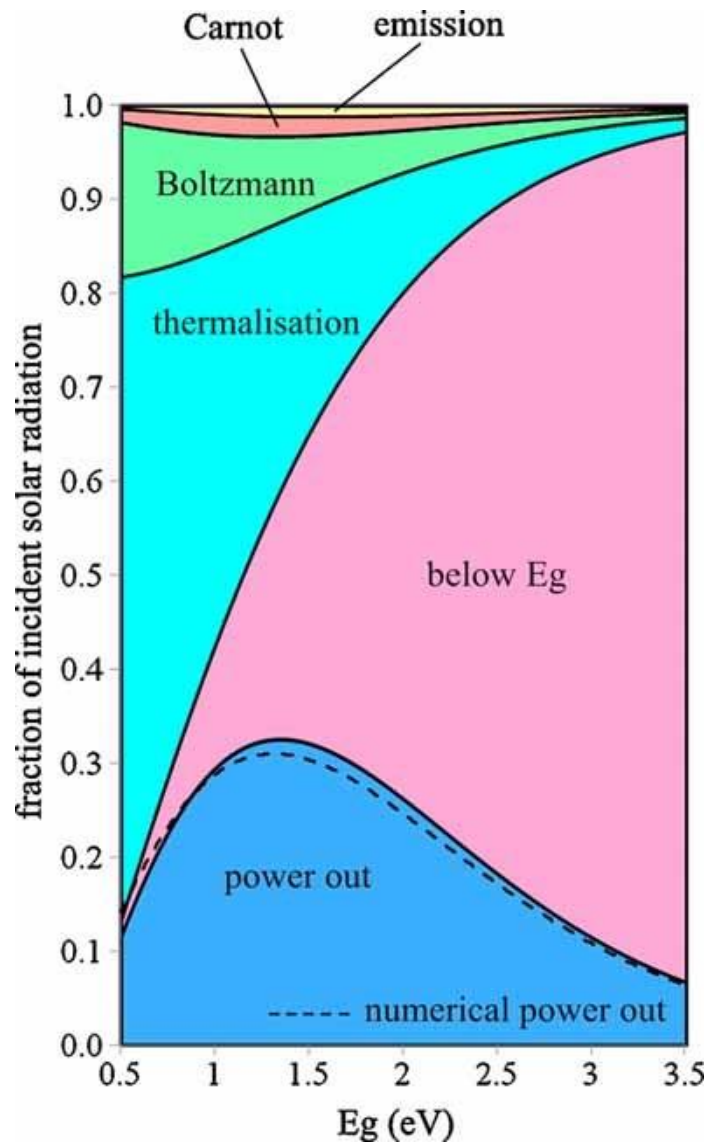
Figure 2-3-1 Fractions of energy losses at different bandgaps [230] **. Below bandgap transmission loss and high-energy carrier thermalisation loss are the dominating losses. 1.33 eV is the optimal bandgap for a single-junction solar cell where the maximum efficiency expectation is 33.7%.**

There are three criteria for designing a high performance tandem cell, namely, a well aligned band offset, highly effective interlayers and current matching between adjacent subcells.[67, 77, 232] The first criterion of a well aligned band offset could be met by choosing suitable absorbing materials. For now, the highest certified record among tandem cells and also among all kinds of cells of PCE=46.1% is achieved by III-V group materials.[64] This cell employed a bandgap combination of 1.9, 1.4, 1.0, and 0.5 eV for sub cell absorbers, which is close to the ideal values of 1.9, 1.4, 1.0, and 0.5 eV bandgaps combination obtained from detailed balance calculation.[233] The record organic tandem solar cell with 17.3% efficiency

was achieved largely due to a careful selection of rear cell material with a bandgap of 1.2 eV.[67] Combined theoretical and experimental work may facilitate the selection for appropriate bandgaps for a tandem cell. For Si-perovskite tandem cells as an example, the theoretical optimal bandgap for front perovskite cell is 1.7 eV,[234, 235] while experiments shown that 1.6 eV is the optimal value due to parasitic absorption which is not included in calculations.[236, 237]
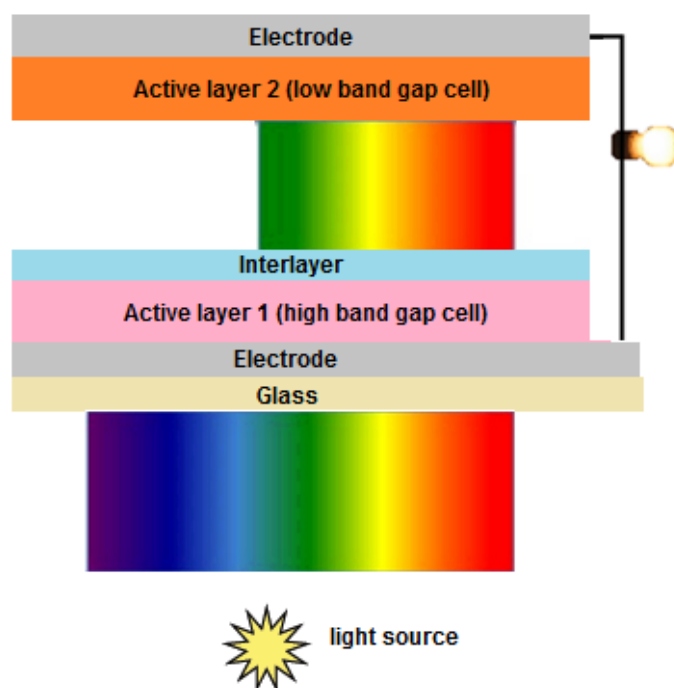
Figure 2-3-2 Scheme of the structure of a tandem solar cell.[238] The high bandgap cell is also referred to as front cell, while the low bandgap cell is also referred to as rear cell. Front cell and rear cell are connected by the interlayer to more efficiently utilise the solar spectrum. In this scheme, the "gap" between "Interlayer" and "Active layer 2" is specifically drawn for showing light splitting, which does not exist in a monolithic device.

The second criterion of a recombination layer or interlayer is a crucial part for making a high performance CQD tandem solar cell. For III-V group tandem solar cells, tunnelling recombination layers were usually constructed by employing lattice-matched materials with different doping levels.[239-243] For organic tandem solar cells, a variety of recombination layers have been developed such as PEDOT:PSS/ZnO [244-248], TiOx/PEDOT:PSS [249, 250], ZnO/MoO$_3$

[66, 251], PF3N-2TNDI/PEDOT:PSS [252] and MoO_3/Ag/PFN [253, 254]. Compared to organic tandem cells, perovskite tandem cells show more similarities with CQD tandem cells because they both require an avoid-polar-solvent fabrication process where interlayers such as (spiro-OMeTAD / PEDOT:PSS / PEI / PCBM:PEI)[255-259] have been applied. One noteworthy work achieved a 23.6% efficiency using a perovskite/Si tandem cell with a NiO/ITO interlayer.[260]

The third criterion, which is also one of the biggest challenges to fabricate high performance two terminal monolithic tandem solar cells, is the current matching for subcells.[67] In a monolithic tandem configuration, the front cell and rear cell are connected in series. Therefore the overall current is limited by the lower one of the two currents from front and rear cells reducing the device performance. Balancing subcells' currents by adjusting both absorbing layers' thicknesses until subcells' currents match with each other is an optional strategy to optimise tandem cell current. Optical modelling can predict the current from each subcell under a certain absorbing layer thickness and provides significant guidance for the design of the tandem structure.[236] Modified detailed balance limit calculation [67, 237] and semi-empirical modelling [261] are also reported methods for providing guidance for designing subcells' thicknesses for achieving current matching.

2.3.2 CQD tandem solar cells

CQD-CQD tandem cells are drawing more and more attention recently. This is mainly due to the recent great development of single-junction CQD solar cell efficiency and processing techniques. The recent progresses [188-191] of single-junction CQD solar cells (>12% PCE) has paved the way for CQD tandem cells to become an up-coming research hot-spot considering quantum dots' unique advantages dedicated for tandem solar cells.

Quantum dots possess dedicated advantages for forming a tandem solar cell. Firstly, bandgaps of quantum dots could be tuned from 0.4 eV to 1.6 eV by simply adjusting nano-crystal size.[71, 72] Secondly, doping types of quantum dots are also tunable by using different ligands. For example, iodine ligands could create n-type quantum dots [119, 126] while p-type quantum dots can be obtained by using MPA ligands.[88, 147] Thirdly, as-deposited quantum dot films are relatively robust to solvents during the subsequent interlayer and rear cell processing, which makes it easier to fabricate tandem structures.[262] In addition, in-solution-processability can further provide convenience for CQD tandem solar cell construction.[147]

However, previous research on CQD tandem solar cells has yielded a relatively small number of reports to date.[75-77, 261, 263]

In 2011, Wang et al[75] fabricated the first PbS CQD tandem solar cell. In that work, Front cell and bottom cell bandgaps of 1.6 eV and 1.0 eV were chosen respectively according to a simulation based on a graphical method.[264, 265] A gradual recombination layer was designed showing an ideal combination of two subcells. This gradual recombination layer includes a combination of MoO_3, ITO, ZAO and TiO_2 layers. Current matching of subcells was reached by calculating the absorption of both subcells. Both experimental adjustments and calculations were conducted to make accurate thickness adjustment. A scheme of the tandem cell structure is shown in Figure 2-3-3(a). The cell had shown a PCE of 4.21%. The tandem cell voltage is the sum of subcells' voltages, which indicates an ideal combination of subcells by the designed interlayer. Figure 2-3-3(b) shows J-V curves for the tandem cell and corresponding subcells.
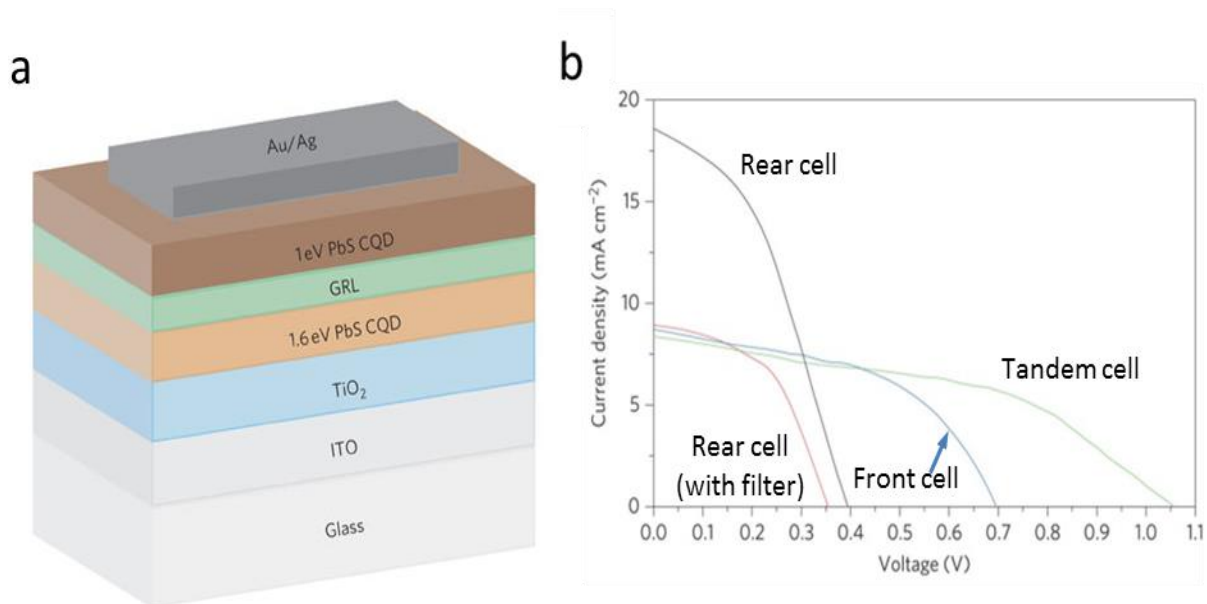
Figure 2-3-3 (a) A scheme of Wang's PbS CQD tandem solar cell structure. The complicated gradual recombination layer (GRL) includes four layers of MoO_3, ITO, ZAO and TiO_2. (b) J-V curves of this tandem cell and corresponding subcells.[75]

In the same year, Choi et al [76] reported another PbS CQD tandem solar cell with a simpler recombination layer of thin Au layer. Choi's work employed CQDs' bandgap combinations of 1.6 and 1.0 eV for front and rear subcells respectively according to detailed balance limitation calculation.[266] A simpler recombination layer composed of a thin Au layer was employed which effectively combined subcells' voltages. However, the PCE of tandem is much lower than that of Wang's work. This may be partly due to too thin absorbing layers which are only 50nm in thickness, leading to low current density for the tandem cell. Figure 2-3-4 shows the band diagram of Choi's PbS CQD tandem solar cell. A well designed subcells' thickness combination by optical modelling[236] can be a promising way to improve the tandem cells' current.
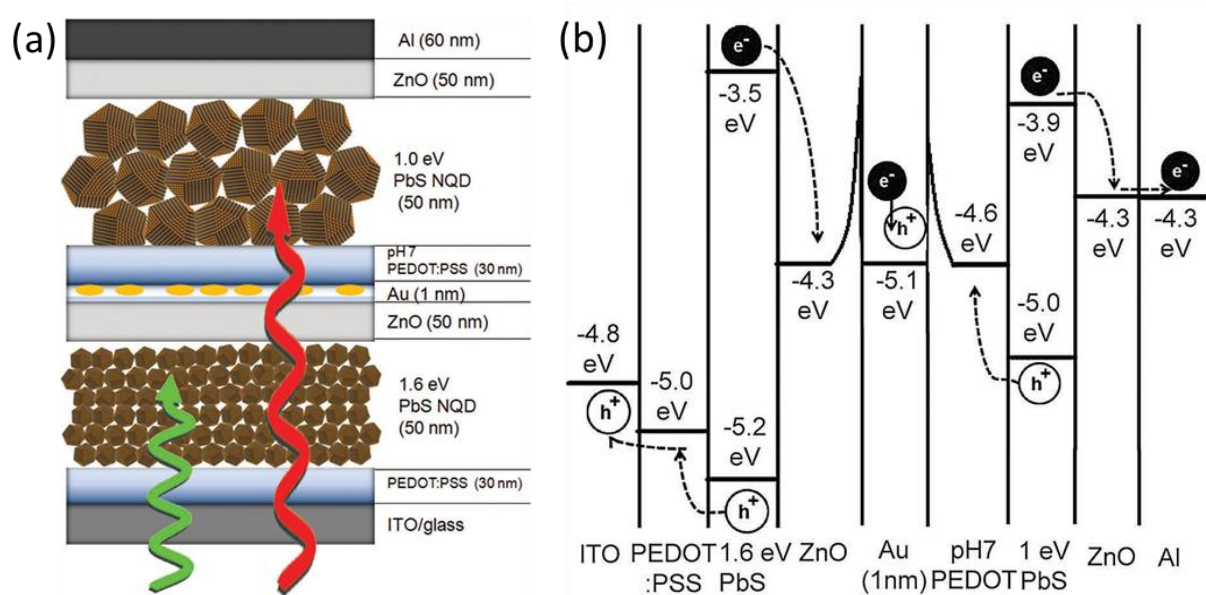
Figure 2-3-4 Choi's PbS CQD tandem solar cell structure (a) and band-diagram (b).[76] (a) the front cell and rear cell used 1.6 eV and 1.0 eV PbS CQDs respectively. An ultra-thin Au interlayer of 1 nm was applied in this tandem cell. (b) A well designed band alignment is illustrated here. Schottky barriers formed between Au and ZnO as well as between Au and PEDOT.

A hybrid CdTe-PbS CQD tandem solar cell was reported by Luther et al[261] in 2016. For the first trial of this kind of cell, the experimental PCE reached 5%. In Luther's study, one significant contribution is that a systematic simulation was made for a hybrid CdTe-PbS CQD tandem solar cell. In this simulation, not only a classical detailed balance limit calculation was conducted with the assumption that a subcell absorbs all photons with energy above the bandgap, as shown in Figure 2-3-5(a), but also the calculation with a semi-transparent absorbing film assumption was carried out, of which the simulated result is shown in Figure 2-3-5(b). According to this simulation, based on a CdTe front cell with bandgap of 1.5 eV and a PbS rear cell with a bandgap of 0.95 eV, an optimum efficiency of above 40% can be expected by the simulation. The judiciously designed recombination layer of ZnTe-ZnO shown a smooth transition between the subcells with minimal voltage loss. Both modelling and experimental tests were combined for deciding the absorbing layer thicknesses for subcells in this work.
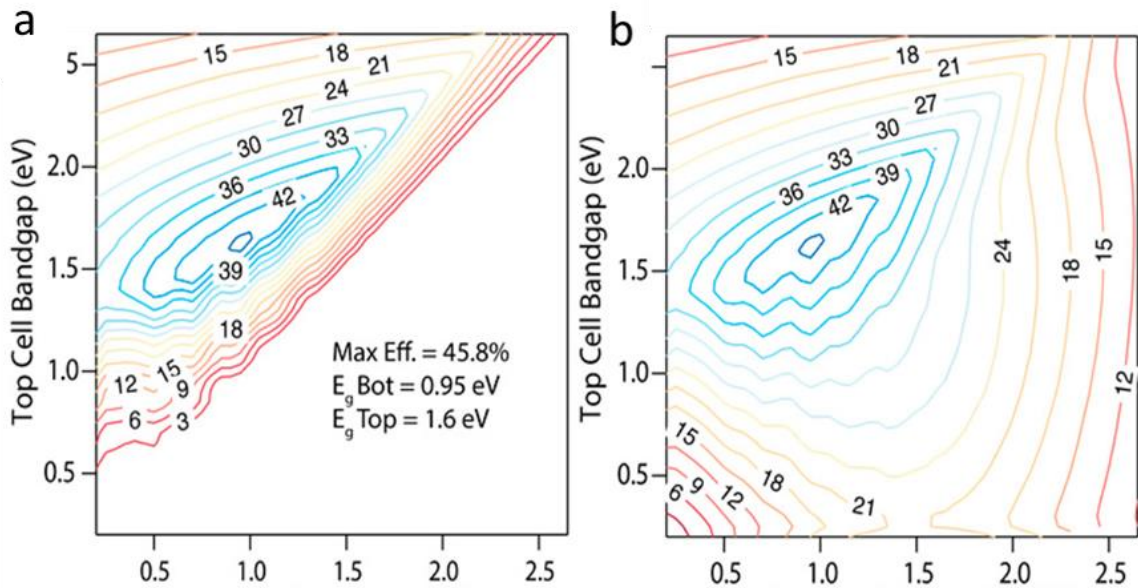
Figure 2-3-5 Simulations for CdTe-PbS CQD tandem solar cell [261] . (a) Based on classical detailed balance limit calculation, the assumption that all photons above the bandgap are absorbed by a subcell was applied. (b) A semi-transparent film assumption was applied in contrast with above mentioned simulations, which means photons can transmit through a subcell by adjusting this subcell's thickness.

In 2017, Ma et al [77] reported a research about PbS CQD tandem solar cells with a champion cell achieving ~9% efficiency, which is more than double the previous record value. This research employed two rationally designed recombination layers: PbS-EDT/PEDOT/ZnO and PbS-EDT/Au/ZnO. The tandem cells' structure is shown in Figure 2-3-6. The results of experiments (Table 2-3-1) in Ma's research showed that replacing PEDOT with a thin layer of gold increased the PCE of a tandem solar cell from 7.7% to 8.6%, while a significant increase in FF from 58.5% to 66.4% was the main reason for the increased PCE. In Ma's research, a 1.13 V tandem cell voltage was obtained showing well aligned bandgaps and ideally combined subcells. In Table 2-3-1, a series of recombination layer were investigated and reported in the research, which can provide a detailed guidance for future studies on this kind of cell. In Ma's research, for optimising the tandem cell's current density, a series of the absorbing layers' thicknesses were tested for identifying the optimal thicknesses. One thing worth a note is that though PbS quantum dots with the same size were used for front and rear cells in Ma's work, an unprecedented efficiency was still achieved.
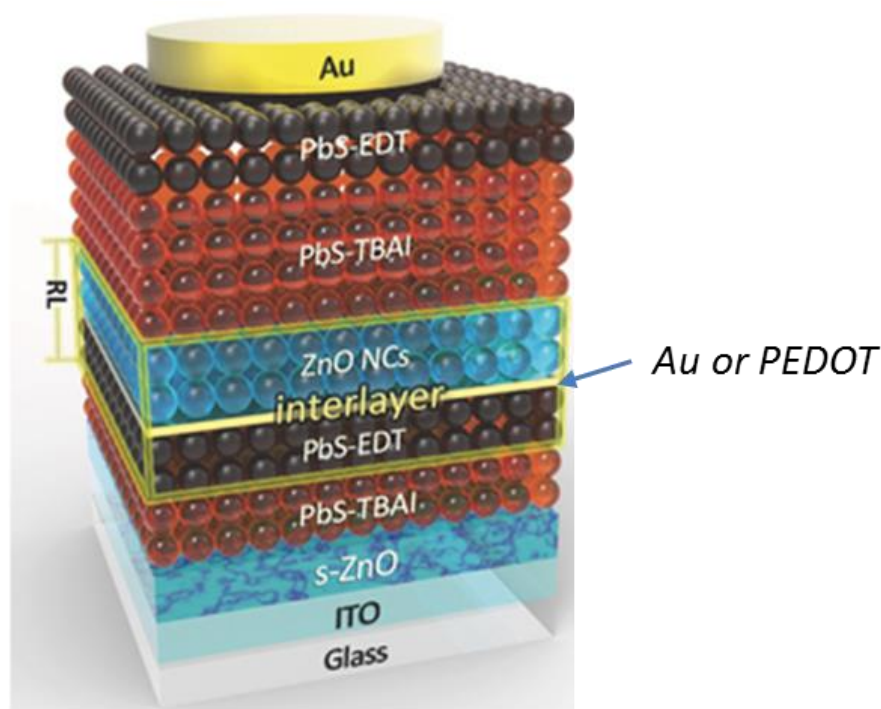
Figure 2-3-6 Illustration of Ma's PbS CQD tandem solar cell structure.[77] Front cell and rear cell are both composed of ZnO electron transport layer and PbS absorbing layer. An interlayer of PEDOT:PSS or ultra-thin Au layer was used to connect the subcells.

Fabrication technique	Structure	J_{sc} [mA cm^{-2}]	FF [%]	V_{oc} [V]	PCE [%]
Full solution processing	PEDOT/ZnO	9.11	42.5	0.61	2.4
	PbS-EDT/ZnO	10.27	45.2	0.42	1.9
	PbS-EDT/PEDOT/ZnO	12.92	58.5	1.02	7.7
Solution processing/e-beam evaporation	Au/ZnO	7.12	52.4	0.65	2.4
	PbS-EDT/Au/ZnO	11.93	66.4	1.08	8.6
	PbS-EDT/Au/n-ZnO	12.26	64.1	1.13	8.9

The most recent research on CQD tandem solar cell was about a PbS CQD tandem solar cell by Bi et al [263] in 2018. Bi et al [263] introduced a chemical vapor deposited graphene layer as interlayer for the PbS CQD tandem solar cell. A high efficiency of 8.2% was achieved by using a 1.4 eV and 1.3 eV bandgap combination of quantum dots. A more ideal bandgap combination of 1.43eV and 0.95eV was expected to be able to reach higher tandem cell efficiency, however, only an efficiency of 7.1% was achieved by this bandgap combination. The reason can be that a narrow bandgap CQD rear cell led to a lower overall tandem cell voltage. Figure 2-3-7 shows Bi's PbS CQD tandem solar cell structure and EQEs of subcells. Subcells' thicknesses were determined by both optical modelling and experimental tests. One thing worth a note is that an ultra-high rear cell current integrated from EQE measurement of 17.5 mA/cm^2 could be achieved in this research.
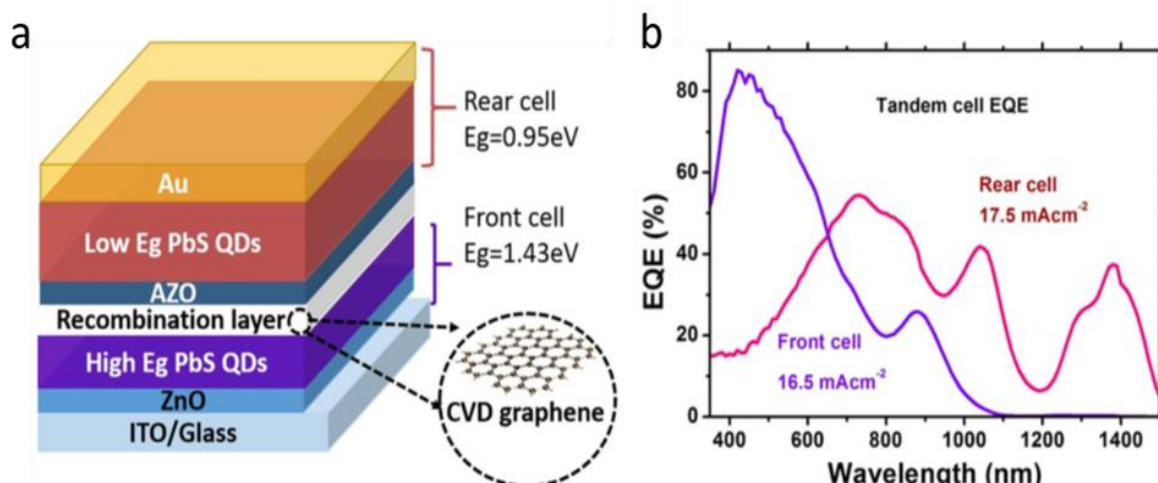
Figure 2-3-7 Bi's PbS CQD tandem solar cell structure(a) and EQEs of subcells (b).[263] A chemical vapour deposit (CVD) graphene interlayer was introduced in this tandem cell. With a front cell bandgap of 1.43 eV and a rear cell bandgap of 0.95 eV, the integrated current from EQE of the front cell achieved 16.5 mA/cm^2 and that of the rear cell reached 17.5 mA/cm^2.

2.3.3 Tandem solar cells using CQD and other materials

Colloidal quantum dots and organic material have been combined to form tandem cells because of their mutually compensated absorbing spectrums.[267, 268] Tong et al [267] reported a CQD/organic tandem solar cell with an efficiency of 7.4%. A scheme of this tandem cell structure is shown in Figure 2-3-8(a) and absorbance curves of both subcells are shown in Figure 2-3-8(b). Complementary absorption was achieved in this tandem cell by using organic front cell and PbS CQD rear cell which respond to different but compensating wavelength ranges. Sargent et al [268] also studied CQD/organic tandem (PCE=5.3%) which could extend the absorption spectrum of an organic cell by incorporating a CQD subcell [246, 248]. Tong [267] and Sargent [268] both found that using quantum dots as the bottom cell absorbing material could achieve a better tandem cell performance than switching subcells' sequence as the solvent processability of quantum dots is better than polymers.

For adjusting the thicknesses of subcells in CQD/organic tandem cells, a modelling was introduced for optimising CQD/organic current matching by Speirs et al[269]. The result of the

modelling as shown in Figure 2-3-9(a), the solid line indicates the optimised thicknesses of subcells when PbS CQD cells were used as front cells. As an early stage research, guided by the modelling, the tandem cell efficiency reached 1.8%. This PbS CQD/organic tandem solar cell employed Al/WO$_3$ as inter-layer and the champion cell showed a V_{OC} of 0.89 V occupying 92% of the sum of subcells. The J-V curve of Speirs's CQD/organic tandem solar cell is shown in Figure 2-3-9(b).
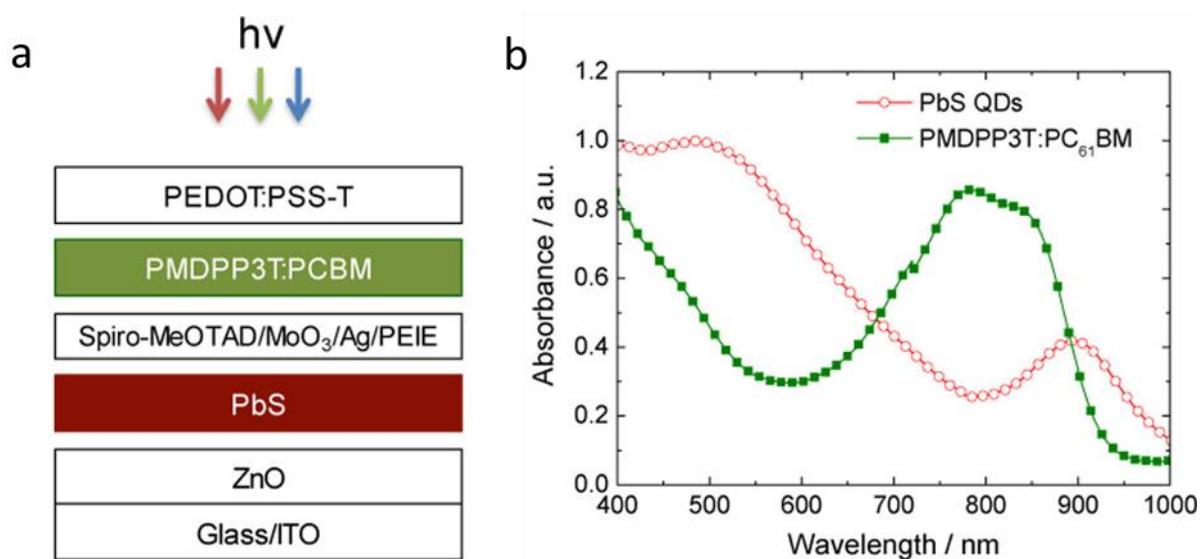
Figure 2-3-8 (a) Scheme of Tong's CQD/organic tandem solar cell's structure.[267] (b) Complementary absorbance of subcells of Tong's CQD/organic tandem solar cell.[267]

A series of interlayers were investigated for CQD/organic tandem cells such as Spiro-MeOTAD/MoO3/Ag/PEIE [267], MoOx/ZnO/PFN [268], Al/WO$_3$ [269]. A high performance CQD/polymer tandem solar cell was developed by Havid et al [270] with a MoOx/Au/ZnO recombination layer. The PCE of this tandem cell rose from 7.6% to 8.3% by inserting a thin layer of gold in the recombination profile. Sargent et al [271] found a similar trend in another CQD/organic tandem work in which the PCE increased to 7.9% from 5.3% due to the insertion of a Au layer. This increase is due to improved conductivity by inserting the Au layer. However, inserting an Au interlayer may cause reduction in transparency.
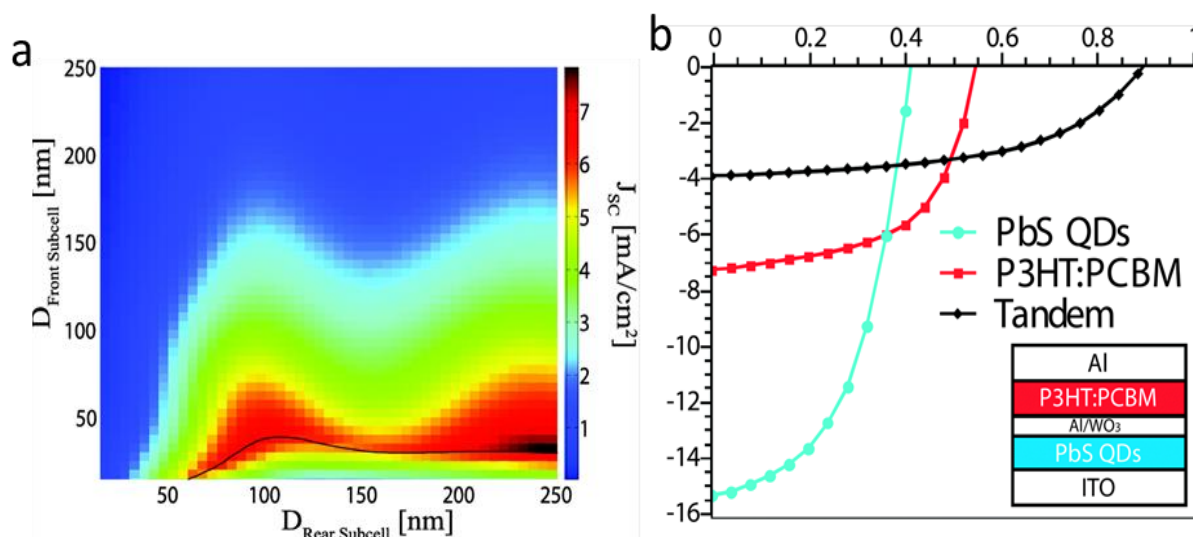
Figure 2-3-9 (a) Simulation of current matching for PbS CQD/organic tandem solar cell. The black solid line indicates the optimised thickness combinations. (b) J-V curves of PbS CQD/organic tandem solar cell.[269]

The only CQD/perovskite tandem solar cell research to date so far was reported by Ma et al in 2018.[262] There are few reports on this kind of tandem cell because the perovskite absorbing layer is easily destroyed when casting rear cell layers onto a perovskite front cell substrate. Even in this, only, research about CQD/perovskite tandem solar cells, the PbS CQD cell was employed as front cell and the perovskite cell as rear cell due to the difficulty of adding layers onto a perovskite substrate. When a perovskite cell was applied as the front cell, the poor solvent tolerance of perovskite would lead to front cell degradation in this structure. So making perovskite as a front cell is still a great challenge for tandem cell researchers. Ma's CQD/perovskite tandem solar cell reached a PCE>10%, which is still a pioneer contribution to this kind of tandem solar cell research. Figure 2-3-10 shows the structure of Ma's CQD/perovskite tandem cell and a cross-sectional SEM image of the cell.
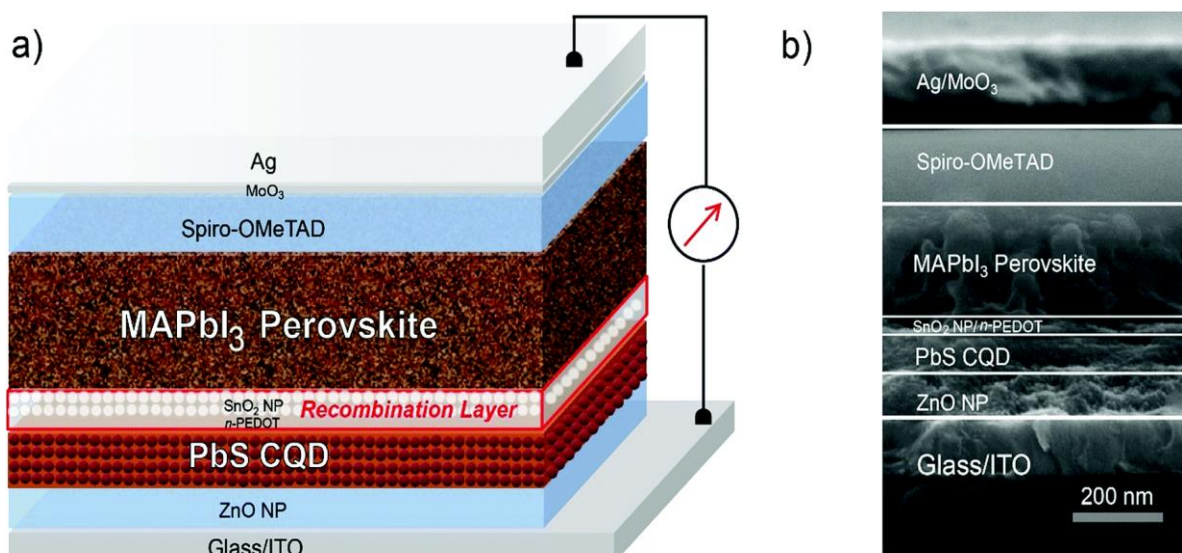
Figure 2-3-10 (a) Scheme of Ma's CQD/perovskite tandem solar cell and (b) a cross-sectional image of this tandem cell.[262] A PbS CQD front cell and a perovskite rear cell were adopted in this tandem cell structure.

2.4 Conclusion

In this chapter, the following aspects are reviewed in sequence: quantum dot synthesis and ligand exchange, single-junction PbS CQD solar cell development and the application of CQDs in tandem solar cells. The advantages of tunable bandgaps, solution-processed low-cost synthesis and easy cell fabrication process have made quantum dot a suitable material candidate for absorbing layers in a tandem solar cell.

Regarding the PbS CQD tandem solar cell, the material synthesis and single-junction cell fabrication techniques have been developed which provides a solid foundation for further pushing quantum dots into the tandem solar cell application. In chapter 3 after this chapters, a $MgCl_2$ doped ZnO electron transport layer would be introduced for further improving the single-junction PbS CQD solar cell's performance.

By investigating quantum dot related tandem solar cells including CQD tandem solar cells as well as tandem solar cells using quantum dot and other materials, the most fundamental problem facing a tandem device is the current matching problem. Current matching is an

important criterion for high performance in any tandem cell. In a monolithic tandem configuration, the front cell and rear cell are connected in series. Therefore the overall current is limited by the lower one of the two currents from front and rear cells reducing the device performance for current-mismatched cells. Optical analysis is a powerful tool to predict the current from each subcell based on their optical constants. Current matching can be achieved by adjusting the thicknesses of the absorbing layers to optimize device performance. In chapter 4 in this thesis, optical modelling is used to analyse PbS CQD tandem solar cells and to provide useful guidance for the design of PbS CQD tandem solar cells.

Currently, the tandem PbS CQD solar cell research field has yielded a limited number of reports. Most of them have adopted an ultra-thin Au interlayer, while only one work[75] utilised transparent ITO material within a complicated composite interlayer. In chapter 5 in this thesis, PbS CQD tandem solar cells with Au interlayer were further investigated and a graded band alignment strategy has been applied to improve tandem cell performance by developing the rear cell's carrier extraction. Additionally, a much simplified mono-layer ITO interlayer has been applied and investigated in PbS CQD tandem solar cells.

Chapter 3. Improving Single-junction PbS CQD Solar Cell by MgCl₂ Treated Electron Transport Layer

Making high-qualilty single-junction cell is a fundamental work for achieving a working tandem cell. High performance CQD solar cells rely on good-quality electron transport layers (ETL) that act as carrier selective contacts for extracting electrons. Though a variety of n-type oxides have been extensively studied as electron transport layers, a detailed understanding of their surface and interface states as well as mechanisms to improve their optical properties are still being developed. This chapter reports on a simple procedure to produce $MgCl_2$ passivated ZnO nanoparticle electron transport layers that have improved PbS CQD solar cell performance. The $MgCl_2$ treated ZnO electron transport layers have boosted the PbS CQD solar cell efficiency from 6.3% to 8.2%. The cell has exhibited both improved FF and J_{SC} due to reduced surface defects on ZnO nanoparticle surfaces an improved carrier extraction, leading to significantly improved cell performance. This low-temperature $MgCl_2$ treated ZnO electron transport layer can be applied not only in solution processed single-junction PbS CQD solar cells but also in PbS CQD tandem solar cell interlayer as a promising strategy to further increase solar cell efficiencies.

3.1 Introduction

Colloidal quantum dots have been developed as competitive candidates for fabricating LEDs, [272-274] photodetectors [275, 276] and photovoltaic devices [147, 189, 277-281] due to their tunable bandgaps [71] and simple solution processed synthesis.[282] Improvements in CQD solar cell performance has been dependent mainly on developments in quantum dot surface passivation [283, 284] and beneficial changes to the cell architecture as reviewed in the last chapter.[152, 155, 184, 195, 285] A typical structure of PbS CQDs single-junction solar cells is shown in Figure 3-1. ZnO is a typical electron transport layer for this cell structure. Recently, modifications to the

electron transport layer (ETL) have shown potential for improving solar cell performance.[286-290] Further developing this essential electron transport layer creates a new avenue to improve CQD solar cell efficiencies.
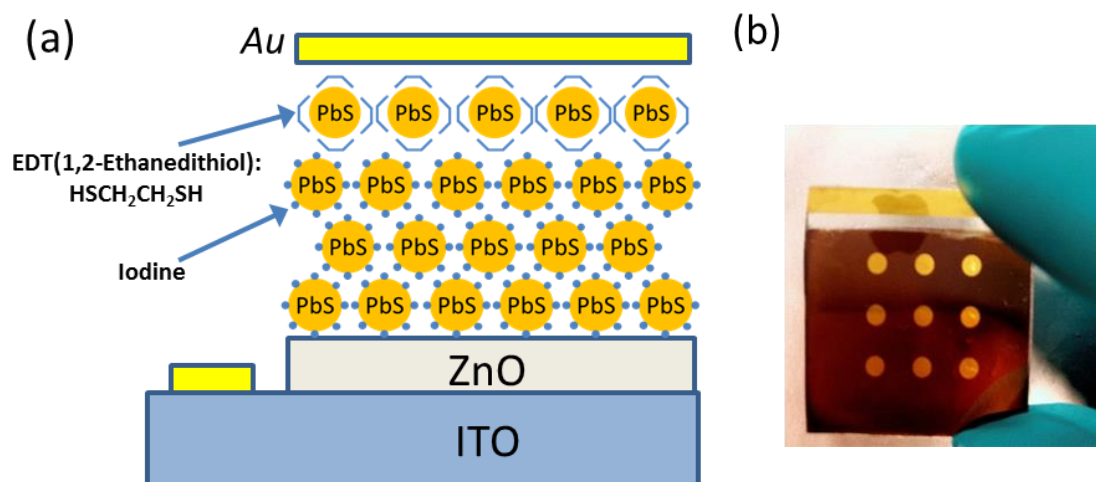
Figure 3-1 (a) A scheme of a typical PbS CQD solar cell structure. This structure is composed of ITO substrate, electron transport layer (ZnO), n-type PbS CQD layer (PbS-I) and p-type PbS CQD layer (PbS-EDT) (b) A photo of a fabricated PbS CQD solar cell.

ZnO nanoparticle electron transport layers have been used extensively in quantum dot solar cells as well as other thin film solar cells such as perovskite and polymer cells. This is because of their high transparency, high charge carrier mobility, high electron affinity, facile synthesis and low crystallization temperature.[286, 291-295] One remaining problem with ZnO nanoparticles is their surface defects. The large surface-to-volume ratio of ZnO nanoparticles turns the nanoparticle surface defects into a significant problem. A large amount of defects can trap electrons resulting in reduced charge transport and these defects can also cause surface defect induced recombination that could lead to both reduced V_{OC} and J_{SC}.[294-297] Though reduction of ZnO nanoparticle surface defects has been studied by introducing interlayers, [278, 288, 298] organic passivators [288, 299, 300] and inorganic passivators, [287, 298, 301-305] further reduction in ZnO nanoparticle defects can still significantly improve the performance of colloidal quantum dot devices.

Utilising NaCl to passivate ZnO nanoparticles has shown its potential to improve electron transport layers, [306] and Choi et al [306] have used this strategy to create a high efficiency of 11.6% for PbS CQD solar cells. According to Choi's work, the anion Cl⁻ has shown that it can reduce surface defects by passivating surface oxygen vacancies and the PbS CQD solar cell performance has been improved by this. However, the residual Na^+ cations did not show any effect on PbS CQD solar cell performance.[306]

Also, Mg^{2+} doping of ZnO has been studied as an effective method to improve ZnO electron transport layers by increasing transparency and by enlarging their bandgap.[307, 308] Inspired by these works and in order to combine benefits from both, Cl⁻ and Mg^{2+} treatments, a simple $MgCl_2$ treatment has been developed in this work to passivate ZnO nanoparticle surfaces and optimize the electron transport layer for PbS CQD solar cells. By this one simple chemical treatment, three effects, reduction in defects, increased transparency, and improved carrier extraction were achieved. The PbS CQD solar cell with the $MgCl_2$ treated electron transport layer achieved an efficiency of 8.2%, while an efficiency of 6.3% was acquired by the device without the $MgCl_2$ treatment. For the device with $MgCl_2$ treated ZnO electron transport layer, both the FF and J_{SC} were increased after the treatment.

3.2 Method

3.2.1 Preparation of ZnO-$MgCl_2$ nanoparticles

ZnO nanoparticles were synthesized following a previously reported method.[280, 306, 309, 310] A solution of potassium hydroxide (2.95 g) in methanol (125 ml) was added slowly, dropwise, into a solution of zinc acetate dehydrate (1.48 g) in methanol (65 ml) at 60°C. Then, the solution was stirred at 60°C for 2 hours. ZnO nanoparticles were extracted by centrifuging and washed using methanol twice. ZnO nanoparticles were finally re-dissolved in a mixed solvent containing chloroform and methanol. For $MgCl_2$ treatment, based on the previously reported optimal ratio [306], a mole ratio of Mg : Zn = 1 : 50 was made by adding 0.3 ml $MgCl_2$-methanol solution with a concentration of 0.7 mmol/ml drop-wise into 10 ml of the as-synthesized ZnO nanoparticle solution. The final solution was stored overnight to let the reaction complete before being used. The same percentage of methanol was also added to the pristine ZnO nanoparticle solution in order to maintain the same ZnO concentration with the $MgCl_2$ treated samples.

3.2.2 Preparation of PbS quantum dots

PbS quantum dots were synthesized by following previously reported methods [147, 306, 311]. 1-octadecene (ODE, 5 g) was degassed overnight and then mixed with Bis(trimethylsilyl)sulfide (TMS, 0.144 g). In the meantime, a mixture of PbO (0.45 g), Oleic acid (OA, 1.8 g) and ODE (10 g) was heated to 100°C for 3 hours under vacuum. The mixture was then cooled down to 90°C followed by injection of the TMS/ODE mixed solution. Then the heating mantle was removed and the mixture was left to cool down naturally. The as-synthesized PbS CQDs were purified three times using acetone as anti-solvent and hexane as solvent. The as-synthesised quantum dots were averagely divided into 4 centrifuge tubes (50 ml in volume). For each centrifugation, 20 ml hexane was added to dissolve quantum dots and then 30 ml acetone was added as anti-solvent. A spinning speed of 6000 rpm was usually used for centrifugation process. The purified final quantum dots were dispersed in hexane (30 mg/ml in a typical synthesis).

3.2.3 Fabrication of PbS CQD cells

ITO coated glass substrates were cleaned using detergent, distilled water, IPA (isopropyl alcohol) and acetone, respectively. Then the substrate was UV-Ozone cleaned for 30 min. The $MgCl_2$ treated ZnO-NP solution (or pristine ZnO NP solution) was spin-coated onto the cleaned ITO glass at 2500 rpm for 30 s. This process was repeated twice and the samples were stored at room temperature in air for an hour to dry out the solvent. Then, the PbS-OA CQD solution was spin-coated onto the ZnO-NP film at 3000 rpm for 30 s. Next, the as-cast PbS-OA film was soaked in PbI_2 (4.6 mg/ml in DMF) for 45 s for ligand exchange. From this, a layer of PbS quantum dots with iodine ligands (PbS-I) was obtained. Then, the PbS-I layer was rinsed with acetonitrile (ACN) multiple times to remove the residual ligands. The PbS-I layer fabrication process was repeated 8 times to produce a 280 nm thick intrinsic PbS-I absorber layer. For the deposition of the hole transport layer, ethanedithiol (EDT) was used for ligand exchange to form a PbS-EDT layer. EDT (0.015% vol in ACN) instead of PbI_2 was used as ligand source to treat the PbS-OA quantum dot layer, which was finally washed with ACN. Two layers of PbS-EDT were deposited onto the PbS-I layer. Finally, 100 nm of Au was deposited by thermal evaporation onto the CQD film as an electrode. The cell area was 0.03 cm^2 defined by the size of the Au electrode.

All chemicals were purchased from Sigma-Aldrich and used as received.

3.2.4 Materials characterisation

X-ray diffraction (XRD) was performed on a PANalytical X'pert Materials Research Diffractometer. A Cu Kα radiation source (λ = 0.1541 nm) was used at 45 kV and 40 mA with the sample measured in air. The film samples of pristine ZnO and $MgCl_2$ treated ZnO were spin-casted on pure glass substrates. XRD was performed for analysing the materials' crystal structures.

X-ray Photoelectron Spectroscopy (XPS) and Ultra-violet Photoelectron Spectroscopy (UPS) were performed using an ESCALAB250Xi system produced by Thermo Scientific (UK). The X-ray source was a mono-chromated Al K alpha (energy 1486.68 eV) and the ultraviolet source was a He Iamp (energy 21.2 eV). The ZnO (or $MgCl_2$ treated ZnO) sample for XPS and UPS measurements were spin-coated films onto ITO substrates. The estimated thicknesses were 500-1000 nm. XPS measurement was carried out mainly for analysing elemental compositions while band offset information could be derived from UPS spectra.

The transmission and reflection spectra were measured on a Perkin Elmer Lambda1050 UV/Vis/NIR spectrophotometer. The T&R measurement is for analysing the samples' optical properties. The samples were nanocrystals spin-casted onto ITO glasses in the same condition with processing solar cells.

The Raman Photoluminescence (PL) measurement was performed on a LabRAM Raman system. An excitation laser of 325 nm was used. Sample films with more than 100 nm thickness were fabricated to fully absorb the excitation light. The intensity of Raman-PL peaks could represent in-gap defects, so that the level of passivation can be analysed by these curves. The relatively thick (~800 nm) sample films for ZnO (or $MgCl_2$ treated ZnO) was spin-casted onto pure glass substrates.

Scanning electron microscope (SEM) images were obtained using a FEI Nova Nano 450 SEM. Samples for surface SEM images were ZnO (or $MgCl_2$ treated ZnO) films spin-casted on ITO glasses in the same condition with processing solar cells. Cross-sectional SEM image was taken for analysing the solar cell's laminar information.

FT-IR measurements were performed on a Spotlight 400 FT-IR system. The KBr pellet method and transmission mode were used in this measurement. The scanning range was from 1000 cm^{-1} to 450 cm^{-1}. ZnO (or $MgCl_2$ treated ZnO) powders were added to KBr powders

followed by compressing the mixture into a pellet. FT-IR measurement could give the samples' composition and bonding information.

Photoluminescence (PL) measurement for PbS solution is conducted by a Horiba Photoluminescence System. PbS solution is contained in a quartz cuvette. Excitation light with a wavelength of 600 nm was used.

3.2.5 Device characterisation

The current density–voltage (J-V) measurements were performed using an IV5 solar cell J-V testing system from PV measurements, Inc. with a Keithley 2400 source meter and an AM1.5G Oriel model 94023A solar simulator. The incident illumination power is 1000 W/m^2. A forward scan from -0.25 V to 0.75 V was used.

External quantum efficiency (EQE) measurements were performed on a PV Measurement QXE7 spectral response system with monochromatic light generated from a xenon arc lamp.

All characterizations were performed at room temperature in ambient conditions except the XPS, UPS and SEM analyses, which were carried out in a vacuum chamber.

3.3 Improved single-junction PbS CQD solar cell
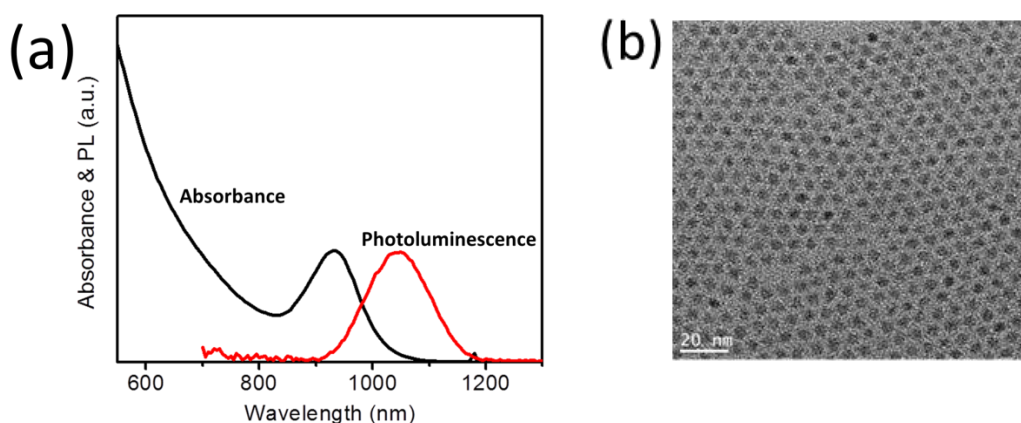
Figure 3-2 (a) Absorbance and photoluminescence of synthesised a PbS quantum dot sample. The absorbance exciton peak centres at 933 nm while the photoluminescence curve peaks at 1041 nm. The half widths at half max of two peaks are both ~120 nm. (b) TEM image for PbS quantum dots. The average size of synthesised PbS quantum dots is ~4 nm.

For fabricating PbS CQD solar cells, PbS CQDs were synthesised in the first place. Figure 3-2(a) shows the absorbance and photoluminescence (PL) for synthesised PbS solution. The quantum dots bandgap is 1.33 eV as indicated by the absorbance peak at 933 nm. The half width at half max (HWHM) of absorbance peak is ~120 nm, indicating a relatively narrow size distribution.[312] The Stokes shift (~110 nm) between the PL and absorbance peaks is minimal [312] and the PL emission peak is similarly narrow as compared to absorption. TEM image of synthesised PbS CQDs is shown in Figure 3-2(b). The average size of quantum dots is ~4 nm, which is consistent with Moreels' empirical equation[71] describing the relationship between bandgap and size reviewed in Chapter 2.1.1.

PbS CQD solar cells were fabricated using synthesised PbS quantum dots. $MgCl_2$ treated ZnO nanoparticles were utilised to form the electron transport layer for improving the single-junction PbS CQD solar cell. The cell's structure consists of glass/ITO/ZnO-$MgCl_2$/PbS-I/PbS-EDT/Au. Also, a control cell was made using the untreated pristine ZnO electron transport layer. The cell structure is shown in the cross-sectional SEM image in Figure 3-3.

The fabrication process of PbS CQD solar cell is described briefly here. First, a ZnO-$MgCl_2$ solution was spin coated onto cleaned ITO glass to form a ZnO-$MgCl_2$ film. Then, this process was repeated once again to form two layers of ZnO-$MgCl_2$ for reducing pin-holes in the electron transport layer. Following the fabrication of ZnO-NPs layer, PbS quantum dot layers, including both "i-type" (PbS-I) and "p-type" (PbS-EDT) layers, were fabricated by a layer-by-layer process as detailed in the Methods. A control cell was then made using the pristine ZnO nanoparticle solution for comparison with ZnO-$MgCl_2$ nanoparticles.

The J-V curves of PbS quantum dot solar cells are shown in Figure 3-4. An 8.2% power conversion efficiency can be achieved by using $MgCl_2$ treated ZnO nanoparticles, compared to the efficiency of 6.3% for the control cell using pristine ZnO nanoparticles. The increase of power conversion efficiency is mainly attributed to the increase in the FF. A FF of 62% has been achieved using $MgCl_2$ treated ZnO nanoparticles, compared to a FF of 53% for the cell using pristine ZnO nanoparticles. An increase in J_{SC} also contributed to the improved device efficiency. The J_{SC} of the cell with ZnO-$MgCl_2$ electron transport layer is 21.9 mA/cm^2 compared to 19.6 mA/cm^2 for the cell with pristine ZnO electron transport layer. EQE results (Figure 3-5) also exhibit an increase in current density, 20.8 mA/cm^2 for the treated cell compared to 18.6 mA/cm^2 for the control cell, which is consistent with the J-V curve results.
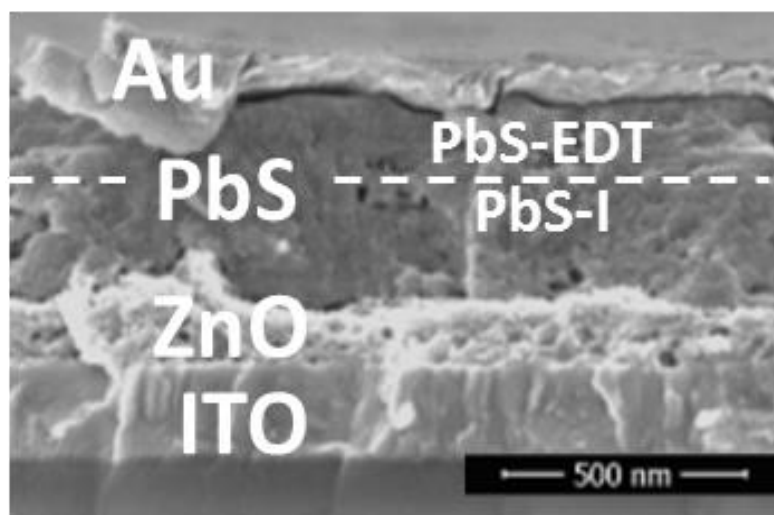
Figure 3-3 SEM cross-sectional image of a PbS CQD solar cell with a glass/ITO/ZnO-MgCl₂/PbS-I/PbS-EDT/Au layer stack. The thickness of the ZnO film is 120 nm, the PbS-I CQD film is ~280 nm and the PbS-EDT layer is ~100 nm. EDT is short for 1,2-Ethanedithiol (HSCH₂CH₂SH).
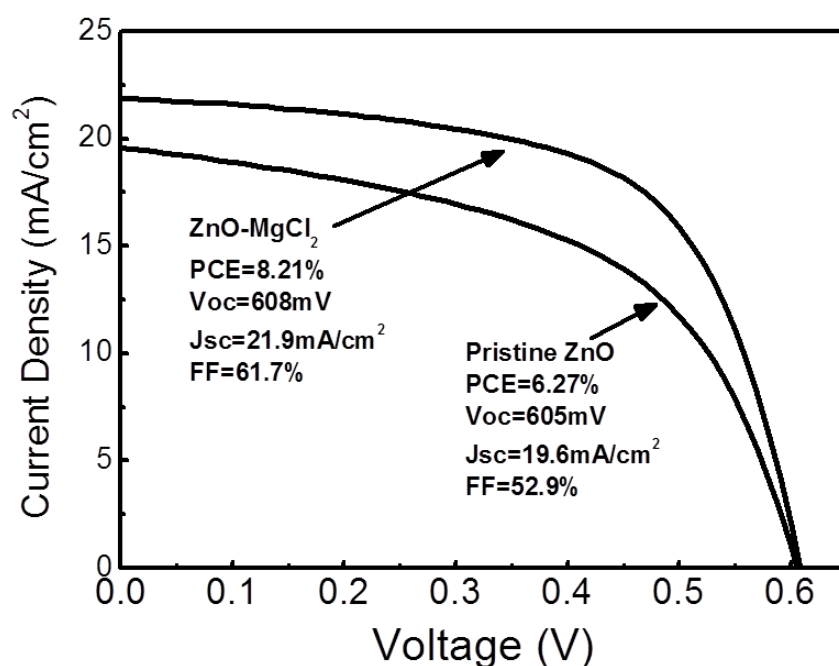
Figure 3-4 The J-V curves of the PbS CQD solar cell using ZnO-MgCl₂ electron transport layer and a control cell using pristine ZnO electron tansport layer. With MgCl₂ treated ZnO-NPs electron transport layer, the cell efficiency increased from 6.3% to 8.2%, and J_{SC} increased from 20 mA/cm² to 22 mA/cm², and fill factor increased from 53% to 62%.

Table 3-1 Solar cell parameters obtained from the J-V curves. With MgCl₂ treatment, the cell's shunt resistance was reduced while the series resistance was increased.

Device	J_{sc} (mA/cm^2)	V_{oc} (mV)	FF	PCE	R_{sh} (Ohm·cm^2)	R_s (Ohm·cm^2)
ZnO-MgCl₂	21.9	608	62%	8.2%	205	3.5
Pristine ZnO	19.6	605	53%	6.3%	103	5.0
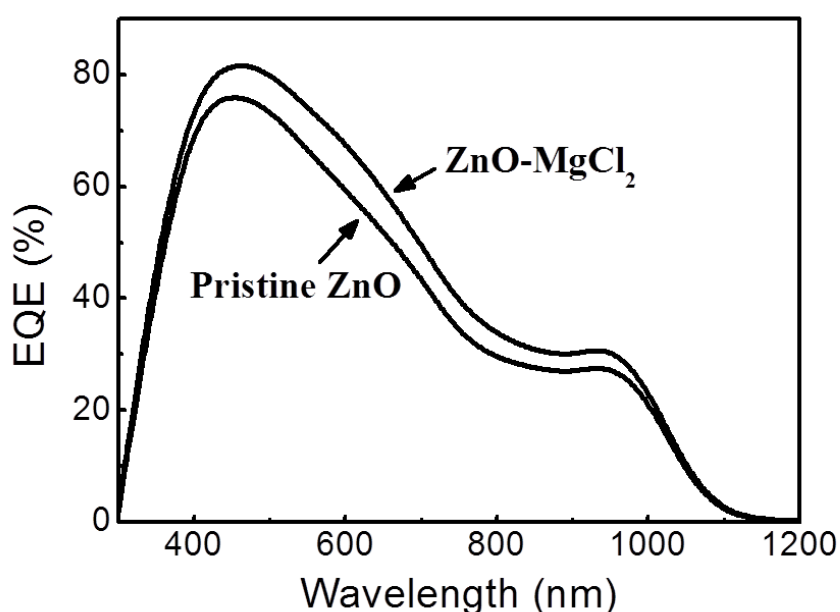
Figure 3-5 The EQE spectra of PbS CQD soalr cell with ZnO-MgCl₂ electron transport layer and a control cell using pristine ZnO electron transport layer. A broadband increase in EQE for the cell with ZnO-MgCl₂ electron transport layer was shown compared that for the cell with pristine ZnO, which is consistent with improved charge carrier collection.

Table 3-1 lists parameters for both PbS CQD solar cells with MgCl₂ treated ZnO electron transport layer and with pristine ZnO layer. Utilising PVlighthouse J-V curve fitting function, shunt and series resistances can be calculated based on J-V curves. With MgCl₂ treatment the shunt resistance R_{SH} increased and the series resistance R_S decreased. R_{SH} increased to 205 Ohm·cm^2 from 103 Ohm·cm^2 after ZnO-NP surface passivation with the MgCl₂ treatment,

indicating less leakage current and possibly less interface defect-mediated recombination. R_S decreased from 5.0 Ohm·cm^2 to 3.5 mOhm·cm^2, which indicates less ohmic loss and possibly better charge collection in the solar cells. The following sections 3.2 and 3.3 in this chapter would show detailed characterisation for that the improved device performance is possibly from reduced ZnO-NP surface defects passivated by MgCl$_2$ treatment hence improving the FF and J_{SC} and improved band alignment for the PbS CQD solar cell.

3.4 MgCl$_2$ treated ZnO electron transport layer with reduced detects

Figure 3-6 illustrates the method of making a MgCl$_2$ treated ZnO nanoparticle solution and shows the mechanism of nanoparticle passivation. To perform the MgCl$_2$ treatment, 0.3 ml of MgCl$_2$ solution (0.7 mmol/ml) was added dropwise into the as-synthesized ZnO nanoparticle solution (10 ml).
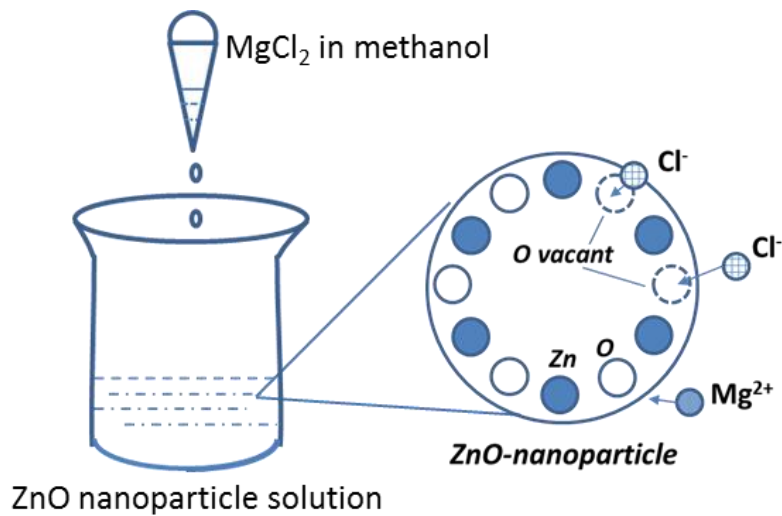
Figure 3-6 Illustration of the MgCl$_2$ treatment of ZnO nanoparticles in solution and the mechanism for the elimination of defects. MgCl$_2$ is added to the ZnO nanoparticle solution at ambient temperature.

To characterise the effect of $MgCl_2$ on the ZnO nanoparticle electron transport layer, a series of measurements including XRD, FT-IR, XPS, Raman-PL, UV-vis, SEM and UPS were carried out.

Firstly, the XRD patterns of both $ZnO-MgCl_2$ and the pristine ZnO samples are shown in Figure 3-7. From these patterns, the three main peaks for the (100) (002) and (101) crystal planes are shown for both samples. These three peaks are characteristic of the ZnO hexagonal wurtzite crystal phase.[313-315] This means both materials have the wurtzite structure. A further conclusion from this is that the ZnO crystal structure remains the same after the $MgCl_2$ treatment. The reason for this can be that the added $MgCl_2$ only treats the surface of the nanoparticles as $MgCl_2$ diffusing into the crystal can be difficult at room temperature. Hence, the crystal structure of the ZnO nanoparticles was unaffected by the $MgCl_2$ treatment. The increase of intensity of ZnO (002) peak is possibly driven by the overlaped signal from residue $MgCl_2$ from which the diffraction peak intensity at ~34° is relatively high.[316-319]
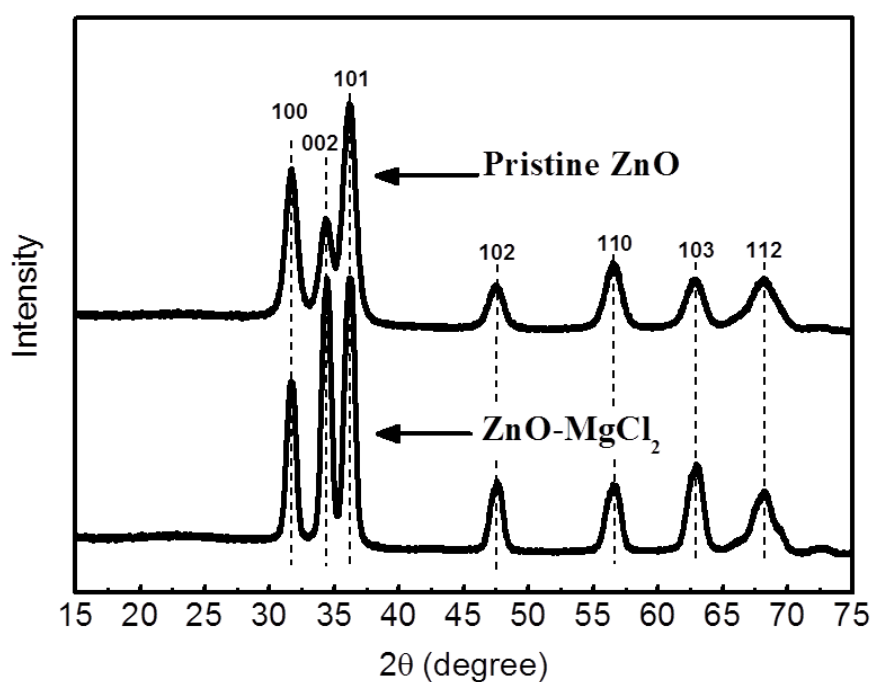
Figure 3-7 XRD patterns of both $ZnO-MgCl_2$ and pristine ZnO. From these patterns, three main peaks (100) (002) and (101) of the ZnO hexagonal wurtzite phase are shown in both curves. These XRD patterns indicate that the $MgCl_2$ treatment does not change the ZnO crystal structure.

To further investigate the bonding of the elements, FT-IR measurements were performed. As can be seen from Figure 3-8, the peak at 520 cm^{-1} is a sign of a vibration in ZnO which appears for both pristine ZnO and ZnO-MgCl$_2$ samples. The MgO symmetric vibration gives a peak at 470 cm^{-1} for the ZnO-MgCl$_2$ sample only. This peak is rather weak, as the amount of MgCl$_2$ is small. The appearance if this peak usually indicates that the formation of Mg-O bonds.[313-315]
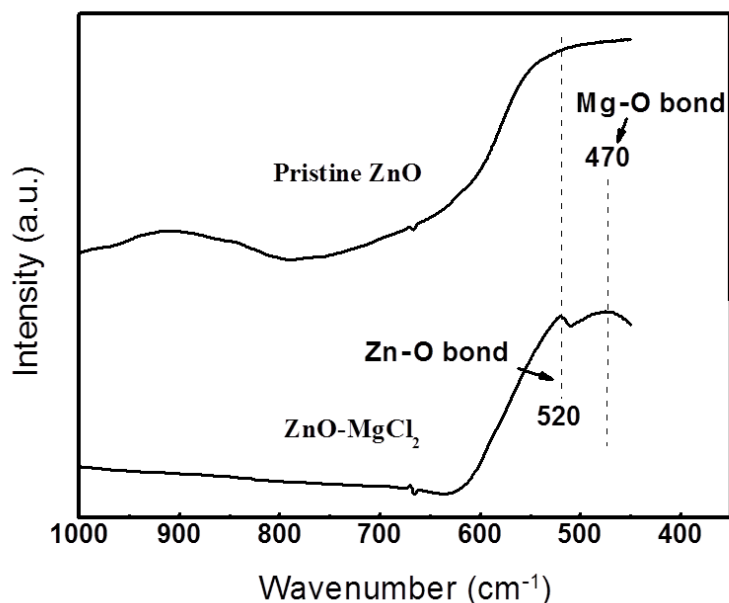
Figure 3-8 FTIR spectra of both pristine ZnO and ZnO-MgCl$_2$. The peak at 520 cm^{-1} is a sign of the Zn-O bond which is shown for both pristine ZnO and ZnO-MgCl$_2$ samples. The MgO symmetric vibration gives a peak at 470 cm^{-1} for the ZnO-MgCl$_2$ sample only.

Then, X-ray photoelectron spectroscopy (XPS) was performed to investigate the components of nanoparticles and the effect of the treatment. As shown in Figure 3-9(a) and Figure 3-9(b), the incorporation of Mg and Cl in the ZnO film is evident from the presence of the Mg 1s peak at 1304 eV and the Cl 2p peak at 198 eV after MgCl$_2$ treatment.[306, 320] The Mg 1s peak at 1304 eV indicates the formation of Mg-O bonds [320] while the Cl 2p peak at 198 eV indicates the formation of Zn-Cl bonds.[321] As can be seen in Figure 3-9(c), with the MgCl$_2$ treatment the shift of the Zn 2p peak from 1021.6 eV to 1022.1 eV also indicates the formation of Zn-Cl bonds.[306, 322, 323]
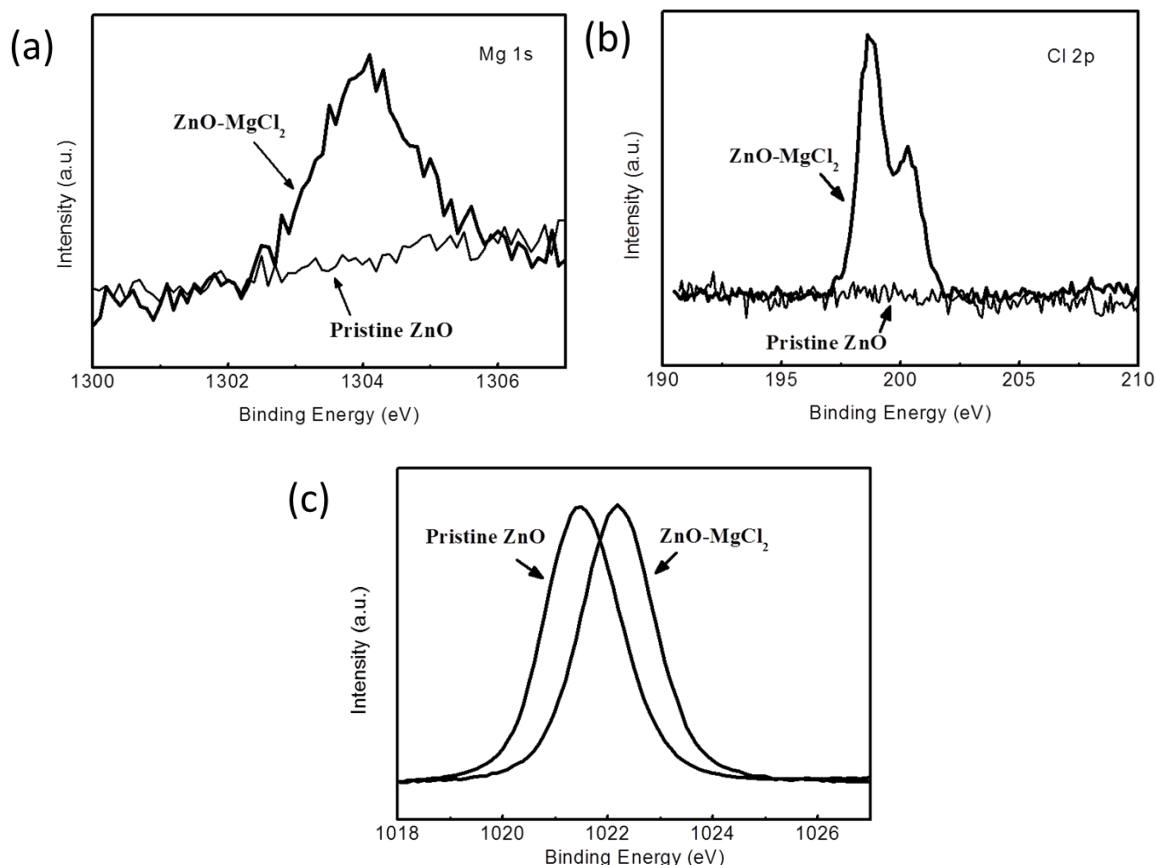
Figure 3-9 (a) XPS Mg 1s spectra for both pristine ZnO and ZnO-MgCl$_2$ films. (b) XPS Cl 2p spectra for both pristine ZnO and ZnO-MgCl$_2$ films. The appearance of the Mg 1s and Cl 2p peaks in (a) and (b) indicates incorporation of Mg and Cl elements into the MgCl$_2$ treated ZnO nanoparticles film. (c)XPS spectra of the Zn 2p peak for both, pristine ZnO and ZnO-MgCl$_2$, samples. For the ZnO-MgCl$_2$ sample, the peak of Zn 2p is 1022.1eV, compared to that of pristine ZnO's 1021.6 eV. This shift indicates the formation of Zn-Cl bonds.

Figure 3-10 shows Raman photoluminescence spectra for both pristine ZnO and MgCl$_2$ treated ZnO electron transport layers. This photoluminescence measurement employed an excitation wavelength of 325 nm. In Figure 3-10, the peak at 370 nm represents band-edge emission caused by radiative annihilation of excitons while the broad emission peak at 550 nm (2.25 eV) is attributed to defect emission from deep levels in the bandgap.[298, 324-326] The decrease in the defect emission peak indicates a reduction in surface defects due to the MgCl$_2$ treatment. Combining with XRD, FT-IR and XPS measurements, a possible mechanism for this treatment can be that the cation Mg^{2+} forms a Mg-O bond on the surface of the

nanoparticles, while the anion Cl⁻ provides compensating charge for the oxygen vacancies on the nanoparticle surface.
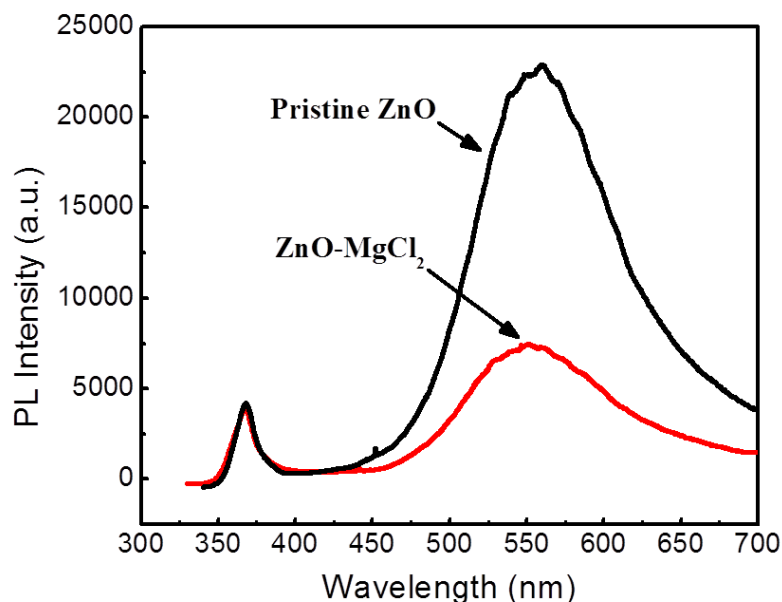
Figure 3-10 PL spectra of pristine ZnO and ZnO-MgCl₂ films. The peak at 370nm represents band-edge emission caused by radiative recombination. The reduction in the peak between 450 nm and 700 nm is attributed to a reduction of surface defects.

3.5 MgCl$_2$ treated ZnO electron transport layer with improved transparency

For current PbS CQD solar cells, electron transport layers are located in front of absorbing layers, so that the optical properties of the electron transport layers are significantly influencing solar cells' performance. In this section, the transmission and reflection of the ZnO nanoparticle electron transport layers are measured by UV-vis.

Increasing the transparency of ZnO layers by introducing Mg is another positive outcome from this treatment.[307, 308] With the very small amount of MgCl$_2$ incorporated into the synthesis, an increase of approximately 3% in transmission was observed from MgCl$_2$ treated ZnO films (Figure 3-11). Unlike the Mg-doped ZnO film fabricated by the sol-gel method, the bandgap of our ZnO-MgCl$_2$ film only shows minor enlargement (ca. 0.01 eV) as shown in Figure 3-11(c). (The method of plotting Tauc-plot for projecting bandgaps is from reported

papers.[306, 327]) This can be attributed to the $MgCl_2$-treated nanoparticles in this work where Mg^{2+} has bonded to the particle surface instead of merging into ZnO nanoparticle. Hence it has not significantly altered the band structure. In contrast, the sol-gel method generally incorporates Mg atoms into the ZnO lattice, changing the band structure.[200, 307]
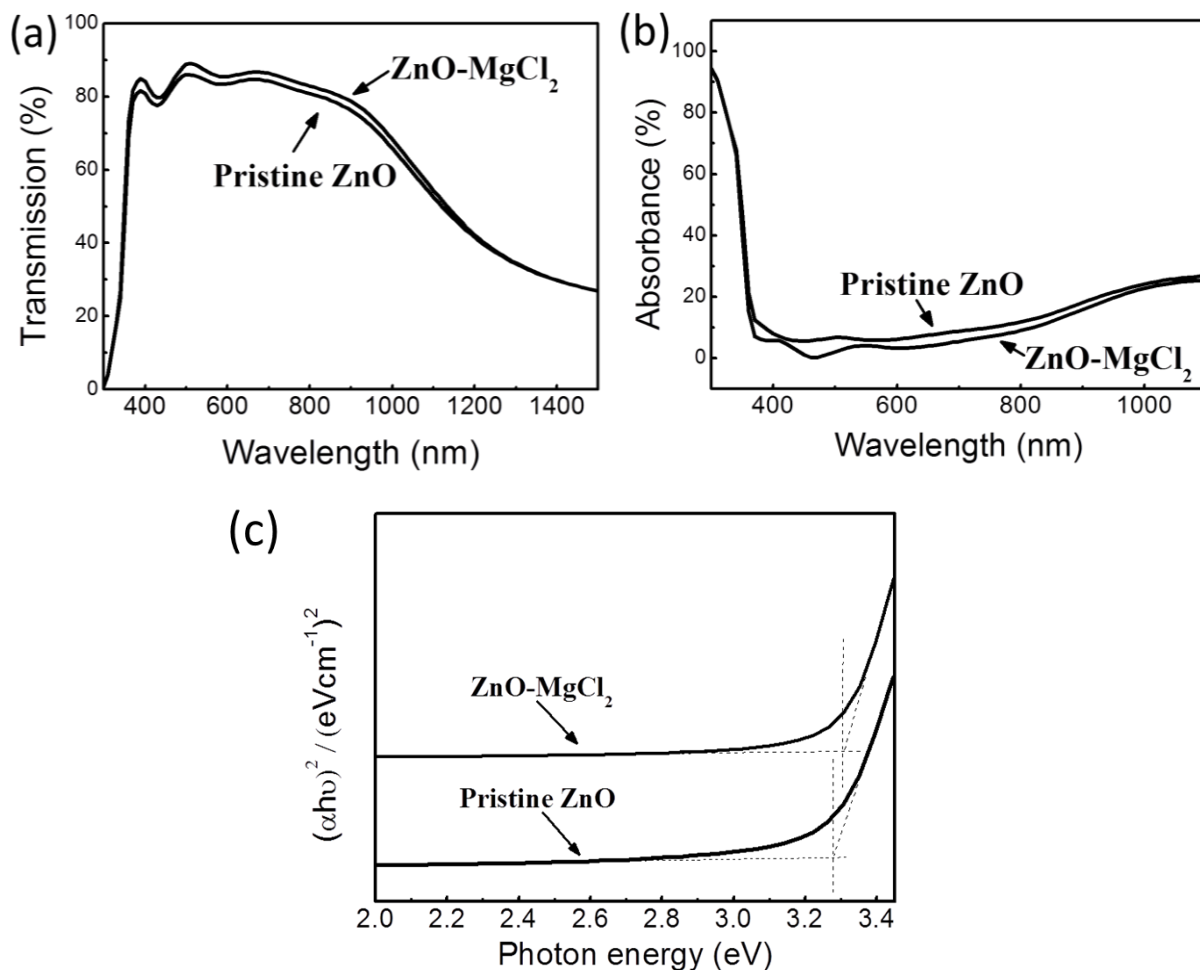
Figure 3-11 (a) Transmission of both ZnO-MgCl$_2$ and pristine ZnO films. With the very small amount of MgCl$_2$ incorporated, an increase of approximately 3% in transmission can be observed (b) Reflectance of both ZnO-MgCl$_2$ and pristine ZnO films. (c) Tauc plot of both ZnO-pristine and ZnO-MgCl$_2$. The bandgap of ZnO is only slightly shifted.

SEM images for the pristine ZnO film and $MgCl_2$ treated ZnO films are shown in Figure 3-12. The surface passivated ZnO film has a reduced the amount of pinholes as compared to that of the pristine ZnO film. The possible reason is that a better solubility of the surface

treated ZnO leading to a denser spin-coated film. This can further increase current density in a solar cell because these pinholes act as shunting centres leading to leakage current. Elimination of surface traps may also reduce charge carrier scattering by surface defects as carriers move between nanocrystals. This can increase ZnO electron transport layer conductivity, resulting in reduced series resistance (R_S) (Table 3-1). Also, the reduction of surface recombination centres can effectively increase the diode shunt resistance (R_{SH}) by reducing surface trap-assisted recombination.[294-297] Hence, an increase in both J_{SC} and FF can be expected.
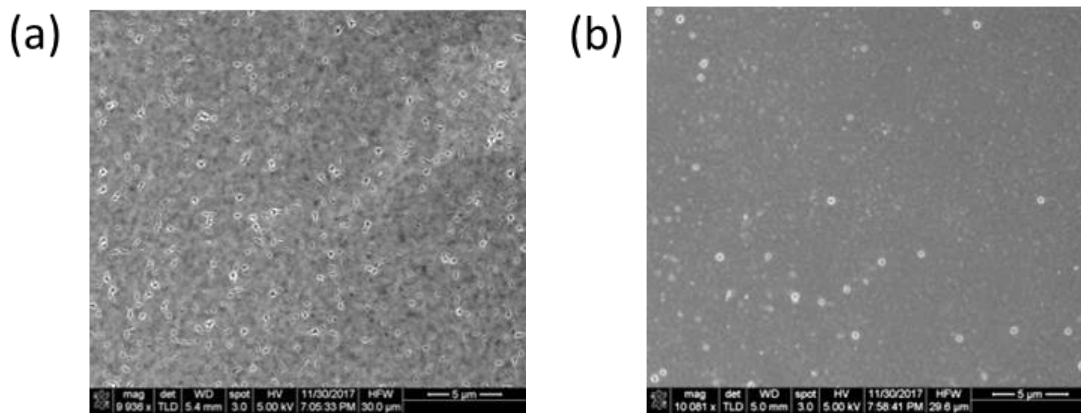
Figure 3-12 SEM images of (a) the pristine ZnO film and (b) MgCl$_2$ treated ZnO film. Pinholes are reduced significantly by using MgCl$_2$ treated ZnO nanoparticles.

3.6 Improved band alignment for PbS CQD solar cell

Ultraviolet photoelectron spectroscopy (UPS) was used to investigate the energy band structure of the ZnO-NP electron transport layer. The UPS spectra in Figure 3-13(a,b) show that the Fermi level (E_F) appears further away from the valence band (E_V) for the ZnO-MgCl$_2$ sample, where the difference between E_F and E_V is 2.3 eV for the pristine ZnO sample and 2.8 eV for ZnO-MgCl$_2$. The conduction band was shifted from -4.2 eV for pristine ZnO nanocrystals layer to -4.7 eV for the MgCl$_2$ treated ZnO electron transport layer. This means a larger electrical field for the heterojunction with MgCl$_2$ treated ZnO in a solar cell.[308] Figure 3-13(c) schemes the charge transport in the interface area. With a larger electrical field, an enhanced charge extraction was achieved and interfacial recombination can be reduced due to minimised charge accumulation.[308]
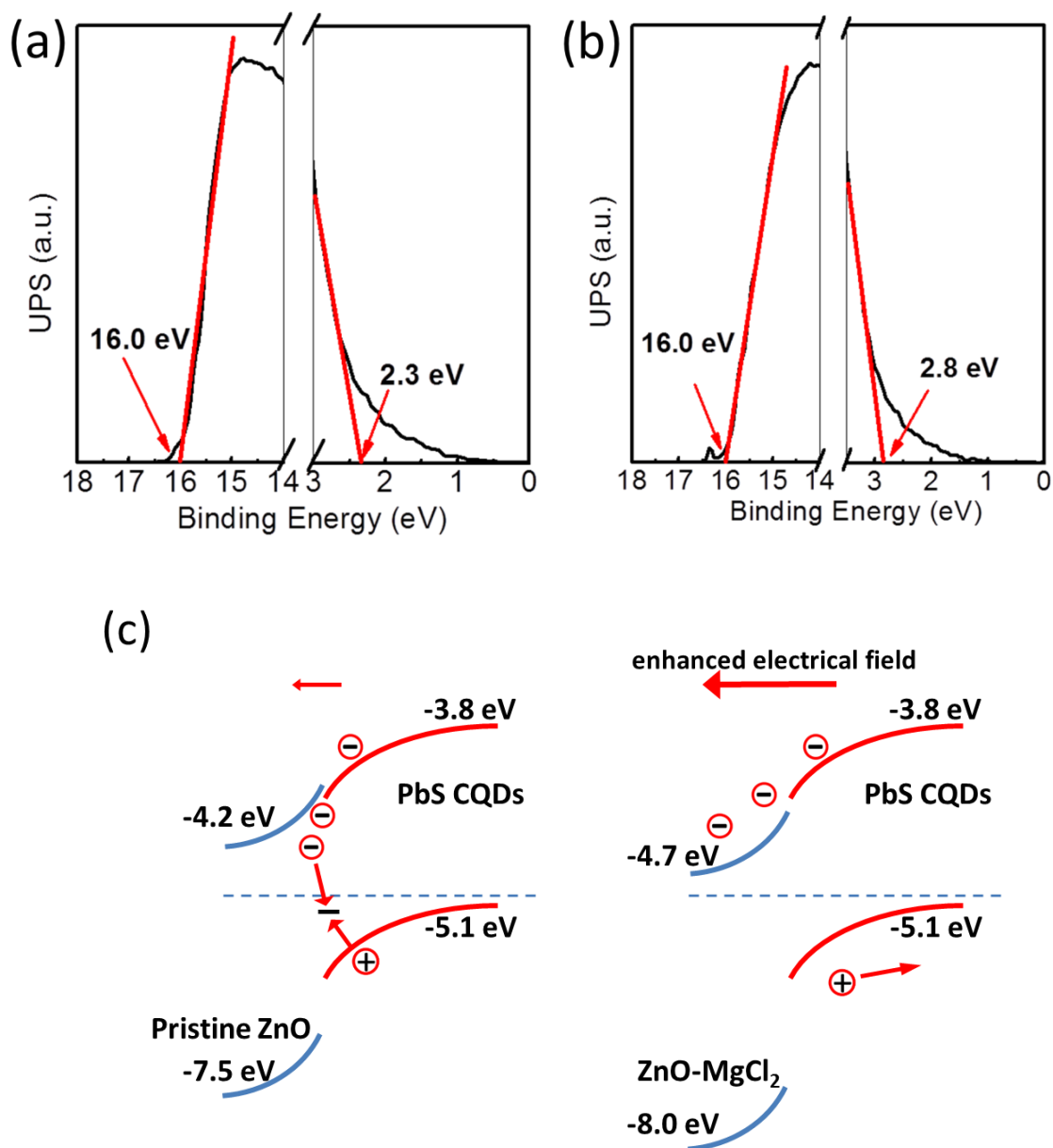
Figure 3-13 UPS of ZnO nanocrystals before (a) and after (b) applying MgCl$_2$ surface treatment. By applying this treatment, the ZnO nanocrystals' conduction band was observed to shift from -4.2 eV to -4.7 eV. (c) A scheme for electron extraction before and after MgCl$_2$ doping. The PbS CQDs bandgaps refer to reported values.[328, 329] The doped nanoparticles caused larger build-in electrical field and reduced defects. More efficient electron extraction due to higher build-in electrical field reduced charge carriers' accummulation at the interface area for the solar cell with MgCl$_2$ treated ZnO electron tranport layer.

3.7 Conclusion

In conclusion, in this chapter a simple $MgCl_2$ treatment of ZnO nanoparticles has been reported which has improved the efficiency of PbS CQD solar cells. With the simple one-step treatment, the combined benefits of both, Mg^{2+} and Cl^-, passivation on the ZnO nanoparticle surface can be obtained. Not only surface defects were reduced by this simple trreatrment, but also an increased transmittance was observed for the treated film. Moreover, a down-shifted conduction band of ZnO-$MgCl_2$ ETL formed a better band alignment in the cell leading to more efficient carrier extraction. These improvements have led to a PCE of 8.2% in a PbS quantum dot solar cell relative to a PCE=6.3% for a control cell with a pristine ZnO electron transport layer. As a material that can be processed at low-temperature, this $MgCl_2$ treated ZnO electron transport layer can also be applied to other type of thin film single-junction cells. Hence, the development of this improved ZnO-NP layer may contribute to further improvements in solar cell efficiencies.

Chapter 4. Modelling of PbS CQD Tandem Solar Cell Structure

Tandem solar cell is a promising strategy for increasing solar cell efficiency and PbS quantum dots are suitable absorbing material for constructing tandem solar cells due to their tunable bandgaps. While single-junction PbS CQD solar cells have achieved an efficiency of above 12%,[2] PbS CQD tandem solar cells with record efficiency of 8.9%[77] have lagged far behind the development of their single-junction counterparts. A major challenge for making a high performance quantum dot tandem solar cell as well as other tandem solar cells is the current matching problem. The currents from front and rear subcells could easily fall into a mismatched situation because of the difficulty in designing absorbing layer thicknesses. For solving this problem, in this chapter, an optical modelling has been established mainly for guiding the design of absorbing layer thicknesses. With the optical constants obtained from ellipsometry, PbS CQD tandem solar cells' subcell bandgaps and absorbing layer thicknesses were simulated by the modelling. Different interlayers of Au and ITO were both analysed by this modelling. Though this modelling method has been widely applied on other kind of tandem cell analysis, it is rarely applied on quantum dot tandem solar cells currently.

Besides, a diode modelling was applied for simulating J-V curves for PbS CQD tandem solar cells in the later part of this chapter.

4.1 Introduction

For simulating a tandem cell structure, a few classical models have been developed and reported.[67, 261] The detailed balanced limit calculation [261, 330] is a classical model for multi-junction solar cells. This simulation is conducted under the following assumptions: (1) AM1.5G solar spectrum is applied; (2) all photons above the bandgap of the respective absorbing layer are absorbed, while each absorbing layer is completely transparent below the bandgap; (3) only radiative recombination happens in the whole process. Under these assumptions, the detailed balanced limit calculation shows that solar cells with one, two,

three and infinite junctions could achieve efficiencies of 33%, 42%, 49% and 68% respectively.[331] Luther et al [261] introduced a semitransparent film model based on the detailed balance limit model by waiving the second assumption mentioned above. The semitransparent film model assumes that by adjusting the thickness of an absorbing layer, a portion of photons above the bandgap could still transmit through this layer. Under this assumption, a PCE of above 40% can still be achieved for a tandem solar cell by this model. Besides, a semi-empirical modelling was introduced by Lingxian et al [67] for analysing organic tandem solar cells. Based on empirical values for EQE, V_{OC} and FF, the approximate PCEs of organic tandem solar cells can be obtained, which still gave acceptable results. However, these universally applied models can only give the theoretical upper limit by assuming ideal optical conditions for tandem cell performance. We need a model which incorporates material's experimental optical constants and thicknesses of absorbing layers to give a more accurate approximation to the tandem cell's performance.

An optical modelling has been applied to a perovskite-Si tandem cell, which showed very accurate prediction for the tandem cell's performance.[332] This optical model took optical constants into consideration employing a Ray-Tracing method to obtain absorbance and reflection of every functional layer. For constructing a high performance tandem solar cell in which current matching is a vitally important criterion, optical modelling considers specific absorbing layers in different cells and gives a more realistic guidance for tandem cell structure design. This is important because the more accurate the simulation is, the smaller mismatch of subcell currents in the real device exists and hence the smaller the current loss is in a tandem solar cell.

In this chapter, modellings for PbS CQD tandem solar cells were conducted for guiding experimental works. In the beginning part of this chapter, an optical modelling was applied for simulating PbS CQD tandem solar cells, as currents from front and rear subcells need to be adjusted to match with each other so that a tandem cell can have an optimised performance. The optical modelling was established by applying PVlighthouse Sunsolve module, where the a Ray-tracing method is mainly employed.[236] The optical constants of the simulated absorbing layers were obtained by Ellipsometry measurement and Cauchy model fitting. The modelled tandem cell structure is ITO glass / ZnO-NP / Front cell absorbing layer / Au or ITO / ZnO-NP / Rear cell absorbing layer / Au. Firstly, different subcell bandgaps were simulated for identifying the optimal subcells' bandgaps combination. Then, the tandem cells with different interlayer thicknesses were simulated and a proper interlayer thickness

was identified. Thirdly, tandem cells with different absorbing layers' thicknesses were also simulated. By adjusting currents from front cell and rear cell to match with each other, optimised absorbing layer and interlayer thicknesses can be obtained. Under optimised conditions, a matched current of 15.3 mA/cm^2 could be achieved in a quantum dot tandem solar cell. Besides optical modelling, in the later part of this chapter, J-V curves were also simulated based on both tandem and single-junction solar cells by combining diode equations and detailed balance limit modelling. PbS CQD tandem solar cell could reach an efficiency of ~15.5% according to this modelling.

4.2 Method

4.2.1 Optical simulation

Optical constants of PbS quantum dots: The optical constants of PbS quantum dot films were obtained by ellipsometry measurement and Cauchy model fitting using WVase software. Samples for ellipsometry measurement were PbS quantum dots films with different sizes made by spin-coating quantum dot ink onto silicon/silicon dioxide wafers. The thicknesses of quantum dot films were estimated using a cross-sectional scanning electrons microscope image. J.A. Woollam variable angle spectroscopic ellipsometry was used for this measurement. Three reflection angles of 55°, 65° and 75° were chosen to acquire data. The measurement was conducted under standard scan mode. The acquired data was fitted with a Cauchy model firstly to find the thickness and then use an all parameter fitting to extract the refractive index n and the extinction coefficient k over the whole wavelength range. This work was conducted by a collaborator Dr Weijian Chen.

EQE simulation: PVlighthouse Sunsolve module was employed for realising the optical modelling. EQEs for subcells in a PbS CQD tandem solar cell were simulated by this modelling. Optical parameters of PbS CQD absorbing layers were obtained from ellipsometry measurement and fitting while optical parameters of other functional layers were acquired from the PVlighthouse database.

4.2.2 J-V curve simulation

Simulated J-V curves were obtained by a diode modelling combined with J_{SC} obtained from the optical modelling. In this simulation, there are three basic assumptions: (1) The cell absorbance follows the above described optical modelling; (2) Radiative and Shockley-Read-Hall recombination both happen in the relaxation process; (3) Different lifetimes of charge carriers are considered in this model. Equations used in this model are listed below.[333, 334]

$$J_{front} = J_{rear} = J_{tandem} \tag{4-1}$$

$$V_{tandem} = V_{front} + V_{rear} \tag{4-2}$$

$$J_{front} = \int_{E_{front}}^{\infty} \Gamma(E)dE - J_{SHR} \tag{4-3}$$

$$J_{rear} = \int_{E_{rear}}^{\infty} \Gamma(E)dE - J_{SHR} \tag{4-4}$$

$$J_{SHR} = \frac{pn - n_i^2}{\tau_p(n + n_i) + \tau_n(p + p_i)} \tag{4-5}$$

When n>>p,

$$J_{SHR} = \frac{p_n - p_{n0}}{\tau_p} \tag{4-6}$$

$$p_{n0} = \frac{n_i^2}{n_D} \tag{4-7}$$

$$p_n = p_{n0}e^{(\frac{V}{V_T})} \tag{4-8}$$

Parameters used in this modelling were obtained from reported studies [333, 334].

4.3 Obtained optical constants and EQEs for mono-bandgap PbS CQD tandem solar cell

Parameters of *n* and *k* for PbS quantum dots films with different bandgaps are shown in Figure 4-1. Four bandgaps of 1.5 eV, 1.37 eV, 1.22 eV and 1.14 eV for quantum dots were measured and obtained by Cauchy model fitting as described in Method in section 4.2.
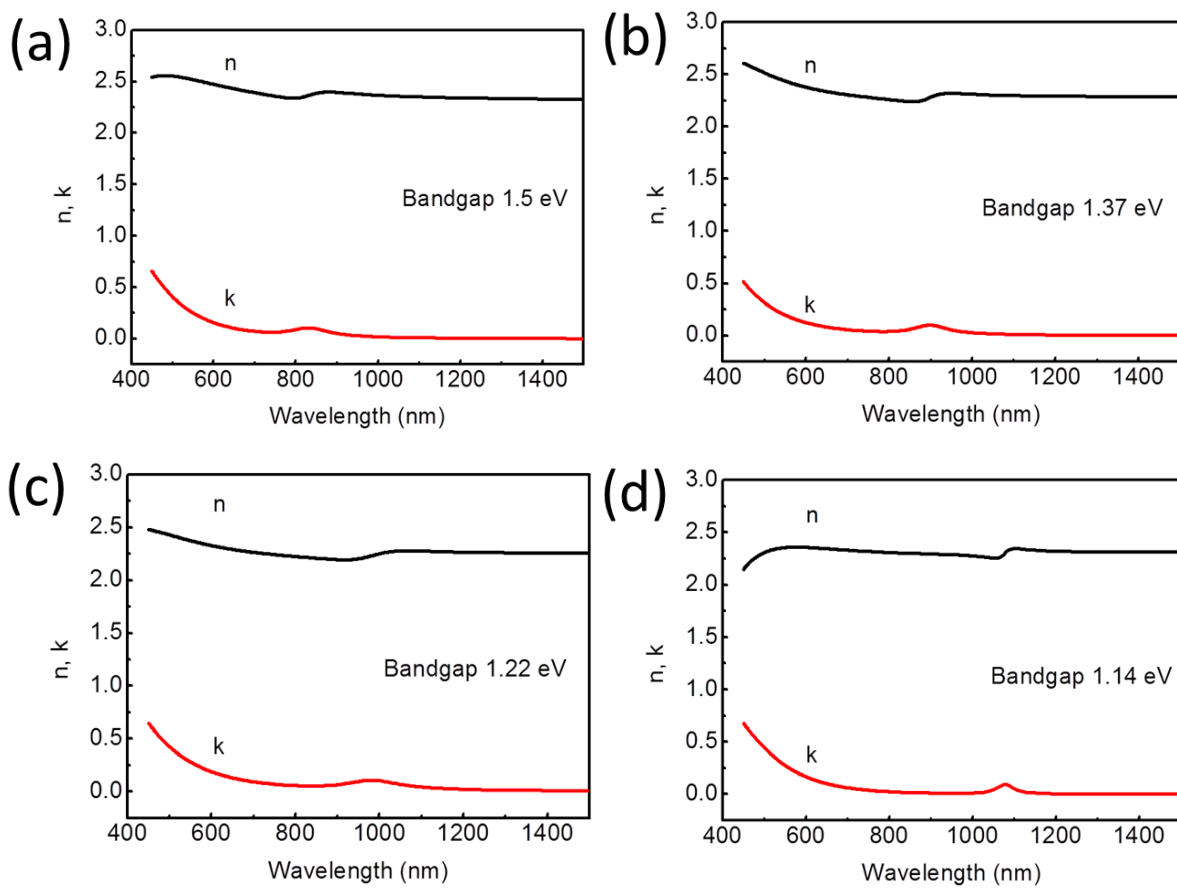
Figure 4-1 Optical constants n and k of PbS quantum dots with different bandgaps of (a) 1.5 eV, (b) 1.37 eV (c) 1.22eV, (d) 1.14 eV.
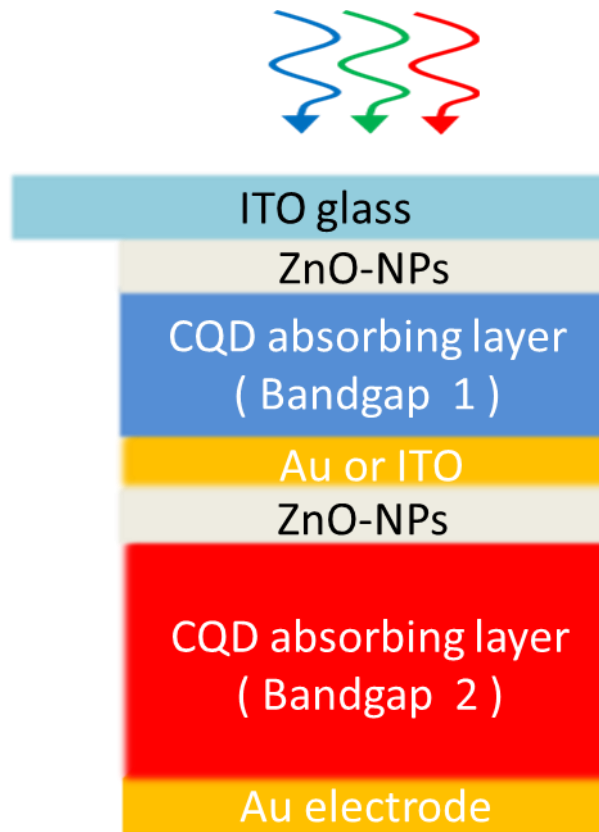
Figure 4-2 illustrates the modelled tandem cell structure in this chapter. Optical constants of n and k were input as parameters for each layer. Absorbing layers' optical constants were obtained from synthesised quantum dots films while other layers' (ZnO, Au and ITO) optical constants were borrowed from PVlighthouse library. Tandem cells with mono-bandgap subcells (Bandgap 1 = Bandgap 2) were investigated firstly, while tandem cells with different bandgaps' subcells (Bandgap 1 $\neq$ Bandgap 2) are presented in following sections.

Though a tandem cell usually employs two subcells with different bandgaps, researchers[77] have shown that using two subcells with the same bandgap still could achieve a higher efficiency than a single-junction CQD solar cell. The small diffusion length together with the resulted low absorbance of the CQD layer is limiting single-junction CQD solar cell's performance.[167, 171, 333] A mono-bandgap tandem cell structure could increase cell efficiency because the total thickness of the absorbing layers can be increased by employing tandem

structure and hence total absorbance could be enhanced. The total thickness of a mono-bandgap tandem solar cell could easily reach beyond diffusion length while a single-junction solar cell would be confined within this limit largely, so that the absorbance of a mono-bandgap tandem solar cell would be higher than that of a single-junction cell. According to NREL's simulation[261] introduced in Figure 2-3-2 in section 2.3.2, the efficiency can still reach ~33% for tandem cells with mono-bandgap subcells (~1.5 eV).

Figure 4-3 shows simulated EQEs of a mono-bandgap PbS CQD tandem solar cell with front cell and rear cell absorbing layer composed of quantum dots with the same bandgap of 1.5 eV. The simulated cell is in a structure of ITO glass/ZnO/front absorbing layer (1.5 eV)/ Au/ ZnO/rear absorbing layer (1.5 eV)/ Au contact. Simulated front and rear absorbing layers' thicknesses are 140 nm and 300 nm, respectively.
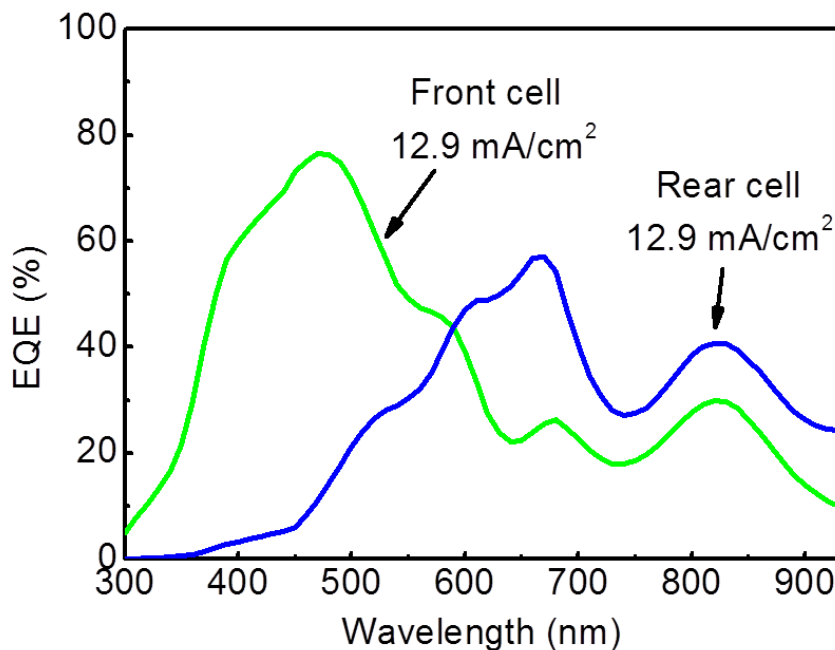
Figure 4-3 Simulated EQEs of a mono-bandgap PbS CQD tandem solar cell. The modelled tandem cell structure is ITO glass/ZnO/front absorbing layer (1.5eV, 140nm)/ Au/ ZnO/rear absorbing layer (1.5eV, 300nm)/ Au contact.

A single-junction CQD solar cell is usually limited by absorbing layer diffusion length. For a typical PbS CQDs absorbing layer, the diffusion length is ~250 nm and the efficiency usually maximise at thickness of 300 nm.[333] Going beyond this thickness would cause degradation of currents and FF[335] and so the overall cell performance. From this simulation, it is shown that

a mono-bandgap tandem structure could increase the total absorbing layer thickness beyond the diffusion length for single-junction cells. The total thickness of this simulated mono-bandgap PbS CQD tandem solar cell absorbing layers achieves 440 nm, which is beyond the thickness of 300 nm for single-junction PbS CQD solar cells. A mono-bandgap tandem solar cell could increase cell performance due to enhanced absorbance driven from much increased total absorbing layer thickness.

For now, the highest efficiency of CQD tandem solar cell is achieved by a mono-bandgap tandem cell structure. An efficiency of 8.9% has been reported for mono-bandgap PbS CQD solar cell by Ma's group. [77] This is still much lower than the efficiency of a single-junction PbS CQD solar cell of 12.5%.[2] Though mono-bandgap PbS CQD tandem solar cell has achieved a comparatively high efficiency for now, tandem cells with different bandgaps have much greater potential for a higher efficiency. The following section focuses on simulations for tandem cells made with subcells with different bandgaps.

4.4 EQEs for PbS CQD tandem cells with different bandgaps (Au interlayer)

4.4.1 Bandgaps' optimisation for subcells

For guiding experimental fabrication of PbS CQD tandem solar cells, the front cell and rear cell bandgaps were investigated by the modelling firstly. According to detailed balanced limit calculation, the optimal bandgap combination of a double-junction tandem cell is 1.6 eV and 1.0 eV.[261] However, by applying the thin-film semi-transparent layers assumption, the optimal bandgap combination changes to 1.5 eV and 1.2-1.1 eV for front and rear cells respectively.[261] In this research, quantum dots with 1.5 eV bandgaps for the front cell were immediately chosen and applied directly, while quantum dots with 1.37 eV, 1.22 eV and 1.14 eV bandgaps were compared and selected for the rear cell. Figure 4-4 shows the simulated EQEs for tandem cells with 1.37 eV (a), 1.22 eV (b) and 1.14 eV (c) quantum dots as rear cell absorbing materials respectively. From the simulated EQEs of tandem solar cells with different bandgaps, it is shown that in these tandem cells the front cell mainly absorbs light at 300-500 nm and 800-900 nm ranges, while the rear cell uses light in the 500-800 nm and >900 nm wavelength ranges. Front cell and rear cell absorbing ranges complement each other, forming a wider spectrum absorbing range.

Compared to a mono-bandgap tandem cell, not only the total absorbing layer thickness is higher, but also an extended absorbing range to fully utilise the solar spectrum can be obtained by tandem cells with different bandgaps. With narrowing rear cell bandgap, the rear cell absorbing range extends further toward longer wavelength side as shown in Figure 4-4(a,b,c).

With the same rear cell thickness of 300 nm, front cell thickness was adjusted to match currents from both subcells. The matched tandem cell current of 15.3 mA/cm^2 for 1.22 eV quantum dots in a rear cell is the maximum matched tandem cell current as shown in Figure 4-4(d). Table 4-1 lists the simulation parameters and results for tandem cells with different rear cell bandgaps. Based on the comparison between rear cells with different bandgaps, 1.22 eV quantum dots were chosen as rear cell absorbing material for making tandem cells together with the front cell with 1.5 eV quantum dots.

The current of tandem cell with 1.14 eV quantum dots as rear cell material shows a lower value is possibly due to the synthesised materials quality leading to a lower k for quantum dots sample with 1.14 eV than quantum dots with 1.22 eV, as shown in Figure 4-1. One thing worth a mention is the peak at 700 nm for the front cell in Figure 4-4(a,b). This is due to interference caused by Au interlayer. Simply by replacing Au with ITO, this peak would disappear, which can be shown by comparing Figure 4-4(a) and Figure 4-8 in the next section. The same explanation applies to the peak at 1000 nm in Figure 4-4 (c).

Table 4-1 Parameters and matched currents of PbS CQD tandem cells with different rear cell bandgaps. Front cell absorbing layers' thicknesses were tuned for current matching under a fixed rear cell thickness. The matched current of tandem cell with 1.22 eV rear cell could reach 15.3mA/cm^2.

Au thickness	Front cell bandgap	Rear cell bandgap	Rear cell thickness	Matched Current
2 nm	1.5 eV	1.5 eV	300 nm	12.9 mA/cm^2
2 nm	1.5 eV	1.37 eV	300 nm	13 mA/cm^2
2 nm	1.5 eV	1.22 eV	300 nm	15.3 mA/cm^2
2 nm	1.5 eV	1.14 eV	300 nm	11.6 mA/cm^2
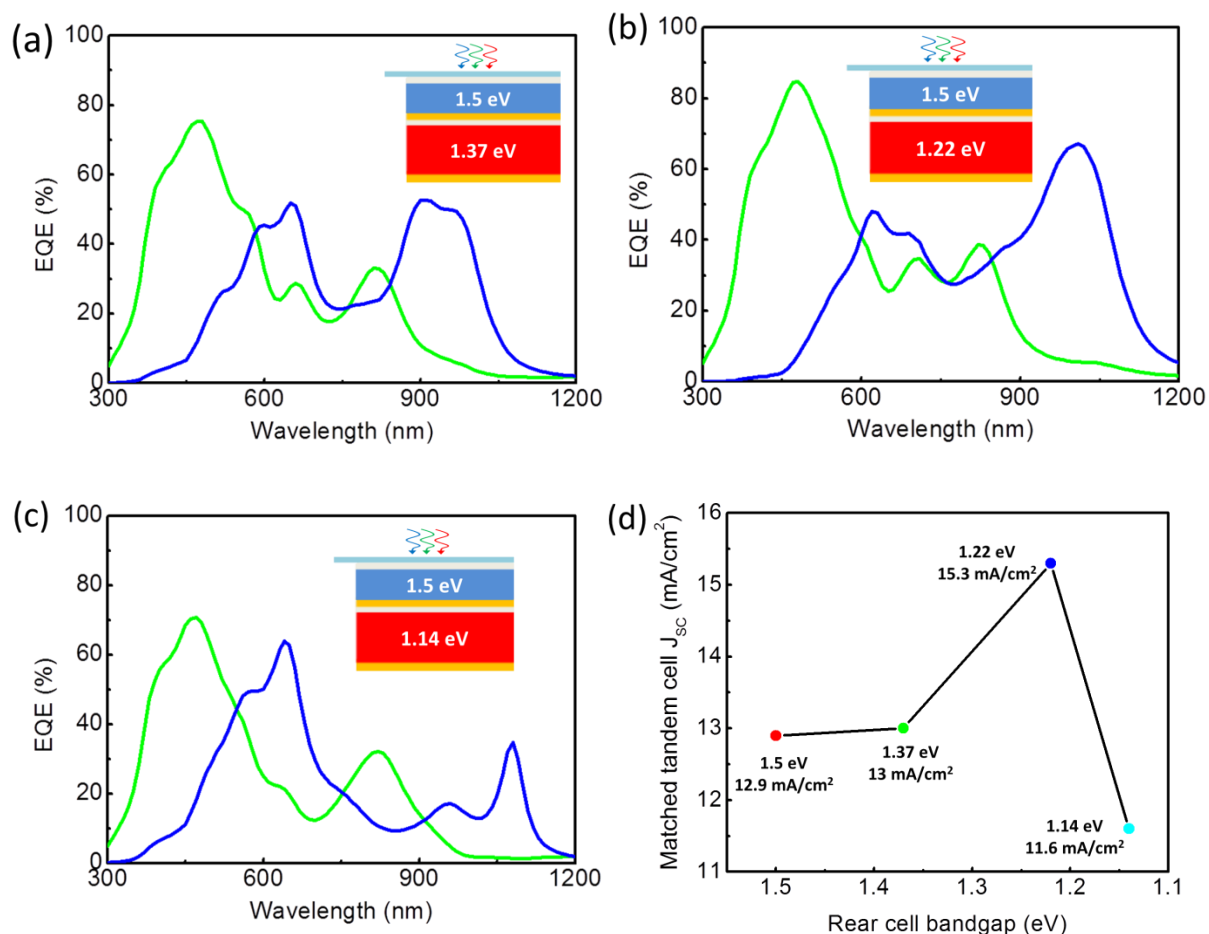
Figure 4-4 Simulated EQEs of PbS CQD tandem solar cells with 1.37 eV (a), 1.22 eV (b) and 1.14 eV (c) rear cells. (d) Comparing matched currents with different rear cell bandgaps (including 1.5 eV rear cell for a mono-bandgap tandem cell simulated in Figure 4-3). The matched current of 15.3 mA/cm² for the rear cell with 1.22 eV CQDs is the theoretical maximum value.

4.4.2 Investigating Au interlayers' thicknesses

After determining bandgaps of absorbing layers for the simulation, the influence of the interlayer is investigated as the interlayer is playing a critical role in a tandem structure in this section. An interlayer not only mechanically combines two sub cells together, but also recombines electrons and holes from both subcells. High performance interlayers need to have a high transparency because a low transparency interlayer reduces the rear cell current

density and a low light condition would cause reduced fill factor leading to a poor performance for a tandem solar cell.

An ultra-thin Au layer can perform as an interlayer for PbS CQD tandem solar cells.[77] The conductivity of Au is very high and the transparency of the Au layer can only be high when the Au layer thickness is confined within a few nanometres. An optical modelling for PbS CQD tandem solar cells with Au interlayers in different thicknesses has been performed. Figure 4-5 shows the simulated EQEs of PbS CQD tandem solar cells with 1 nm (a), 2 nm (b), 5 nm (c) and 10 nm (d) Au interlayers respectively. Table 4-2 lists the parameters of PbS CQD tandem cells in this modelling. Figure 4-5(e) shows the relationship between matched tandem cell current and Au interlayer thickness. As shown in Table 4-2 and Figure 4-5(e), when the thickness of Au layer increases, front cell thickness needs to be reduced for keeping a matched current with a fixed rear cell thickness. Generally, as the thickness of Au layer increases, the current of a current-matched tandem cell decreases. This is because a much thicker Au layer is with lower transparency which leads to fewer photons transmitted through leading to reduced overall tandem cell current. Thus, an ultra-low thickness is required for Au as an interlayer. When Au thickness is below 2 nm, the matched current of tandem cell is no longer affected by the variation of Au thickness. So this means that a 2 nm Au layer is thin enough for maintaining a high transparency for the tandem cell.

Table 4-2 Parameters of PbS CQD tandem cells with different Au thicknesses in the modelling. With a fixed rear cell thickness, front cell absorbing layer thickness need to be tuned down when Au interlayer thickness increases. The matched current of tandem cell with 2nm Au interlayer could reach 15.3 mA/cm^2.

Au thickness	Front cell bandgap	Front cell thickness	Rear cell bandgap	Rear cell thickness	Matched Current
1 nm	1.5 eV	190 nm	1.22 eV	300 nm	15.3 mA/cm^2
2 nm	1.5 eV	190 nm	1.22 eV	300 nm	15.3 mA/cm^2
5 nm	1.5 eV	177 nm	1.22 eV	300 nm	14.9 mA/cm^2
10 nm	1.5 eV	129 nm	1.22 eV	300 nm	13 mA/cm^2
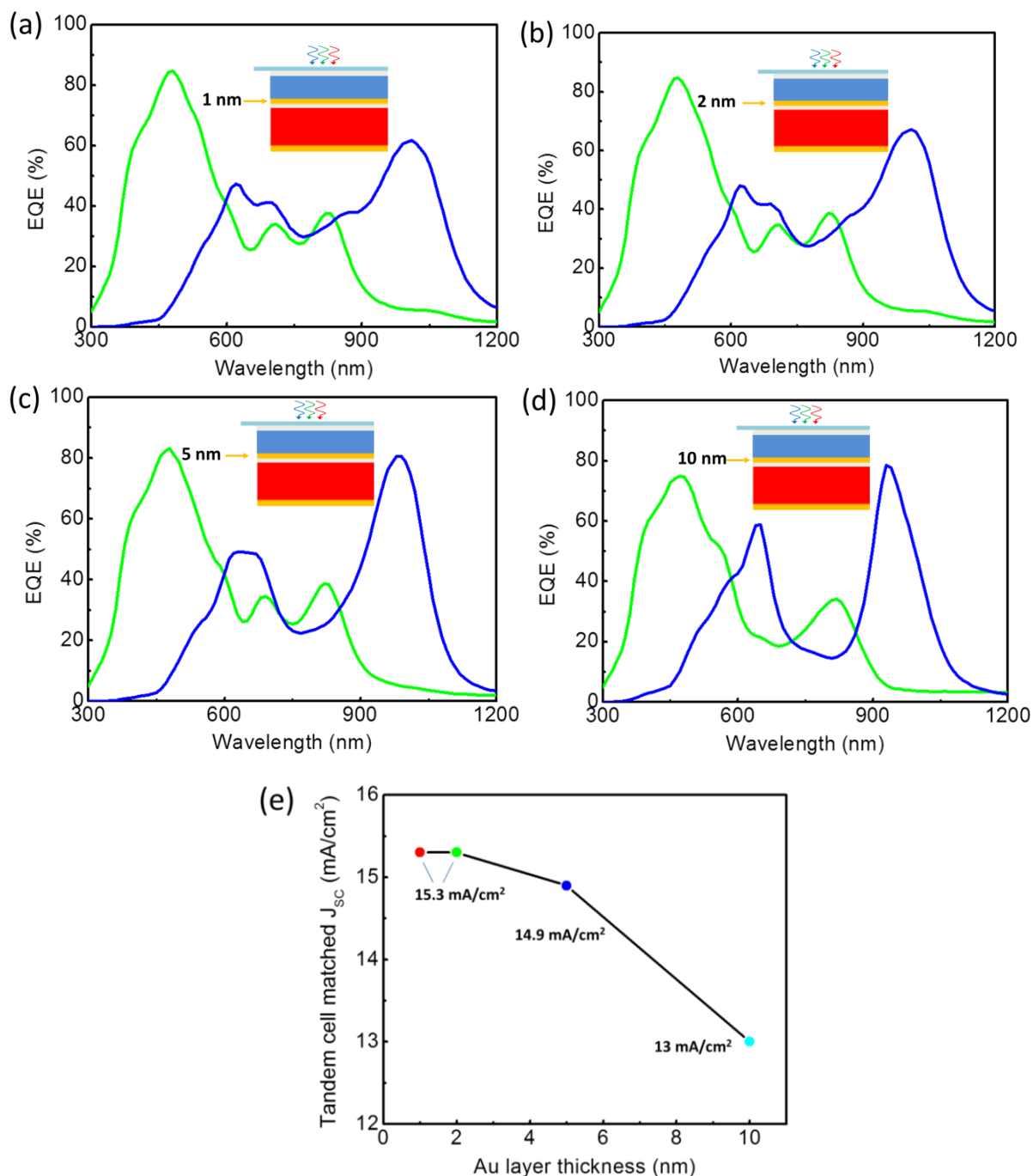
Figure 4-5 Simulated EQEs of PbS CQD tandem solar cell with Au interlayers with different thickness of 1 nm (a), 2 nm (b), 5 nm (c) and 10 nm (d). The rear cells are all with a bandgap of 1.22 eV and a thickness of 300 nm. The front cells are with 1.5 eV quantum dot absorbing layer, of which the thickness was adjusted for current matching. (e) Relationship between the matched tandem cell currents with different Au interlayer thicknesses. When Au interlayer thickness is less than 2 nm, the tandem cell current is almost not affected by Au layer thickness. When Au layer thickness is greater than 2 nm, increasing Au layer thickness would show decrease in the tandem cell's matched current.

4.4.3 Investigating subcells' absorbing layers' thicknesses

After studying the influence of interlayer thickness based on fixed rear cell absorbing layer thickness, the influence of absorbing layer thicknesses needs to be investigated too. Based on the same Au layer thickness of 2 nm, PbS CQD tandem cells with a series of rear cell thicknesses (with front cell thicknesses adjusted for current matching) are investigated in this section.

Simulated EQEs of PbS CQD tandem cells with different rear cell thicknesses are shown in Figure 4-6. Modelling parameters are listed in Table 4-3. For rear cell thicknesses of 100 nm, 200 nm and 300 nm, the matched currents are 11.3 mA/cm^2, 12.5 mA/cm^2 and 15.3 mA/cm^2, respectively. With increasing the rear cell thickness, front cell thickness need to be increased for tandem cell current matching, and the matched tandem cell current would be increased.
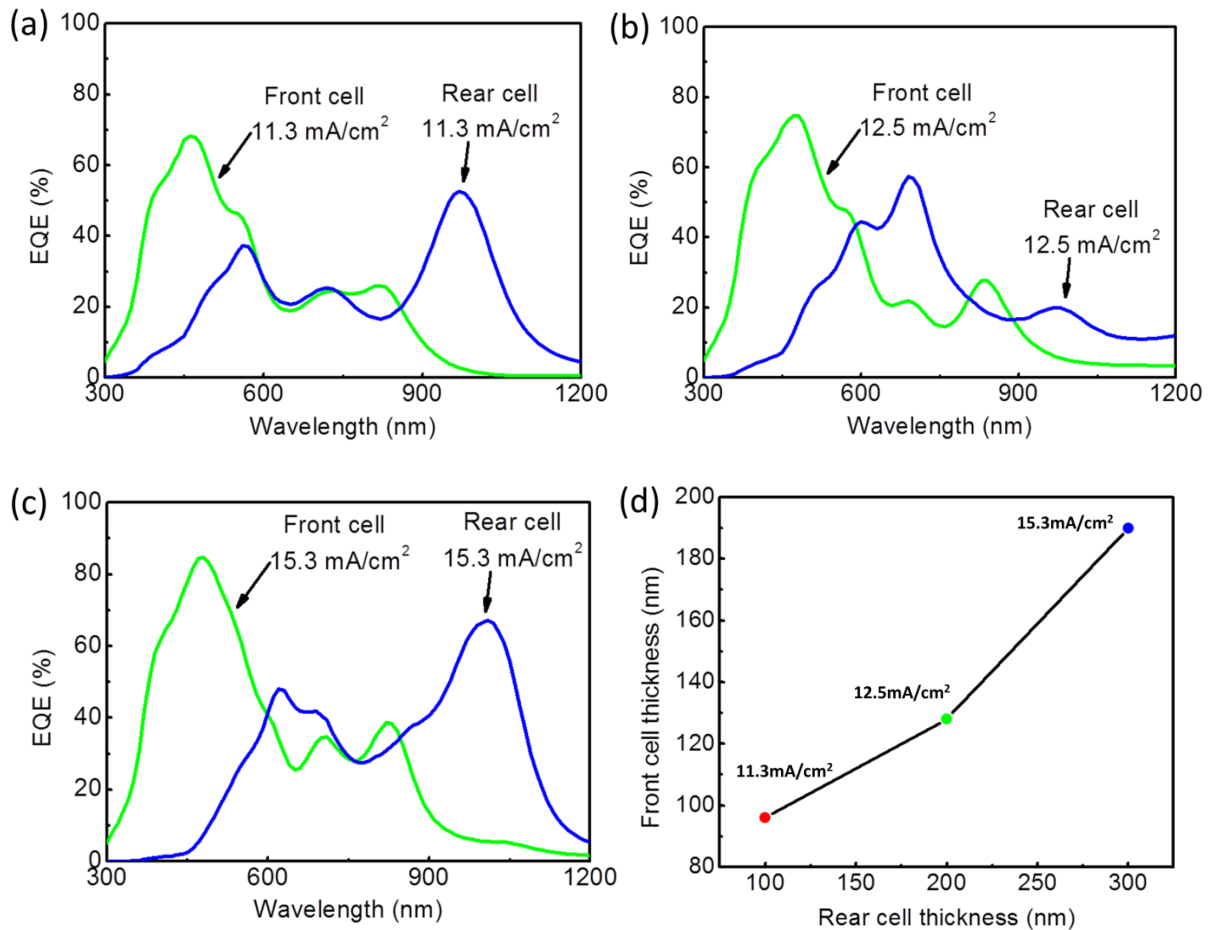
Figure 4-6 Simulated EQEs of PbS CQD tandem solar cell (Au interlayer) with varied subcells' absorbing layers' thicknesses. The matched currents of tandem cells with 100 nm (a), 200 nm (b) and 300 nm (c) rear cell absorbing layer are 11.3 mA/cm^2, 12.5 mA/cm^2, 15.3 mA/cm^2 respectively.

Table 4-3 Parameters of PbS CQD tandem cells with different rear cell absorbing layer thicknesses in the modelling. With a fixed interlayer thickness, front cell absorbing layer thickness need to be tuned up when rear cell thickness increases. The matched current of tandem cell with 300 nm rear cell absorbing layer thickness could reach 15.3 mA/cm^2.

Au thickness	Front cell bandgap	Front cell thickness	Rear cell bandgap	Rear cell thickness	Matched Current
2 nm	1.5 eV	96 nm	1.22 eV	100 nm	11.3 mA/cm^2
2 nm	1.5 eV	128 nm	1.22 eV	200 nm	12.5 mA/cm^2
2 nm	1.5 eV	190 nm	1.22 eV	300 nm	15.3 mA/cm^2

4.5 Optical modelling for PbS CQD tandem cells with ITO interlayer

Except for ultra-thin Au layer, ITO (Indium Tin Oxide) is investigated as interlayer in this section because of its high transparency and high conductivity. Though ITO has been widely used as contacts in thin film solar cells, the potential for ITO as an interlayer has been under-investigated. The influence of ITO interlayer thicknesses on PbS CQD tandem solar cell's matched current is investigated in this section. Based on tandem cells with fixed front cell and rear cell thicknesses, different ITO interlayer thicknesses of 6nm, 80nm and 200nm were simulated. Figure 4-7 shows the matched current densities of tandem cells with ITO interlayer in different thicknesses of 6 nm (a), 80 nm (b) and 200 nm(c). Simulated cell parameters are listed in Table 4-4. With different ITO layer thicknesses, the same matched current of 15.2mA/cm^2 was obtained for the tandem cells. The varied ITO thickness does not change tandem cell's matched current densities according to the simulated result. The reason for this can be attributed to that the transparency of ITO as interlayer is rarely affected by the thickness in this modelling.
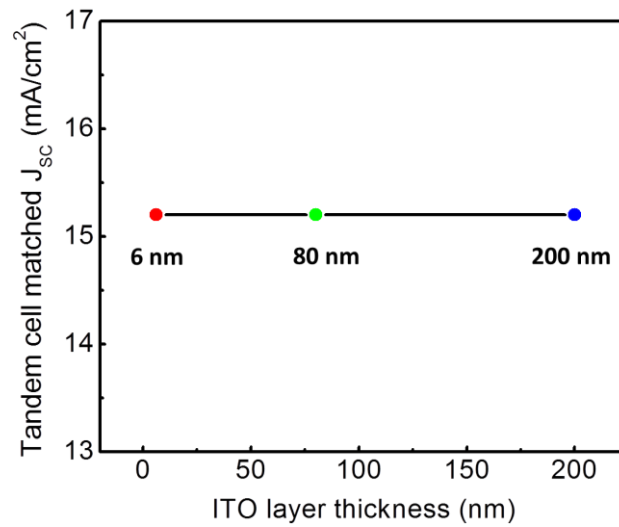
Figure 4-7 Simulated current densities of PbS CQD tandem solar cells with ITO interlayers with different thicknesses of 6 nm, 80 nm and 200 nm. The same matched current of 15.2 mA/cm^2 was obtained by different ITO interlayer's thicknesses.

Table 4-4 Parameters of PbS CQD tandem cells with ITO interlayers in different thicknesses of 6 nm, 80 nm and 200 nm. The matched currents are all the same with different ITO interlayer thicknesses.

ITO thickness	Front cell bandgap	Front cell thickness	Rear cell bandgap	Rear cell thickness	Matched Current
6 nm	1.5 eV	190 nm	1.22 eV	300 nm	15.2 mA/cm^2
80 nm	1.5 eV	190 nm	1.22 eV	300 nm	15.2 mA/cm^2
200 nm	1.5 eV	190 nm	1.22 eV	300 nm	15.2 mA/cm^2

Then, the influence of subcells' absorbing layers' thicknesses on the PbS CQD tandem solar cell (with ITO interlayer)'s performance was also simulated. Figure 4-8(a,b,c) shows EQEs of PbS CQD tandem solar cells with ITO interlayers. For the tandem cells with ITO interlayers the front cell mainly absorbs light at 300-500 nm and 800-900 nm wavelength ranges, while the rear cell uses 500-800 nm and >900 nm wavelength ranges. Front cell and rear cell absorbing ranges also compensate with each other. Figure 4-8(e) shows the relationship between matched currents of tandem cells and rear cell absorbing layer thicknesses. For rear cell thicknesses of 100 nm, 200 nm and 300 nm, the matched currents of tandem cells could reach 11.3 mA/cm^2, 12.9 mA/cm^2 and 15.2 mA/cm^2 respectively. Table 4-5 lists parameters of simulated tandem cells with varied subcells' absorbing layers' thicknesses.
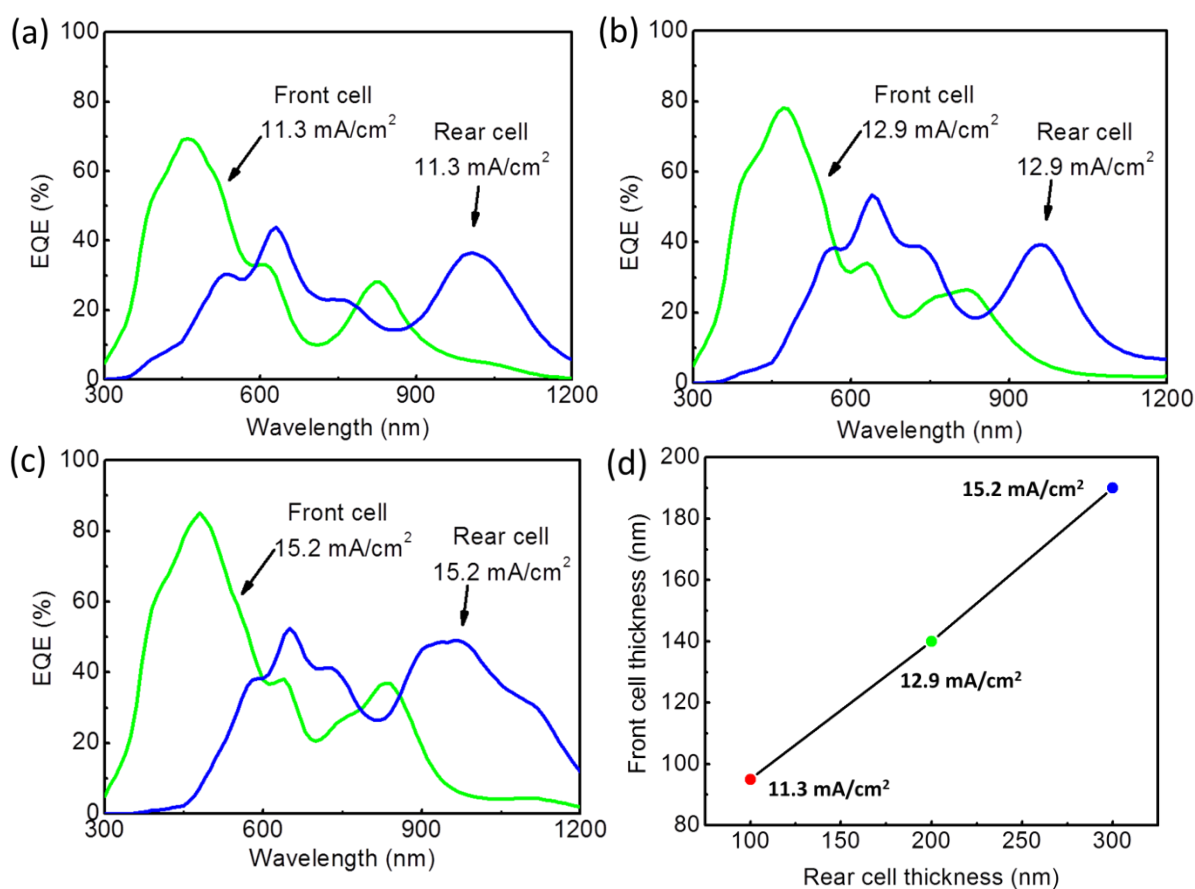
Figure 4-8 Simulated EQEs of PbS CQD tandem solar cell (ITO interlayer) with varied subcells' absorbing layers' thicknesses. The matched currents of tandem cells with 100 nm (a), 200 nm (b) and 300 nm (c) rear cell absorbing layer are 11.3 mA/cm^2, 12.9 mA/cm^2, 15.2 mA/cm^2 respectively.

Table 4-5 Parameters of simulated PbS CQD tandem cells with varied absorbing layer thicknesses. Front cell absorbing layer thickness need to be tuned down when rear cell thickness decreases. The matched current of tandem cell with 300 nm rear cell absorbing layer thickness could reach 15.2mA/cm^2.

ITO thickness	Front cell bandgap	Front cell thickness	Rear cell bandgap	Rear cell thickness	Matched Current
80 nm	1.5 eV	95 nm	1.22 eV	100 nm	11.3 mA/cm^2
80 nm	1.5 eV	140 nm	1.22 eV	200 nm	12.9 mA/cm^2
80 nm	1.5 eV	190 nm	1.22 eV	300 nm	15.2 mA/cm^2

4.6 J-V curve modelling

Besides optical modelling which analyses subcells' currents and EQEs for PbS CQD tandem solar cells, a J-V curve modelling could further simulate the power conversion efficiency of tandem cells. J-V curves of tandem cells and corresponding single-junction cells can be simulated based on a diode modelling combined with the result of above mentioned optical modelling. In this J-V curve modelling, there are three basic assumptions: (1) the cell absorbance and current densities follow the described optical modelling; (2) only Shockley-Read-Hall recombination happens in the relaxation process. In this modelling, carrier lifetime is taken into consideration and shows significant impact on cell voltage and efficiency. Figure 4-9 and Figure 4-10 show simulated single-junction front cell and rear cell respectively with different carriers' lifetimes. For both single-junction subcells, with carrier lifetime increasing, voltages of simulated cells would increase.

By assuming quantum dot lifetime to be 1 ms which is a typical high quality quantum dot lifetime, [336-339] voltages of single-junction front cell (with large bandgap quantum dots) and single-junction rear cell (with narrow bandgap quantum dots) were simulated to be ~0.7 V and ~0.6 V respectively. The tandem cell PCE could reach 15.5% under this condition with a combined voltage of 1.27eV, of which the simulated cells' parameters are listed in Table 4-6. Simulated J-V curves of both the tandem cell and the corresponding single-junction cells with $\tau = 1$ms are shown in Figure 4-11.

Table 4-6 Simulated performance of both the PbS CQD tandem cell and the corresponding single-junction cells with $\tau = 1$ms. The simulated PbS CQD tandem cell efficiency is 15.5%.

	J_{SC} (mA/cm^2)	V_{OC} (V)	FF (%)	PCE (%)
Front cell	14.8	0.7	84.5	8.7
Single rear cell	26.7	0.59	83	13
Tandem cell	14.8	1.27	82.5	15.5
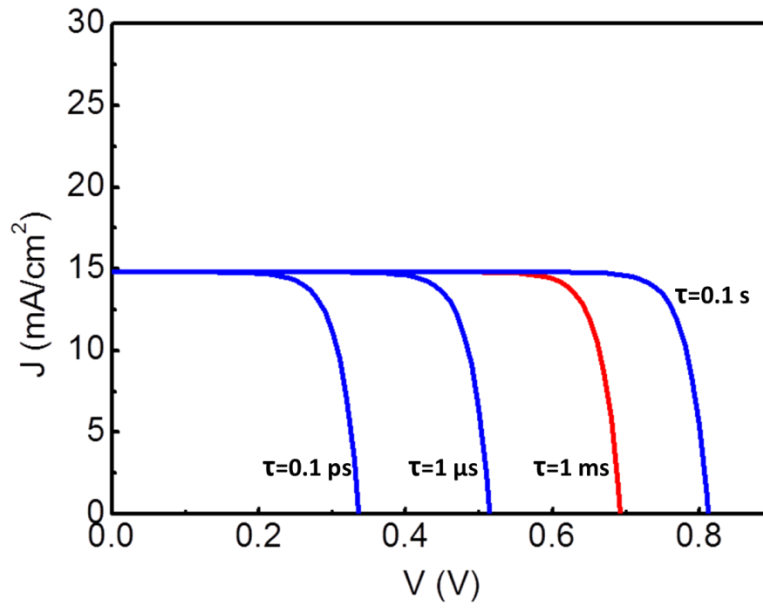
Figure 4-9 J-V curves of single-junction cells with large bandgap CQDs (for front subcell) with different lifetimes. For a typical quantum dot which has a lifetime of 1 ms, the V_{OC} is simulated to be 0.7 V.
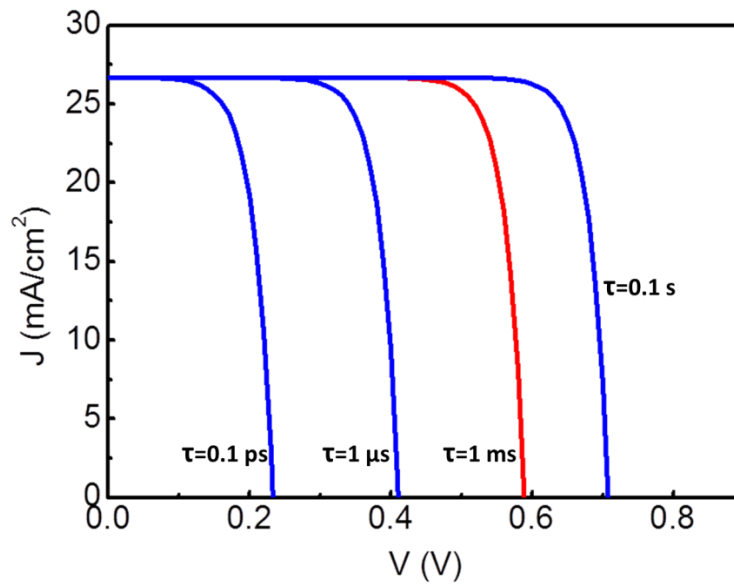
Figure 4-10 J-V curves of single-junction cells with narrow bandgap CQDs (for rear subcell) with different lifetimes. For a typical quantum dot which has a lifetime of 1 ms, the V_{OC} is simulated to be 0.6 V.
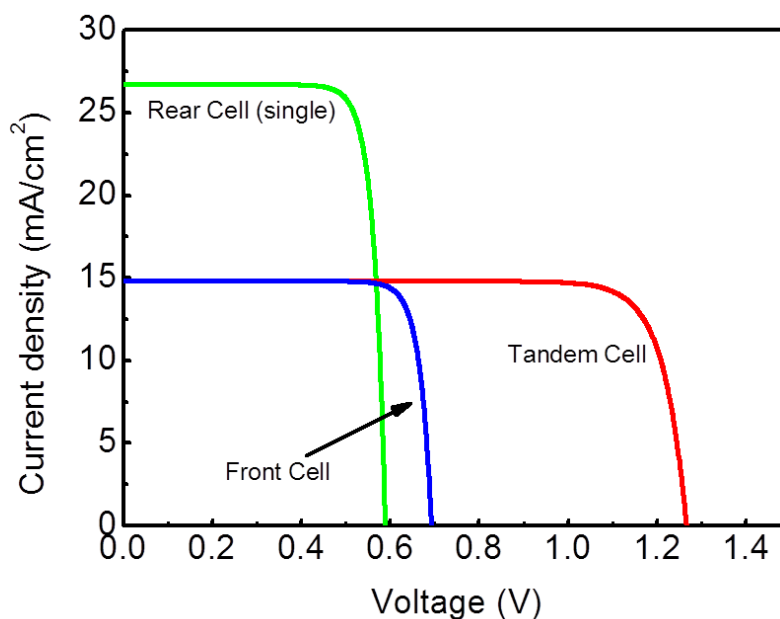
Figure 4-11 Simulated J-V curves of both the PbS CQD tandem solar cell and the corresponding single-junction cells with τ = 1 ms.

4.7 Conclusion

In this chapter, for guiding experimental works in the next chapter, optical modelling has been performed for simulating PbS CQD tandem solar cells' performance. Both mono-bandgap tandem cells and tandem cells with subcells with different bandgaps have been simulated. Tandem cells' subcells bandgaps, interlayer thicknesses and subcells' absorbing layer thicknesses were all studied and optimised in the modelling. Under optimised conditions, a matched current of 15.3 mA/cm^2 could be achieved by a PbS CQD tandem solar cell. Moreover, different interlayers of ultra-thin Au and ITO are both investigated in this optical modelling. The optical modelling has shown that increasing Au layers thickness decreases tandem cell current dramatically while tuning ITO layer thickness has negligible influence on tandem cell current. The modelling shows that 2 nm Au layer is sufficient to inter-connect subcells to achieve good current.

Besides, J-V curve simulation shows predicted performance of quantum dot tandem solar cells and corresponding single-junction quantum dot solar cells. According to the J-V curve simulation, quantum dot tandem solar cell could reach an efficiency of ~15.5% with the lifetime τ = 1 ms.

Chapter 5. Fabrication of PbS Quantum Dot Tandem Solar Cells

In this chapter, based on the improved electron transport layer and the established optical modelling guiding the design of tandem solar cell structure, monolithic PbS CQD tandem solar cells have been successfully fabricated. PbS CQD tandem solar cells with Au interlayer and ITO interlayer are both studied. A graded band alignment strategy has been introduced for improving PbS CQD tandem solar cell in this chapter. The champion PbS CQD tandem solar cell reached an efficiency of around 7%.

5.1 Introduction

For building a working tandem solar cell, good-quality single-junction solar cells are required and a proper tandem cell structure needs to be designed by an efficient modelling. In chapter 3, single-junction PbS CQD solar cell work has been investigated and an improved electron transport layer was waiting to be incorporated into a tandem framework. In chapter 4, modelling works has been established for showing a proper tandem configuration including proper bandgap selection and absorbing layer thicknesses adjustment. These preparation works have paved the way towards experimentally fabricating an efficient PbS CQD tandem solar cell. In this chapter, based on those preparation works, monolithic PbS CQD tandem solar cells were fabricated and characterised.

For the research of CQD tandem cells, there are only a few works have been reported so far.[75-77] In 2011, Wang et al[75] reported the first PbS CQD tandem cell with an efficiency of >4%, while Choi et al[76] also reported a PbS CQD tandem solar cell structure in the same year. In 2016, Ma et al[77] re-studied Choi's structure with two of the junctions made of the same bandgap material. In 2017, Luther et al reported a hybrid CQD tandem solar cell combining CdTe quantum dots and PbS quantum dots as front and rear cell absorbing layers

respectively. In 2018, Yu Bi et al[263] used deposited graphene as interlayer for a PbS CQD tandem solar cell.

Referring to those pioneer works, in this chapter, monolithic PbS CQD tandem solar cells were successfully fabricated. Both tandem cells with ultra-thin Au interlayer and ITO interlayer were constructed and investigated. Furthermore, a graded bandgap alignment strategy for the first time was employed to further improve PbS CQD tandem solar cell efficiency. The champion cell in this research reached an efficiency of around 7%.

5.2 Method

5.2.1 Preparation of ZnO nanoparticles

ZnO nanoparticles were synthesized following a previously reported method.[280, 306, 309, 310] Details refer to Method in section 3.2.

5.2.2 Preparation of PbS quantum dots

PbS quantum dots for front and rear cells were fabricated referring to previously reported methods, with modifications.[152, 340-342] For the front cell quantum dots with a bandgap of 1.5 eV, a mixture of Bis(trimethylsilyl)sulfide (TMS, 0.12 g) and 1-octadecene (ODE, 4 g) was prepared firstly. Then, a mixture of PbO (0.45 g), oleic acid (OA, 1.5 g) and ODE (15 g) was heated to 100°C for 3 hours under vacuum. The mixture was then cooled down to 75°C followed by injection of the TMS/ODE mixture solution. The resulting colloidal solution was removed from the heating mantel and allowed to cool down naturally. The as-synthesized PbS quantum dots were purified by centrifugation using acetone as an anti-solvent and hexane as a solvent for three times. The final quantum dots were dispersed in hexane at a concentration of 20 mg/ml.

For synthesizing rear cell quantum dot, a similar process was used with different amount of oleic acid and reaction temperature to produce different sizes. For the absorbing quantum dots with a bandgap of 1.22 eV, the amount of oleic acid was doubled and the injection performed at 95°C. For quantum dots with a bandgap of 1.14 eV, the amount of oleic acid was quadrupled and injection at 95°C was performed. All chemicals were purchased from Sigma-Aldrich and used as received.

5.2.3 Fabrication of PbS single-junction and tandem solar cells

Single-junction cells and front cell fabrications refer to Method in chapter 3.2.

To fabricate tandem cell's interlayer, an Au layer with a thickness of 2 nm was evaporated onto the front cell using an evaporator. The evaporation was conducted at a rate of 0.1 Å/s under 1×10^{-6} mTorr. A thickness meter could monitor the real-time thickness of the deposited Au film. ITO interlayer was sputtered on the PbS CQDs layer with 30 W RF power with Ar at 1.5 mTorr for 120 min using an AJA International sputtering system. A ZnO-NP layer with or without surface doping was then spin-coated on top of the Au interlayer at 2500 rpm for 30s. Then, the remaining rear cell was fabricated following the single-junction cell process with narrow bandgap quantum dots with or without graded band alignment.

For the graded rear cell structure fabrication, just replace the quantum dot in the first layer in PbS-I (1.22eV) layers with 1.13eV quantum dots and that in the last layer with 1.5eV quantum dots. As well, quantum dots for PbS-EDT layers were replaced by 1.5eV quantum dots for forming the graded cell structure. The total numbers of deposited layers for graded and non-graded cells were kept the same in both PbS-I and PbS-EDT absorbing layers.

5.2.4 Measurement and characterisation

Characterization method refer to Method section 3.2 except for the differences illustrated following.

Cross-sectional scanning electron microscope (SEM) samples were prepared by cut-and-break method applying a glass cutter. SEM images were obtained using an FEI Nova Nano 450 SEM.

The current density–voltage (J-V) measurements were performed using a voltage scanning range from -0.25 V to 1.75 V. The cell area was defined by an aperture of 0.03 cm^2.

The EQE of the rear cell was measured by placing a single-junction front cell as a filter in front of a single-junction rear cell. This measurement method was proven to be acceptable by reported researches.[77, 343, 344]

All characterizations were performed at room temperature in ambient conditions except the SEM that were carried out in a vacuum chamber.

5.3 PbS CQD tandem solar cell with Au interlayer

Though the current highest performance of PbS CQD tandem solar cells is achieved by a mono-bandgap structure, tandem solar cells with different bandgaps have a greater potential for a higher efficiency.[77] For making a PbS CQD tandem solar cell with different bandgaps, quantum dots with different bandgaps should be obtained by tuning the synthesis conditions. By tuning precursor ratio and injection temperature, a series of quantum dots with different bandgaps were synthesised. Absorbance of quantum dots with different bandgaps is shown in Figure 5-1.
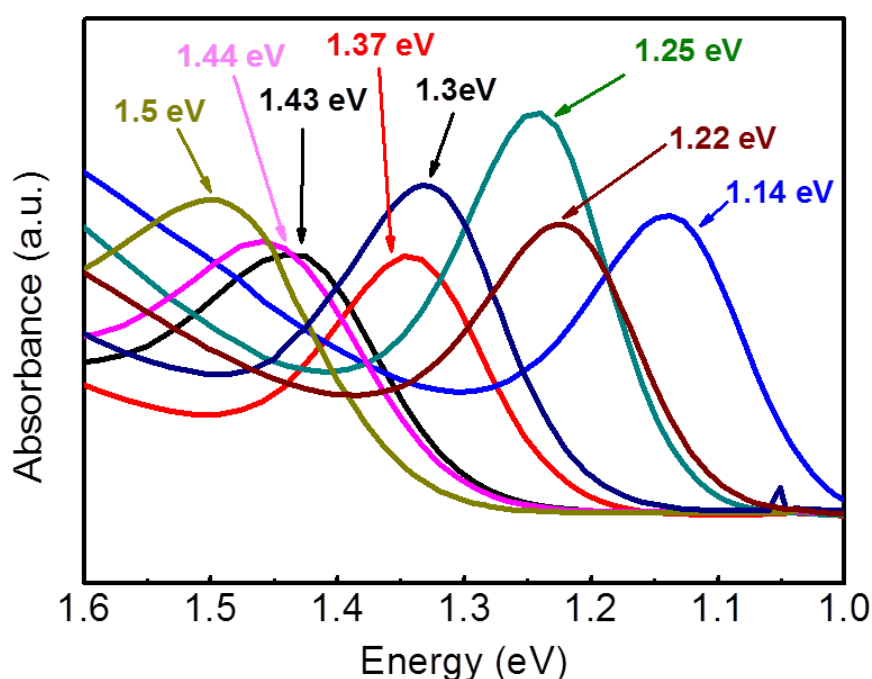
Figure 5-1 Absorbance of synthesised quantum dots with different bandgaps. By tuning synthesis conditions, quantum dots with bandgaps ranging from 1.1 eV to 1.5 eV can be obtained.

For choosing quantum dots with proper bandgaps for the rear cell, single-junction cells with quantum dots with 1.22 eV and 1.14 eV bandgaps were compared experimentally. Fabricated single-junction CQD solar cell with a bandgap of 1.22 eV achieved a voltage of 560 mV while the cell with a bandgap of 1.14 eV only had a 430 mV voltage which is shown in Figure 5-2. Hence, there would be a 130 mV voltage increase by using 1.22 eV quantum dots in the rear cell absorbing layer. At the same time the currents are almost identical for cells with 1.14 eV and 1.22 eV. The results of this comparison are also consistent with previous

reported researches.[328, 345] Combining the bandgap values suggested by NREL's simulation [261] and the simulated results in section 4.4.1 in chapter 4, hence, 1.22 eV quantum dots were chosen as the rear cell absorbing material together with 1.5 eV quantum dots as the front cell absorbing material.
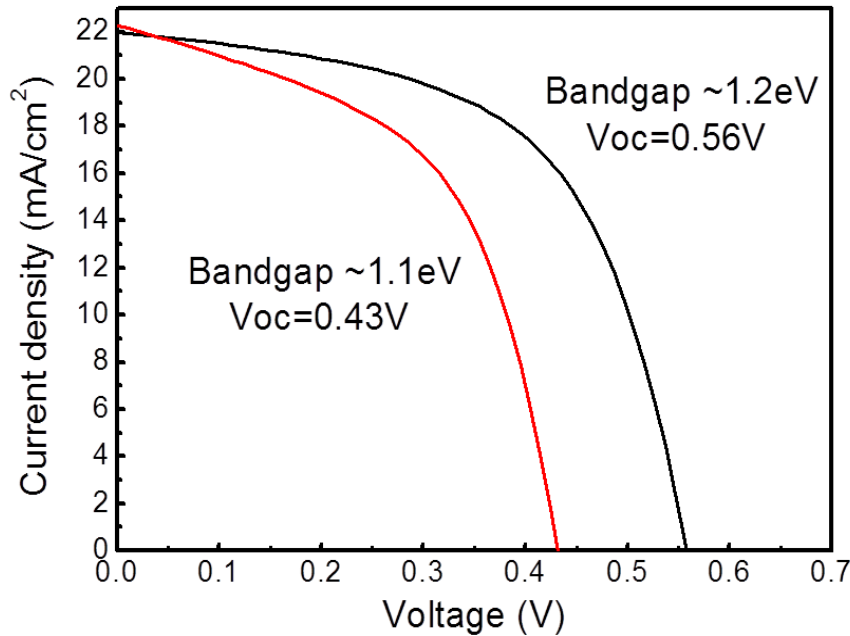
Figure 5-2 J-V curves of experimental single-junction PbS CQD solar cells with 1.22 eV and 1.14 eV quantum dots. The voltage of single-junction PbS CQD solar cell with 1.22 eV quantum dots is 560 mV while that with 1.14 eV quantum dots only has a voltage of 430 mV.

PbS CQD tandem solar cells with Au interlayer were fabricated based on a 1.5 eV front cell and a 1.22 eV rear cell. Referring to the simulated results in section 4.4.3 for tandem cell with 1.5 eV front cell and 1.22 eV rear cell, the thicknesses of front cell and rear cell were adjusted to be 190nm and 300nm respectively in the tandem cell fabrication experiments. The interlayer of 2 nm ultra-thin Au was utilised as suggested by the simulated results in section 4.4.2. A cross-sectional SEM image of a fabricated PbS CQD tandem solar cell is shown in Figure 5-3.

This tandem cell reached a PCE of 4.5% as shown in Figure 5-4 and listed in Table 5-1. V_{OC} and J_{SC} of this tandem cell are 1.1 V and 7.7 mA/cm^2 respectively. EQEs of subcells are shown in Figure 5-5. Integrated currents from front cell and rear cell EQEs are 12.2 A/cm^2 and 6.9 mA/cm^2 respectively. The front cell mainly responds to the wavelength of 300-600

nm while the rear cell mainly responds to the wavelength range of 600-900 nm. Though the rear cell EQE is low in the long wavelength range, the subcells' EQEs are still compensating with each other.
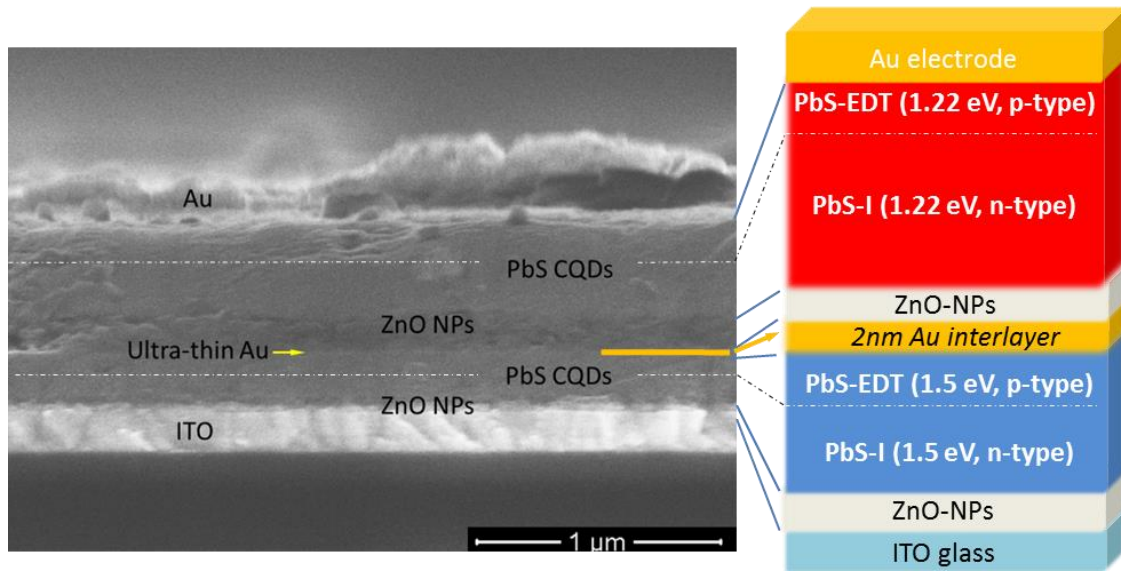
Figure 5-3 A cross-sectional SEM image of PbS CQD tandem solar cell. The cell structure is ITO glass/ZnO-NPs/PbS CQDs(1.5eV, 190nm)/Au (2 nm)/ZnO-NPs/CQDs(1.2eV, 300nm)/Au.
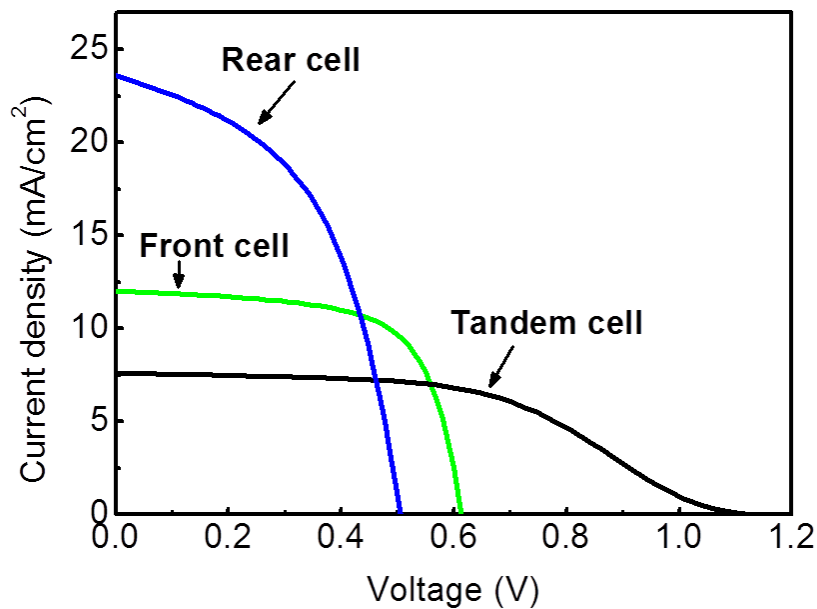
Figure 5-4 J-V curves of PbS CQD tandem solar cell with Au interlayer and corresponding single-junction cells. The tandem cell reached an efficiency of 4.5% with a combined V_{OC} of 1.1 V.

	J_{SC} (mA/cm^2)	V_{OC} (V)	FF (%)	PCE (%)
Front cell	12.0	0.61	66	4.8
Rear cell (Single)	23.6	0.51	50	6.0
Tandem cell	7.7	1.10	53	4.5
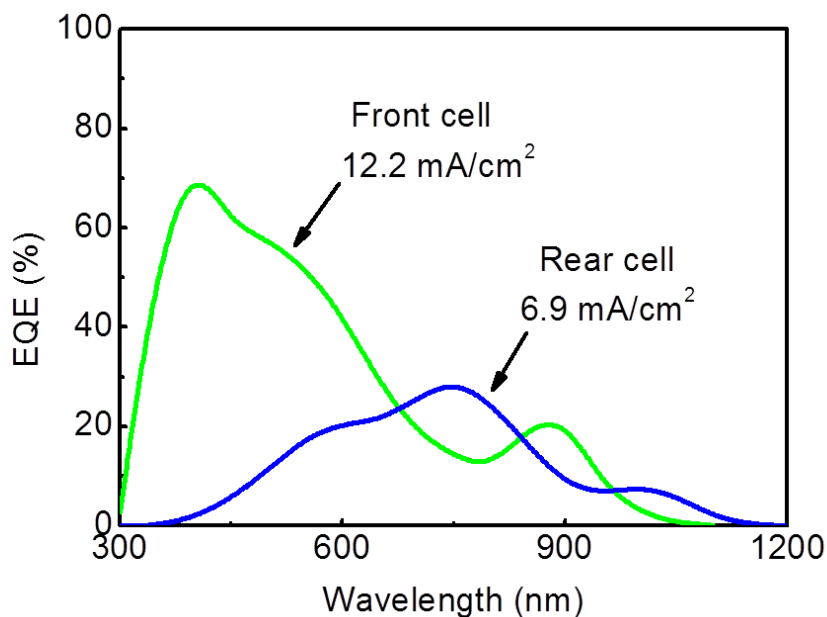
Figure 5-5 EQEs of subcells of PbS CQD tandem solar cell with Au interlayer. Front cell mainly responds to the wavelength of 300-600 nm while the rear cell mainly responds to the wavelength range of 600-900 nm.

Another reason for the low current for this tandem cell is a poor carriers' extraction from the rear cell. When low bandgap quantum dots are applied in the rear cell, where the low bandgap is mainly due to a down-shifted conduction band,[328] the build-in electrical field for extracting electrons near the n-type side tend to be weakened. So the rear cell's current density can be reduced by this and hence reducing the overall tandem cell's current. This poor carriers' extraction problem is to be tackled by a graded band alignment strategy in the following section 5.5 in this chapter.

5.4 Fabricating PbS CQD tandem solar cell with ITO interlayer

ITO is recognised as a transparent material which has been applied as interlayer in organic and perovskite tandem solar cells. Wang et al[75] utilised ITO in PbS CQD tandem solar cell, but a complicated interlayer was associated. This research applied a simplified monolayer ITO in a PbS CQD tandem solar cell as the interlayer. An investigation on the optical properties of ITO was conducted before making tandem cells. Figure 5-6 shows the transmittance of ITO in different thicknesses. 80 nm ITO was chosen as interlayer because ITO with this thickness exhibited high transmittance in the wavelength range between 500 nm and 800 nm while maintain the high transmittance between 350 nm and 450 nm.
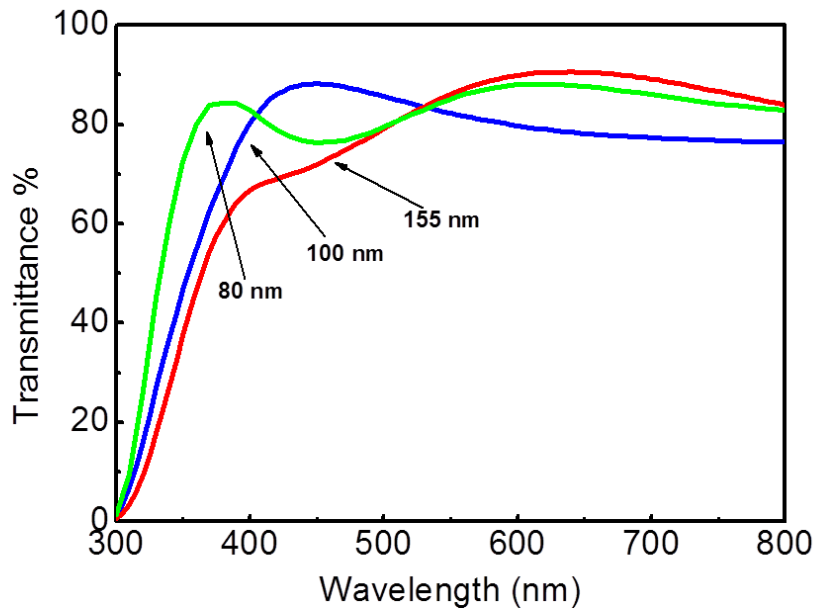
Figure 5-6 Transmittance of ITO with different thicknesses. ITO with a thickness of 80 nm exhibited high transmittance in the wavelength range between 500 nm and 800 nm while maintain the high transmittance between 350 nm and 450 nm.

Referring to the suggested subcell absorbing layer thicknesses by the optical modelling in section 4.5 in chapter 4, the PbS CQD tandem solar cell with an ITO interlayer was fabricated. An SEM cross-sectional image of the tandem cell is shown in Figure 5-7. The fabricated tandem cell is in a structure of ITO glass / ZnO-NP (80 nm) / small size PbS quantum dots (1.5 eV, 190 nm) / ITO (80 nm) / ZnO-NP (80 nm) / large size PbS quantum dots (1.22 eV, 300 nm) / Au (100 nm).

J-V curve of PbS CQD tandem solar cell with ITO interlayers is shown in Figure 5-8 and parameters are listed in Table 5-2. This tandem cell reached an efficiency of 4.9% and a combined V_{OC} of 1.1 V, which indicates a successful combination of subcells. The J_{SC} of the

tandem cell reached 8.1 mA/cm^2. The higher current density and FF for the tandem cell with ITO interlayer than that with Au interlayer is possibly because of the better transmittance of ITO as an interlayer.
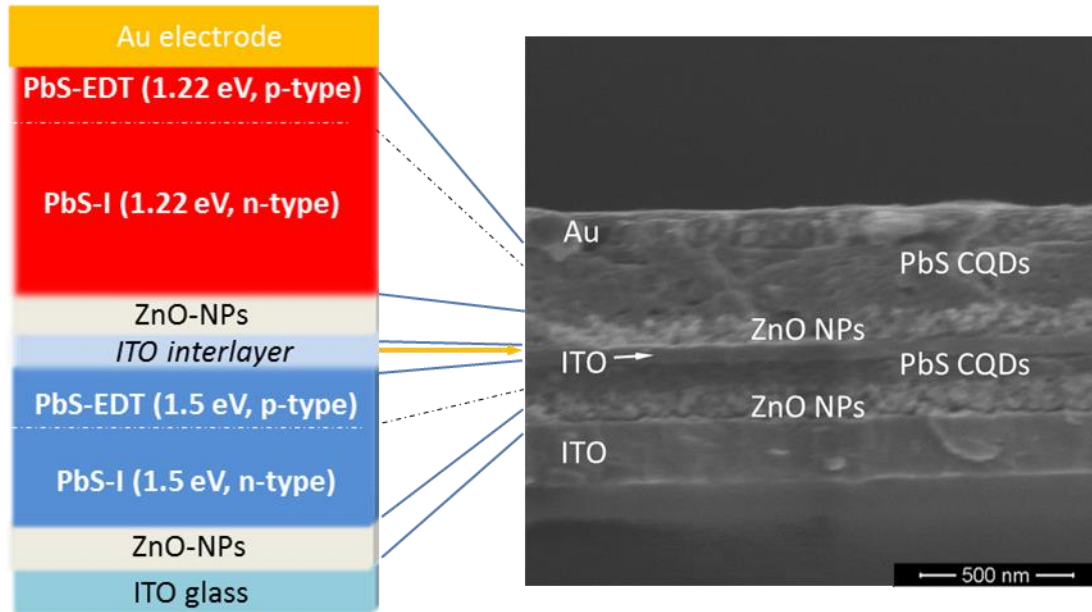
Figure 5-7 SEM cross-sectional image of PbS CQD tandem solar cell with ITO interlayer. The fabricated tandem is in a structure of ITO glass / ZnO-NP (80 nm) / small size PbS quantum dots (1.5 eV, 190 nm) / ITO (80 nm) / ZnO-NP (80 nm) / large size PbS quantum dots (1.22 eV, 300 nm) / Au (100 nm).

EQEs of subcells of PbS CQD tandem solar cell with ITO interlayer are shown in Figure 5-9. Integrated currents from front cell and rear cell are 12.2 mA/cm^2 and 7.3 mA/cm^2 respectively. Front cell mainly responds to the wavelength range of 300-600 nm while the rear cell mainly responds in the wavelength range of 600-800 nm and 900-1200 nm. The exciton peak of the front cell EQE at around 900 nm compensates the valley of the rear cell EQE at 800-950 nm.

One thing needs to be discussed is that the integrated J_{SC} from EQE of the rear cell is systemically lower than that of the tandem cell. One of the reasons is the measurement method itself. The rear cell EQE was measured with a top filter, which has a different light tracing configuration with the monolithic tandem structure. In a monolithic structure, decoupling between front and rear cell could enhance light utilisation.[346] But with the method with a filter, additional reflection can be introduced by the air gap between front filter and the rear single-junction cell and the extra glass of the single-junction rear cell. So the integrated

J_{SC} from measured rear cell EQE is lower than that from a monolithic structure. These situations were simulated and compared in monolithic and "four terminal" profiles (Figure 5-10), which is consistent with experiment results.
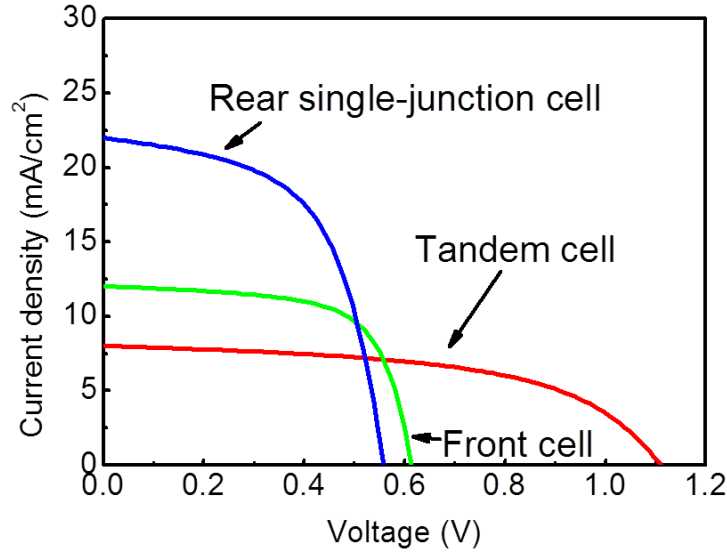
Figure 5-8 J-V curves of PbS CQD tandem solar cell with ITO interlayer and corresponding single-junction cells. The tandem cell reaches an efficiency of 4.9% with a combined V_{OC} of 1.1 V.
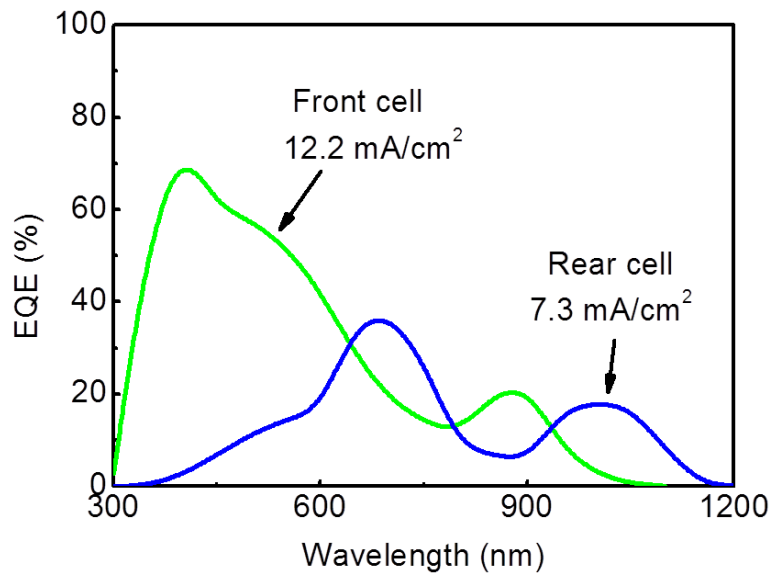
Figure 5-9 EQEs of subcells of PbS CQD tandem solar cell with different bandgaps. Front cell mainly responds to the wavelength of 300-600 nm while the rear cell mainly responds to the wavelength range of 600-800 nm and 900-1200 nm.
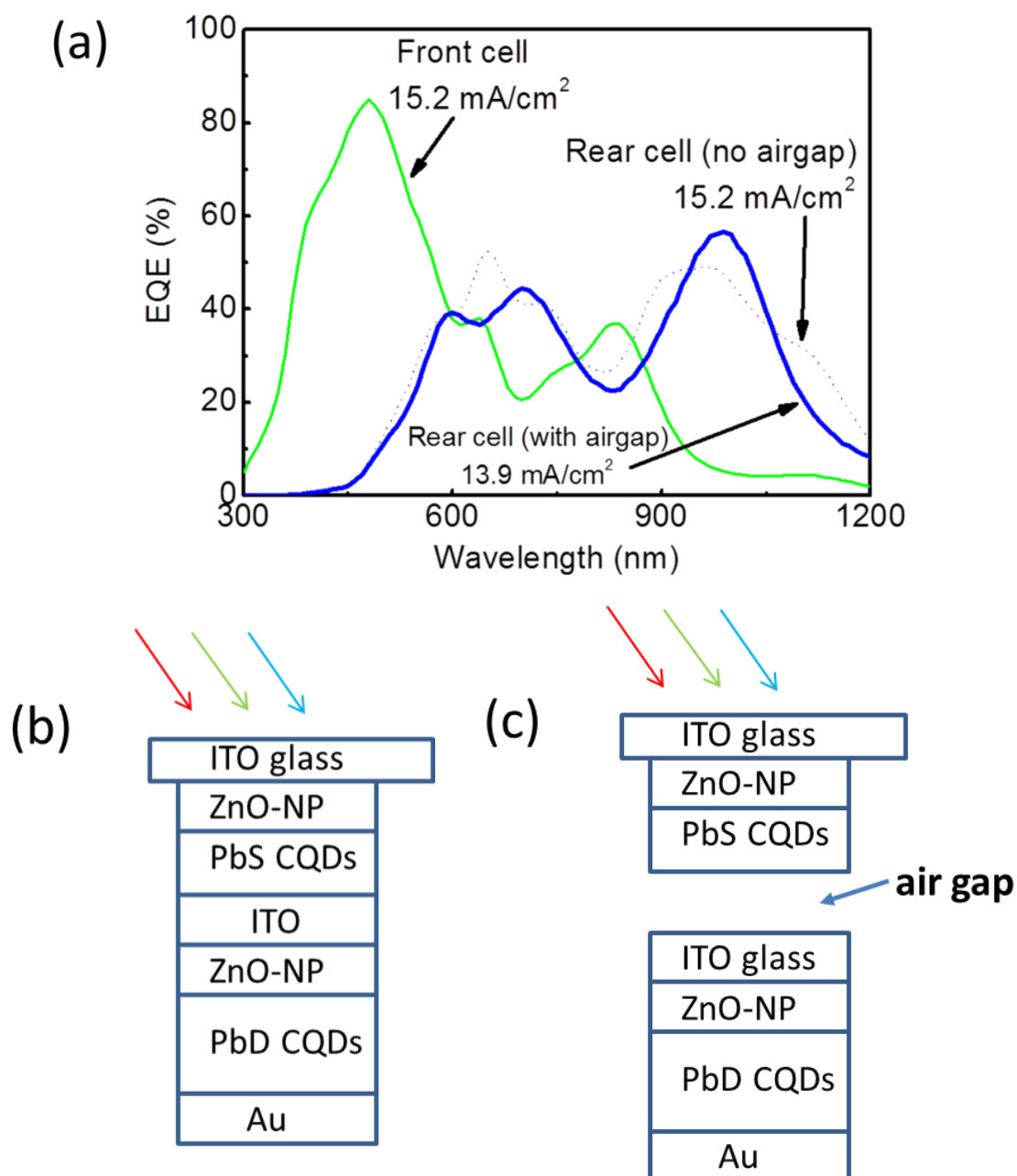
Figure 5-10 (a) Simulated EQEs of rear cells in monolithic tandem and in a "four terminal" profile (rear cell with filter). (b) Monolithic tandem cell structure. (c) "four terminal" cell structure (using a filter) with air-gap in between subcells. In a "four terminal" profile, the inserted airgap causes light scattering and additional interfaces, so that there is light loss and current drop in the rear cell. In contrast, in a monolithic tandem cell, there is no such a loss, so the current is expected to be higher. The simulated integrated J_{SC} from EQE obtained by using a filter (blue solid line) is only 13.9 mA/cm² while that obtained from a monolithic tandem structure (dash line) is 15.2 mA/cm².

	J_{SC} (mA/cm^2)	V_{OC} (V)	FF (%)	PCE (%)
Front cell	12.0	0.61	66	4.8
Rear cell (Single)	21.9	0.56	57	7.0
Tandem cell	8.1	1.11	54	4.9

5.5 Further improving PbS CQD tandem solar cell by graded band alignment

5.6.1 Improving rear cell performance by using graded band alignment

The reason for the poor performance of the PbS CQD tandem solar cell presented in section 5.3 is largely due to a reduced electrical field for extracting charge carriers when narrow bandgap quantum dots are applied in the rear cell as an absorbing layer. This would lead to poor charge carrier extraction in the rear cell part resulting in both reduced rear cell current and hindered charge recombination in the interlayers. So the tandem cell's current density as well as overall tandem cell performance was unsatisfying. Motivated by a graded band alignment strategy[328, 347, 348] which has shown effectiveness for improving single-junction PbS CQD solar cells' performance by increasing the current densities, this strategy was applied on PbS CQD tandem solar cells in this section to further improve the tandem cells' performance for the first time.

Before applying the graded band alignment strategy in a tandem structure, the rear cell was investigated with applying this strategy. The graded band alignment was achieved by adjusting both the band offsets of the interlayer ZnO-nanoparticles (NPs) and the quantum dot layer in the single-junction rear cell. First, the conduction band of ZnO-NPs was deepened using $MgCl_2$ surface treatment.[349] This treatment is to shift the conduction band of ZnO downward as illustrated in section 3.6 in chapter 3 (Figure 3-13). Second, utilising the quantum dots' tunable bandgap a graded structure was fabricated, [328] which is also in favor of charge extraction due to the enhanced electrical field the graded structure offers. This combined modification favors electron extraction and improved rear cell's current density from 23.6 mA/cm^2 to 26 mA/cm^2. J-V curves of single-junction rear cell and the modifications in band offset with and without graded band alignment are shown in Figure 5-11.
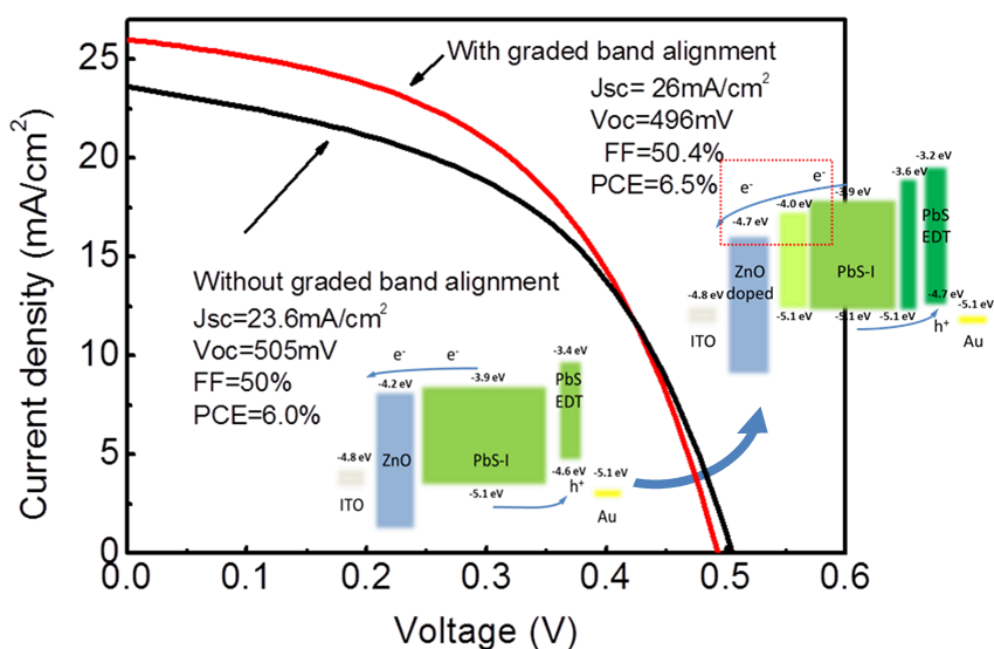
Figure 5-11 J-V curves of single-junction rear cells with and without graded band alignment. The graded band alignment increases the PCE of single-junction cells mainly due to increased current density. Quantum dots for the absorbing layer in these two single-junction cells have the same bandgap of 1.22 eV.

5.6.2 Improving PbS CQD tandem solar cell by graded band alignment

After investigating the improvement on single-junction rear cell, the graded band alignment was applied on the monolithic PbS CQD tandem solar cell for solving the poor carriers' extraction problem. Similarly, the graded band alignment was realised by applying a combined modification to both interlayer ZnO-nanoparticles (NPs) and rear cell quantum dots. On the one hand, the conduction band ZnO-NPs can be tuned downward by using MgCl$_2$ surface treatment.[349] The treatment shifts down the conduction band of ZnO to be lower than that of PbS in the rear cell as discussed above. On the other hand, utilising quantum dots' tunable bandgaps, a graded rear cell band structure was achieved,[328] which also favours charge extraction due to the enhanced electrical field. The modified band offset is shown in Figure 5-12. UPS data and band energy parameters [150, 328, 329] are supplied in Figure 3-13 (section 3.6) and Table 5-3. By utilising this graded band alignment in the tandem cell, not only charge carrier extraction is improved,[328, 347, 350] but also the carriers'

recombination in the Au interlayer can be improved due to higher carrier density in the vicinity of the recombination layer.
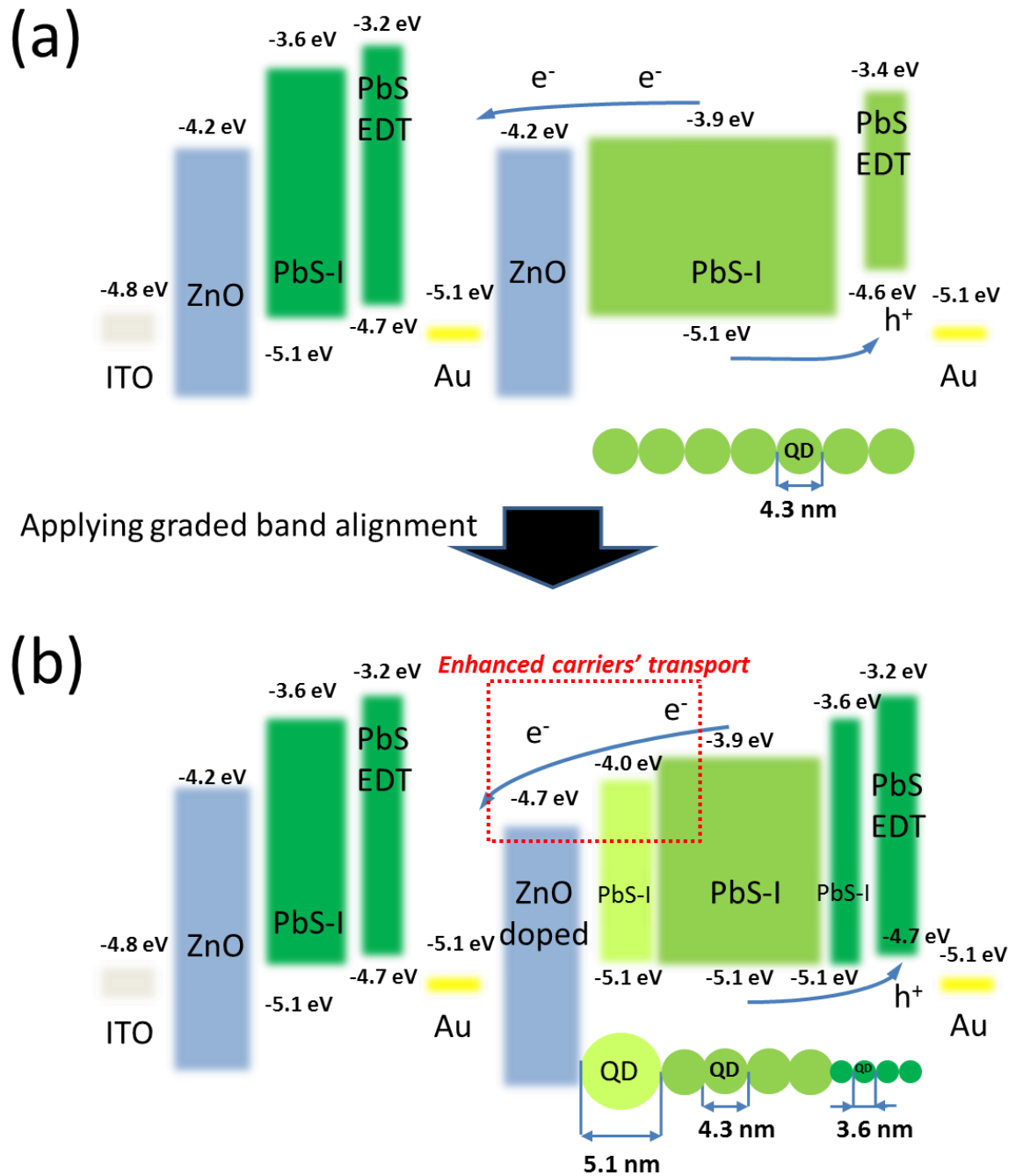
Figure 5-12 Illustration of PbS CQD tandem solar cell's band offsets without (a) and with (b) a graded band alignment. Surface treated ZnO nanoparticles at the interlayer and PbS quantum dots with different sizes were utilised for creating a graded band structure. This graded structure is in favour of charge carriers' extraction.

	5.1 nm PbS-I	4.3 nm PbS-I	3.6 nm PbS-I	4.3 nm PbS-EDT	3.6 nm PbS-EDT
Conduction band	-4.0 eV	-3.9 eV	-3.6 eV	-3.4	-3.2 eV
Valance band	-5.1 eV	-5.1 eV	-5.1 eV	-4.6	-4.7 eV

A PbS CQD tandem solar cell with graded band alignment was successfully fabricated, and the cross-sectional SEM image of the tandem cell is shown in Figure 5-13. The fabricated PbS CQD tandem solar cell is in a structure of ITO glass / ZnO-NP (80 nm) / 1.5 eV PbS CQDs (190 nm) / Au (2 nm) / ZnO-NP (80 nm) / 1.22 eV CQDs (300 nm) / Au (100 nm). For the PbS CQD tandem solar cell with graded band alignment, the first layer and the last layer spin-casted of the rear cell absorbing layer are using 1.14 eV CQDs and 1.5 eV quantum dots respectively for creating the graded structure. The PbS-EDT (p-type) layer is with 1.5 eV quantum dots for fitting with the grade structure.
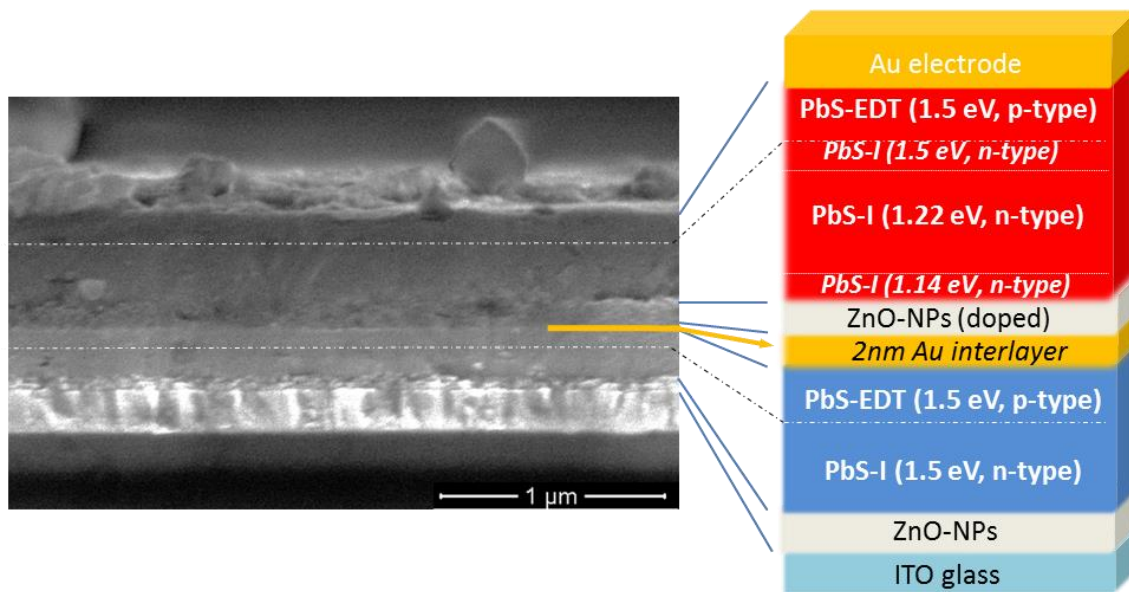
Figure 5-13 Cross-sectional SEM image of PbS CQD tandem solar cell with graded band alignment. The cell is in a structure of ITO glass/ ZnO-NP/Front cell absorbing layer (190 nm)/Au(2 nm)/ZnO-NP(doped)/Rear cell absorbing layer (300 nm)/Au. The rear cell absorbing layer is in a graded structure with quantum dots with different bandgaps.

By applying this graded band alignment, the PbS CQD tandem solar cell's performance was increased. J-V curves of the tandem cell and corresponding single-junction cells are shown in Figure 5-14. By applying the graded band alignment, the power conversion efficiency of the tandem cell was improved to 6.8% (Champion cell efficiency). Parameters of tandem cells and corresponding single-junction cells are listed in Table 5-4. The tandem cell's performance was improved mainly because of the graded band structure leading to a better charge carrier extraction. [328, 347, 350]
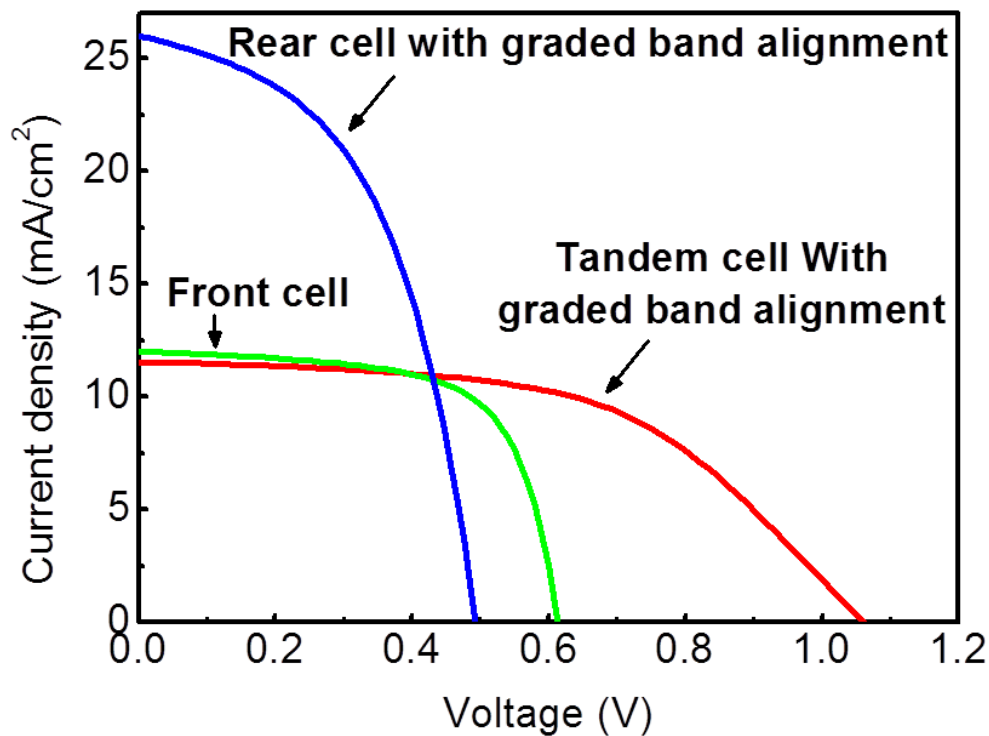
Figure 5-14 J-V curves of the PbS CQD tandem solar cell and corresponding single-junction cells with graded band alignment. The red curve is the tandem cell's J-V curve (champion cell). The green curve represents the front single-junction cell. The blue curve is for the rear single-junction cell.

Table 5-4 Parameters of the PbS CQD tandem cell and corresponding single-junction cells with graded band alignment. The champion cell of PCE=6.8% was achieved.

	J_{SC} (mA/cm^2)	V_{OC}(V)	FF (%)	PCE (%)
Front cell	12.0	0.61	66	4.8
Rear cell (Single)	26.0	0.50	50	6.5
Tandem cell	11.5	1.07	55	6.8
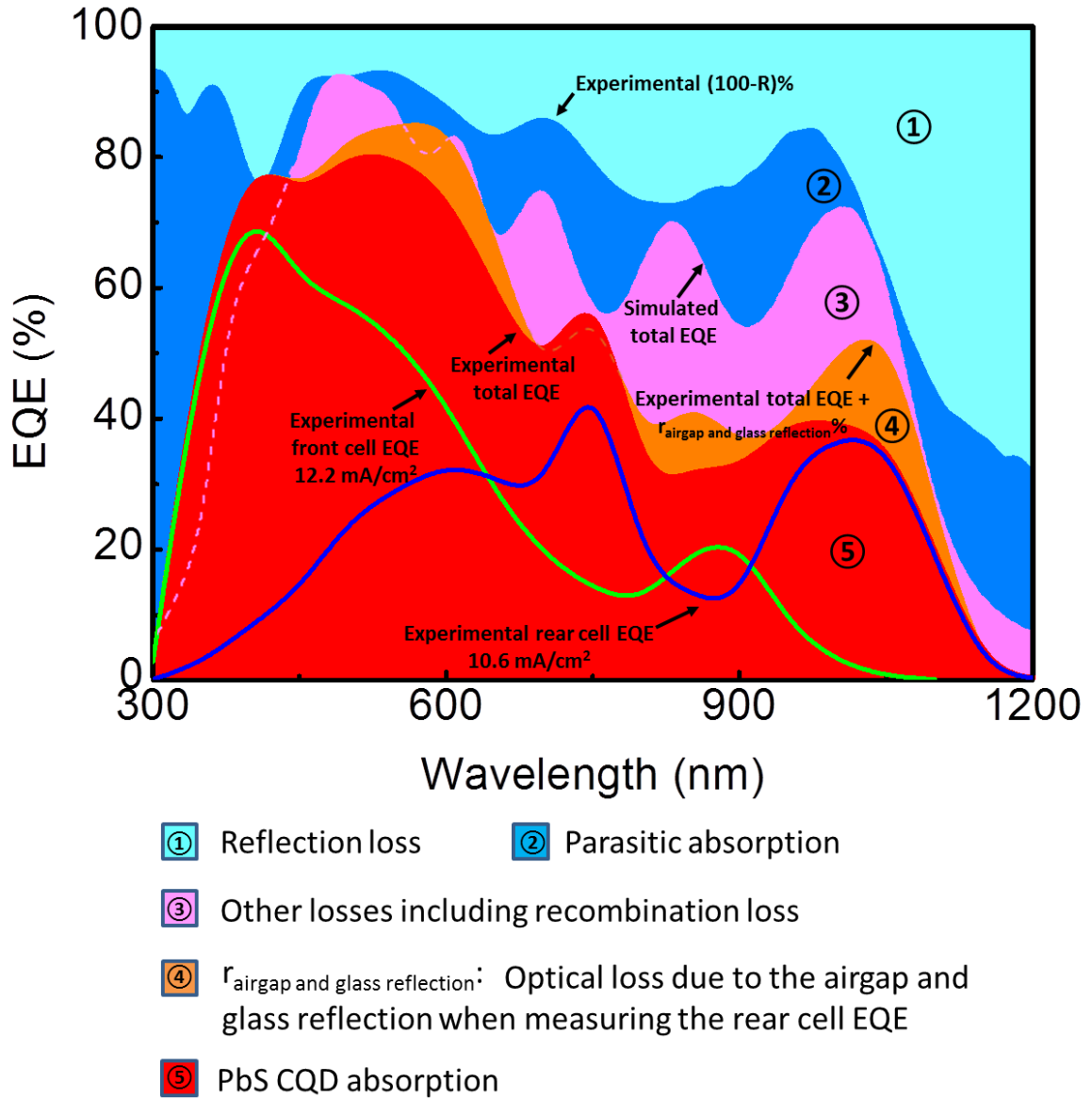
Figure 5-15 Experimental EQEs of subcells of the PbS CQD tandem solar cell with graded band alignment and loss analysis based on the simulated and experimental EQEs. The front cell integrated current density is 12.2 mA/cm² while that of the rear cell is 10.6 mA/cm². The measurement method (illustrated in Figure S8) with the front filter introduces a systematic difference between the measured and simulated rear cell currents. This is due to the airgap and additional glass reflection introduced in the measurement. Loss mechanisms accounted for the tandem cell include reflection loss (① cyan), parasitic absorption (② blue), recombination from defects (③ pink), and optical loss due to the airgap and glass reflection when measuring rear cell EQE (④ orange). Red area (⑤) represents the experimental total absorption of quantum dots by adding up the measured front cell and rear cell EQEs.

Experimental EQEs of subcells of fabricated PbS CQD tandem solar cell with graded band alignment are shown in Figure 5-15. In this tandem cell, the rear cell with an absorbing range extended to ~1200 nm could compensate for transmission losses by absorbing photons transmitted through the front cell and interlayer. Comparing the experimental EQEs in Figure 5-15 and the simulated EQEs in Figure 4-6(c), the experimental current densities are lower than the simulated theoretical maximum values. An important reason for this is that the rear cell EQE was measured using a single-junction front cell as a filter (Figure 5-16).[77, 343] This method to perform the EQE measurement was used because the front cell and rear cell spectrally overlap with each other, which leads to difficulty in separating their contribution to the EQE in a monolithic device.[344] This measurement method introduces an extra reflection by the air gap and additional ITO glass (as shown in Figure 5-16). This part of the reflection loss (region 4, orange), $r_{airgap\ and\ glass\ reflection}$ (reflection caused by airgap and additional glass) , was obtained by simulation. This reflection is present when measuring the rear cell EQE using a filter, but it does not exist in the monolithic tandem device. Therefore, the J-V current density (11.5 mA/cm^2) of the tandem device with a graded band alignment (Figure 5-14 and Table 5-4) is higher than the EQE integrated current density (10.6 mA/cm^2) for the rear cell.

Except for the reflection loss in Figure 5-15 (region 4, orange) caused by the measurement method, other important reasons for the difference between the simulated (region 3, pink) and experimental (region 5, red) results include the recombination loss and current loss due to non-optimized carrier extraction in the CQD tandem solar cells, which cannot be included in the PVlighthouse SunSolve module. Reduction in recombination loss requires improvements in charge carriers' lifetime. The dominant contribution to improved lifetimes in quantum dot devices stems from improved quantum dot surface passivation to reduce non-radiative recombination loss. One strategy to further improve the carrier extraction in CQD solar cells is the graded band alignment described in this section, which shows that optimizing the band alignment in each subcell as well as the interlayer would enhance carrier extraction and hence improve currents. Also as shown in the optical analysis in Figure 5-15, reflection loss (region 1, cyan) and parasitic absorption (region 2, blue) loss are both major loss mechanisms, which can be reduced by applying an anti-reflection coating and low-absorption functional interlayers. Detailed strategies for further improving PbS CQD tandem solar cell performance for the future are specified in 6.2 Future Work in chapter 6.
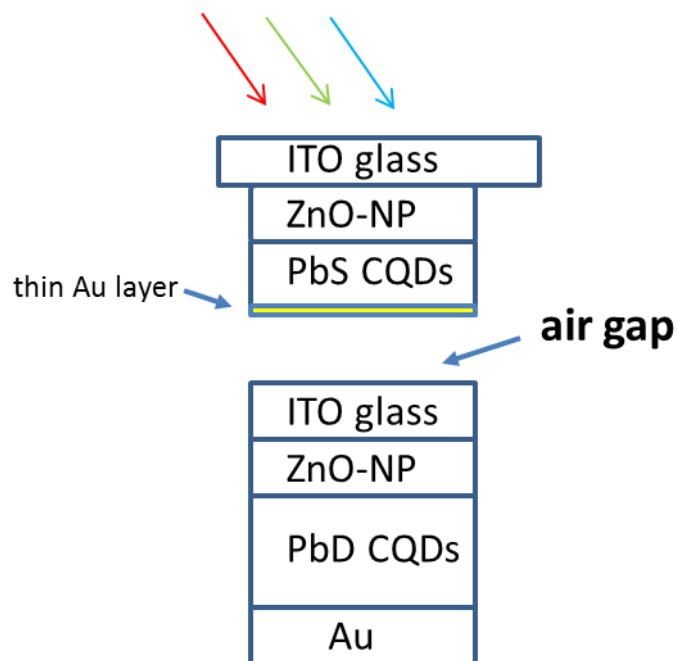
Figure 5-16 A Scheme diagram for EQE measurement of the rear cell using a single-junction front cell as a filter. This configuration introduces an air-gap in between the sub-cells and additional ITO glass absorption compared with the monolithic tandem structure. The air-gap causes light scattering and additional interfaces, so that there would be additional light loss and current drop in the measured EQE of the rear cell. The additional ITO glass's absorption may also reduce current but is with minor influence.

5.6 Conclusion

In this chapter, PbS CQD tandem solar cells are experimentally fabricated and investigated. Different interlayers of Au and ITO were studied. ITO as a transparent material has shown its potential to be an effective interlayer in PbS CQD tandem solar cell. The PbS CQD tandem solar cell with a simplified monolayer ITO interlayer reached an efficiency of 4.9%.

A graded band alignment strategy employing multiple innovations including ZnO-doping and quantum dot bandgap tuning has improved carriers' extraction and this strategy successfully improved the tandem cell performance from 4.5% to 6.8% for PbS CQD tandem solar cell with Au interlayer. This is the first time this strategy being applied on PbS CQD solar cell. the application of this strategy can still be extended to improve other thin film tandem solar cells.

Chapter 6. Conclusion and Future Work

6.1 Conclusion

Colloidal quantum dots are perfect candidate materials for making tandem solar cells not only because of their tunable bandgaps which offer great convenience for tandem cell design, but also because that the tandem cell strategy is a dedicated solution for the fundamental problem of the quantum dots' low absorbance together with limits placed on the thickness of the absorbing layer due to poor transport properties. Nonetheless, PbS CQD tandem solar cell development has lagged far behind single-junction CQD solar cells. This research addresses the problem of current matching using an optical modelling and the problem of the rear cell's poor carriers' extraction using graded band alignment for PbS CQD tandem solar cells. With the innovations applied, the tandem cell's efficiency surpassed that of its single-junction counterparts in this research.

Firstly, for fabricating a PbS CQD tandem solar cell, single-junction PbS CQD solar cells were studied and improved so that solid building blocks can be made for constructing multi-junction tandem solar cells. A simple $MgCl_2$ treatment to ZnO-NPs electron transport layer was developed for improving the single-junction PbS CQD solar cell. The single-junction cell's performance was improved because of increased short circuit current J_{SC} and fill factor FF. J_{SC} increased from 20 mA/cm^2 to 22 mA/cm^2 and FF rose from 53% to 62% respectively. The $MgCl_2$ treated electron transport layer can be applied in both single-junction cells and tandem cells as interlayers.

Secondly, for making an efficient PbS CQD tandem solar cell, modellings were also established as guidance for the experimental work on PbS CQD tandem cell fabrication. As the most challenging part for making a higher performance tandem cell is adjusting subcells to have matched currents, an optical modelling was specially established to deal with this current matching problem. By this optical modelling, the PbS CQD tandem solar cell's parameters were optimised, including the subcells' bandgaps, interlayer thickness and absorbing layer thicknesses. It is shown that the maximised J_{SC} of PbS CQD tandem solar cell

can reach 15.3 mA/cm^2 under optimised conditions. The optical modelling also shows that a 2nm Au layer is sufficient to inter-connect subcells to achieve good current. A diode modelling established in this research shows that an efficiency of 15.5% can be expected for PbS CQD tandem solar cell.

Finally, PbS CQD tandem solar cells were successfully fabricated and investigated. Different interlayers of Au and ITO were both applied and studied in fabricated PbS CQD tandem solar cells. For the first time a simplified mono-layer ITO interlayer was introduced for PbS CQD tandem solar cells in this research, and the tandem cell's efficiency reached 4.9%. A graded band alignment strategy was applied to further improve PbS CQD tandem cell performance with Au interlayer. A problem of poor carrier extraction for the rear cell was identified and then solved by a graded band alignment. This graded band alignment strategy usefully pushed the tandem cell efficiency from 4.5% to 6.8%. This strategy can be further applied to other kind of thin film tandem solar cells in the future.

6.2 Future work

In this research, numeral innovations have been made for improving PbS CQD tandem solar cell as well as single-junction PbS solar cell. In the meantime, a series of works can be considered as future projects for further developing PbS quantum dot based solar cells.

Firstly, for developing PbS quantum dot based solar cells, PbS quantum dots need to be improved in the first place. Surface passivation is important for reducing quantum dots' surface defects which determines the solar cell's voltage. For improving quantum dot surface passivation, not only novel ligands need to be developed, but also ligand exchange method is playing an important role in the quality of passivation. So, while looking for short effective novel ligands, solution-phase ligand exchange which shows a potential for a higher PbS solar cell efficiency than conventional solid-state ligand exchange should be paid more attention in the future research.

Secondly, as the limiting part is the rear cell for PbS CQD tandem solar cells based on experience in this research, developing high-quality low-bandgap PbS quantum dots became an important task. However, producing low-bandgap quantum dots and the following ligand exchange for these quantum dots are a challenging tasks for now. In the meantime, quantum

dots with an absorption extended to 1300-1500 nm (~0.7 eV) can be very appealing to not only tandem cell fabrication but also telecommunication research in particular. So developing low-bandgap PbS quantum dots can be a promising future research project. For achieving this, the synthesis conditions need to be revised judiciously including but not limited to using higher temperature injection method and developing novel precursors. Ligands for low-bandgap quantum dot surface passivation can also be an research project where developing novel ligands can be considered such as zinc or cadmium containing compounds which have shown effectiveness on quantum dot surface passivation.

Thirdly, as the optical modelling in this research mainly focuses on simulating optical properties, novel modelling methods can be developed for having a more comprehensive simulation. Instead of just simulating the optical properties, more characters such as carriers' extraction and recombination mechanisms can also be incorporated into consideration, where more skills on physics and computer programming are possibly needed. More skilled-needed softwares such as Comsol can be utilised to perform a more systematic and complicated simulation work. For now there is still a large room for developing quantum dot based electronic devices modelling.

Fourthly, using solution-processed interlayers is an attractive tactics for making tandem cells as this would simplify the processing and provides convenience for future industrial manufacture. A series of candidates can be taken into consideration such as PEDOT (poly(3,4-ethylenedioxythiophene) polystyrene sulfonate), gold nanoparticles, colloidal graphene nano-flakes, 2D ITO nano-sheets. Besides, Atomic Layer Deposition (ALD) processed transparent materials can also be promising candidates for interlayers as this method can provide a mild fabrication process which brings minimised damage to the as-fabricated subcells.

List of Publications

First author papers:

1. <u>Gao, Y.</u>; Zheng, J.; Chen, W.; Yuan, L.; Teh, Z. L.; Yang, J.; Cui, X.; Conibeer, G.; Patterson, R.; Huang, S., *Enhancing PbS Colloidal Quantum Dot Tandem Solar Cell Performance by Graded Band Alignment*. *The Journal of Physical Chemistry Letters* **2019,** 10, 5729-5734.

2. <u>Gao, Y.</u>; Patterson, R.; Hu, L.; Yuan, L.; Zhang, Z.; Hu, Y.; Chen, Z.; Teh, Z. L.; Conibeer, G.; Huang, S., *$MgCl_2$ Passivated ZnO Electron Transporting Layer to Improve PbS Quantum Dot Solar Cells. Nanotechnology* **2018,** 30, 085403.

Co-authored papers:

1. Huang, S.; Hu, L.; Patterson, R.; Zhang, Z.; Yuan, L.; Chen, W.; Hu, Y.; Chen, Z.; <u>Gao, Y.</u>; Teh, Z. L. *Improving Hole Extraction for PbS Quantum Dot Solar Cells*, 2018 IEEE 7th World Conference on Photovoltaic Energy Conversion (WCPEC)(A Joint Conference of 45th IEEE PVSC, 28th PVSEC & 34th EU PVSEC), 2018; IEEE: pp 2756-2758.

2. Hu, L.; Patterson, R. J.; Zhang, Z.; Hu, Y.; Li, D.; Chen, Z.; Yuan, L.; Teh, Z. L.; <u>Gao, Y.</u>; Conibeer, G. J., *Enhanced Optoelectronic Performance in $AgBiS_2$ Nanocrystals Obtained via an Improved Amine-based Synthesis Route. Journal of Materials Chemistry C* **2018,** 6, 731-737.

3. The, Z. L., Hu, Long., Zhang, Z., Gentle, A. R., Chen, Z., <u>Gao, Y.</u>, Yuan, L., Hu, Y., Patterson, R. J., Huang, S., *Enhanced Power Conversion Efficiency via Hybrid Ligand Exchange Treatment of p-type PbS Quantum Dot*. (submitted manuscript)

References

1.   Luther, J. M.; Gao, J.; Lloyd, M. T.; Semonin, O. E.; Beard, M. C.; Nozik, A. J., *Stability Assessment on a 3% Bilayer PbS/ZnO Quantum Dot Heterojunction Solar Cell*. *Advanced Materials* **2010,** 22, 3704-3707.

2.   Xu, J.; Voznyy, O.; Liu, M.; Kirmani, A. R.; Walters, G.; Munir, R.; Abdelsamie, M.; Proppe, A. H.; Sarkar, A.; Garcia de Arquer, F. P., et al., *2D matrix engineering for homogeneous quantum dot coupling in photovoltaic solids*. *Nat Nanotechnol* **2018,** 13, 456-462.

3.   O'Reilly, C. M.; Sharma, S.; Gray, D. K.; Hampton, S. E.; Read, J. S.; Rowley, R. J.; Schneider, P.; Lenters, J. D.; McIntyre, P. B.; Kraemer, B. M., et al., *Rapid and highly variable warming of lake surface waters around the globe*. *Geophysical Research Letters* **2015,** 42, 2015GL066235.

4.   Sharma, S.; Gray, D. K.; Read, J. S.; O'Reilly, C. M.; Schneider, P.; Qudrat, A.; Gries, C.; Stefanoff, S.; Hampton, S. E.; Hook, S., et al., *A global database of lake surface temperatures collected by in situ and satellite methods from 1985–2009*. *Scientific Data* **2015,** 2, 150008.

5.   Vorosmarty, C. J.; Green, P.; Salisbury, J.; Lammers, R. B., *Global water resources: Vulnerability from climate change and population growth*. *Science* **2000,** 289, 284-288.

6.   Khalil, H. B.; Zaidi, S. J. H., *Energy crisis and potential of solar energy in Pakistan*. *Renewable and Sustainable Energy Reviews* **2014,** 31, 194-201.

7.   Şen, Z., *Solar energy in progress and future research trends*. *Progress in Energy and Combustion Science* **2004,** 30, 367-416.

8.   Arent, D. J.; Wise, A.; Gelman, R., *The status and prospects of renewable energy for combating global warming*. *Energy Economics* **2011,** 33, 584-593.

9.   Tabassum, A.; Premalatha, M.; Abbasi, T.; Abbasi, S. A., *Wind energy: Increasing deployment, rising environmental concerns*. *Renewable and Sustainable Energy Reviews* **2014,** 31, 270-288.

10.   Manders, T. N.; Höffken, J. I.; van der Vleuten, E. B. A., *Small-scale hydropower in the Netherlands: Problems and strategies of system builders*. *Renewable and Sustainable Energy Reviews* **2016,** 59, 1493-1503.

11.   Williams, P. R. D.; Inman, D.; Aden, A.; Heath, G. A., *Environmental and sustainability factors associated with next-generation biofuels in the U.S.: What do we really know? Environmental Science and Technology* **2009,** 43, 4763-4775.

12.   Mekhilef, S.; Saidur, R.; Safari, A., *A review on solar energy use in industries*. *Renewable and Sustainable Energy Reviews* **2011,** 15, 1777-1790.

13.   Becquerel, A., *On electric effects under the influence of solar radiation*. *CR Acad. Sci* **1839,** 9, 711-714.

14.   Adams, W. G.; Day, R. E., *The Action of Light on Selenium*. *Philosophical Transactions of the Royal Society of London* **1877,** 167, 313-349.

15.   Trivich, D.; Wang, E. Y.; Komp, R. J.; Kakar, A. S., *Cuprous oxide photovoltaic cells*. ; Wayne State Univ., Detroit, MI (USA): 1978; p Medium: ED; Size: Pages: 5.

16.   Loferski, J. J., *The first forty years: A brief history of the modern photovoltaic age*. *Progress in Photovoltaics: Research and Applications* **1993,** 1, 67-78.

17.   Chapin, D. M.; Fuller, C. S.; Pearson, G. L., *A New Silicon p‐n Junction Photocell for Converting Solar Radiation into Electrical Power*. *Journal of Applied Physics* **1954,** 25, 676-677.

18.   Rappaport, P., *The Electron-Voltaic Effect in $p-n$ Junctions Induced by Beta-Particle Bombardment*. *Physical Review* **1954,** 93, 246-247.

19.   Reynolds, D. C.; Leies, G.; Antes, L. L.; Marburger, R. E., *Photovoltaic Effect in Cadmium Sulfide*. *Physical Review* **1954,** 96, 533-534.

20.   Pfann, W. G.; Van Roosbroeck, W., *Radioactive and Photoelectric p‐n Junction Power Sources*. *Journal of Applied Physics* **1954,** 25, 1422-1434.

21.   Shockley, W.; Queisser, H. J., *Detailed Balance Limit of Efficiency of p‐n Junction Solar Cells*. *Journal of Applied Physics* **1961,** 32, 510-519.

22.   Shockley, W.; Read, W. T., *Statistics of the Recombinations of Holes and Electrons*. *Physical Review* **1952,** 87, 835-842.

23.   Sah, C. t.; Noyce, R. N.; Shockley, W., *Carrier Generation and Recombination in P-N Junctions and P-N Junction Characteristics*. *Proceedings of the IRE* **1957,** 45, 1228-1243.

24.   Prince, M. B., *Silicon Solar Energy Converters*. *Journal of Applied Physics* **1955,** 26, 534-540.

25.   Green, M. A., High Efficiency Silicon Solar Cells. In *Seventh E.C. Photovoltaic Solar Energy Conference: Proceedings of the International Conference, held at Sevilla, Spain, 27–31 October 1986*, Goetzberger, A.; Palz, W.; Willeke, G., Eds. Springer Netherlands: Dordrecht, 1987; pp 681-687.

26.   Green, M. A.; Wenham, S. R.; Zhao, J.; Zolper, J.; Blakers, A. W. In *Recent improvements in silicon solar cells and module efficiency*, Photovoltaic Specialists Conference, 1990., Conference Record of the Twenty First IEEE, 21-25 May 1990, 1990; pp 207-210 vol.201.

27.   Loferski, J. J., *Theoretical Considerations Governing the Choice of the Optimum Semiconductor for Photovoltaic Solar Energy Conversion*. *Journal of Applied Physics* **1956,** 27, 777-784.

28.   Cherry, W. In *Military considerations for a photovoltaic solar energy converter*, Transactions of the Conference on the Use of Solar Energy, University of Arizona, Tuscon, 1955; p 127.

29.   Wolf, M., *Limitations and Possibilities for Improvement of Photovoltaic Solar Energy Converters: Part I: Considerations for Earth's Surface Operation*. *Proceedings of the IRE* **1960,** 48, 1246-1263.

30.   Werner, J. H.; Kolodinski, S.; Queisser, H. J., *Novel optimization principles and efficiency limits for semiconductor solar cells*. *Physical Review Letters* **1994,** 72, 3851-3854.

31.   Bergmann, R. B., *Crystalline Si thin-film solar cells: a review*. *Applied Physics A* **1999,** 69, 187-194.

32.   Ferber, J.; Stangl, R.; Luther, J., *An electrical model of the dye-sensitized solar cell*. *Solar Energy Materials and Solar Cells* **1998,** 53, 29-54.

33.   Kosten, E. D.; Atwater, J. H.; Parsons, J.; Polman, A.; Atwater, H. A., *Highly efficient GaAs solar cells by limiting light emission angle*. *Light Sci Appl* **2013,** 2, e45.

34.   Reber, S.; Wettling, W., *High-temperature processing of crystalline silicon thin-film solar cells*. *Applied Physics A* **1999,** 69, 215-220.

35.   Smith, D. D.; Cousins, P. J.; Masad, A.; Waldhauer, A.; Westerberg, S.; Johnson, M.; Tu, X.; Dennis, T.; Harley, G.; Solomon, G., et al. In *Generation III high efficiency lower cost technology: Transition to full scale manufacturing*, Photovoltaic Specialists Conference (PVSC), 2012 38th IEEE, 3-8 June 2012, 2012; pp 001594-001597.

36.   Todorov, T. K.; Reuter, K. B.; Mitzi, D. B., *High-Efficiency Solar Cell with Earth-Abundant Liquid-Processed Absorber*. *Advanced Materials* **2010,** 22, E156-E159.

37.   Xing, G.; Mathews, N.; Lim, S. S.; Yantara, N.; Liu, X.; Sabba, D.; Grätzel, M.; Mhaisalkar, S.; Sum, T. C., *Low-temperature solution-processed wavelength-tunable perovskites for lasing*. *Nat Mater* **2014,** 13, 476-480.

38.   O'Regan, B.; Gratzel, M., *A low-cost, high-efficiency solar cell based on dye-sensitized colloidal TiO2 films*. *Nature* **1991,** 353, 737-740.

39.   Rostalski, J. O.; Meissner, D., *Monochromatic versus solar efficiencies of organic solar cells*. *Solar Energy Materials and Solar Cells* **2000,** 61, 87-95.

40.   Würfel, P., *Solar energy conversion with hot electrons from impact ionisation*. *Solar Energy Materials and Solar Cells* **1997,** 46, 43-52.

41.   Luque, A.; Martí, A., *Increasing the efficiency of ideal solar cells by photon induced transitions at intermediate levels*. *Physical Review Letters* **1997,** 78, 5014-5017.

42.   Sariciftci, N. S.; Smilowitz, L.; Heeger, A. J.; Wudl, F., *Photoinduced electron transfer from a conducting polymer to buckminsterfullerene*. *Science* **1992,** 258, 1474-1476.

43.   Blakers, A. W.; Wang, A.; Milne, A. M.; Zhao, J.; Green, M. A., *22.8% efficient silicon solar cell*. *Applied Physics Letters* **1989,** 55, 1363-1365.

44.   Woodall, J. M., *High-efficiency Ga1−xAlxAs[Single Bond]GaAs solar cells*. *Applied Physics Letters* **1972,** 21, 379.

45.   Zhao, J.; Green, M. A., *Optimized antireflection coatings for high-efficiency silicon solar cells*. *IEEE Transactions on Electron Devices* **1991,** 38, 1925-1934.

46.   Zhao, J.; Wang, A.; Altermatt, P. P.; Wenham, S. R.; Green, M. A., *24% efficient perl silicon solar cell: Recent improvements in high efficiency silicon cell research*. *Solar Energy Materials and Solar Cells* **1996,** 41, 87-99.

47.   Zhao, J.; Wang, A.; Green, M. A.; Ferrazza, F., *19.8% efficient "honeycomb" textured multicrystalline and 24.4% monocrystalline silicon solar cells*. *Applied Physics Letters* **1998,** 73, 1991-1993.

48.   Mazzarella, L.; Lin, Y. H.; Kirner, S.; Morales‑Vilches, A. B.; Korte, L.; Albrecht, S.; Crossland, E.; Stannowski, B.; Case, C.; Snaith, H. J., *Infrared Light Management Using a Nanocrystalline Silicon Oxide Interlayer in Monolithic Perovskite/Silicon Heterojunction Tandem Solar Cells with Efficiency above 25%*. *Advanced Energy Materials* **2019**, 1803241.

49.   Yoshikawa, K.; Kawasaki, H.; Yoshida, W.; Irie, T.; Konishi, K.; Nakano, K.; Uto, T.; Adachi, D.; Kanematsu, M.; Uzu, H., *Silicon heterojunction solar cell with interdigitated back contacts for a photoconversion efficiency over 26%*. *Nature Energy* **2017,** 2, 17032.

50.   Green, M. A.; Hishikawa, Y.; Dunlop, E. D.; Levi, D. H.; Hohl‑Ebinger, J.; Ho‑Baillie, A. W., *Solar cell efficiency tables (version 52)*. *Progress in Photovoltaics: Research and Applications* **2018,** 26, 427-436.

51.   Huijben, J. C. C. M.; Podoynitsyna, K. S.; van Rijn, M. L. B.; Verbong, G. P. J., *A review of governmental support instruments channeling PV market growth in the Flanders region of Belgium (2006–2013)*. *Renewable and Sustainable Energy Reviews* **2016,** 62, 1282-1290.

52.   Goetzberger, A.; Hebling, C.; Schock, H.-W., *Photovoltaic materials, history, status and outlook*. *Materials Science and Engineering: R: Reports* **2003,** 40, 1-46.

53.   Hannebauer, H.; Dullweber, T.; Baumann, U.; Falcon, T.; Brendel, R., *21.2%-efficient fineline-printed PERC solar cell with 5 busbar front grid*. *physica status solidi (RRL) – Rapid Research Letters* **2014,** 8, 675-679.

54.   Polman, A.; Knight, M.; Garnett, E. C.; Ehrler, B.; Sinke, W. C., *Photovoltaic materials: Present efficiencies and future challenges*. *Science* **2016,** 352, aad4424.

55.   Yan, C.; Barlow, S.; Wang, Z.; Yan, H.; Jen, A. K. Y.; Marder, S. R.; Zhan, X., *Non-fullerene acceptors for organic solar cells*. *Nature Reviews Materials* **2018,** 3, 18003.

56.   Ruf, F.; Magin, A.; Schultes, M.; Ahlswede, E.; Kalt, H.; Hetterich, M., *Excitonic nature of optical transitions in electroabsorption spectra of perovskite solar cells*. *Applied Physics Letters* **2018,** 112, 083902.

57.   Semonin, O. E.; Luther, J. M.; Choi, S.; Chen, H.-Y.; Gao, J.; Nozik, A. J.; Beard, M. C., *Peak External Photocurrent Quantum Efficiency Exceeding 100% via MEG in a Quantum Dot Solar Cell*. *Science* **2011,** 334, 1530-1533.

58.   Zhu, S.; Zhang, J.; Tang, S.; Qiao, C.; Wang, L.; Wang, H.; Liu, X.; Li, B.; Li, Y.; Yu, W., et al., *Surface Chemistry Routes to Modulate the Photoluminescence of Graphene Quantum Dots: From Fluorescence Mechanism to Up-Conversion Bioimaging Applications*. *Advanced Functional Materials* **2012,** 22, 4732-4740.

59.   Zhang, Z.; Yang, J.; Wen, X.; Yuan, L.; Shrestha, S.; Stride, J. A.; Conibeer, G. J.; Patterson, R. J.; Huang, S., *Effect of Halide Treatments on PbSe Quantum Dot Thin Films: Stability, Hot Carrier Lifetime, and Application to Photovoltaics*. *The Journal of Physical Chemistry C* **2015,** 119, 24149-24155.

60.   Sasaki, K.; Agui, T.; Nakaido, K.; Takahashi, N.; Onitsuka, R.; Takamoto, T. In *Development of InGaP/GaAs/InGaAs inverted triple junction concentrator solar cells*, AIP conference proceedings, 2013; AIP: pp 22-25.

61.   Cornfeld, A. In *Advances in the Performance of Inverted Metamorphic Multi-junction Solar Cells*, 23rd European Photovoltaic Energy Conference, 2008.

62.   King, R.; Bhusari, D.; Larrabee, D.; Liu, X. Q.; Rehder, E.; Edmondson, K.; Cotal, H.; Jones, R.; Ermer, J.; Fetzer, C., *Solar cell generations over 40% efficiency*. *Progress in Photovoltaics: Research and Applications* **2012,** 20, 801-815.

63.   Guter, W.; Kern, R.; Köstler, W.; Kubera, T.; Löckenhoff, R.; Meusel, M.; Shirnow, M.; Strobl, G. In *III－V multijunction solar cells—new lattice－matched products and development of upright metamorphic 3J cells*, AIP Conference Proceedings, 2011; AIP: pp 5-8.

64.   Dimroth, F.; Tibbits, T. N. D.; Niemeyer, M.; Predan, F.; Beutel, P.; Karcher, C.; Oliva, E.; Siefer, G.; Lackner, D.; Fuß-Kailuweit, P., et al., *Four-Junction Wafer-Bonded Concentrator Solar Cells*. *IEEE Journal of Photovoltaics* **2016,** 6, 343-349.

65.   Wang, G.; Melkonyan, F. S.; Facchetti, A.; Marks, T. J., *All－Polymer Solar Cells: Recent Progress, Challenges, and Prospects*. *Angewandte Chemie International Edition* **2019,** 58, 4129-4142.

66.   Lee, D.; Ki Bae, W.; Park, I.; Yoon, D. Y.; Lee, S.; Lee, C., *Transparent electrode with ZnO nanoparticles in tandem organic solar cells*. *Solar Energy Materials and Solar Cells* **2011,** 95, 365-368.

67.   Meng, L.; Zhang, Y.; Wan, X.; Li, C.; Zhang, X.; Wang, Y.; Ke, X.; Xiao, Z.; Ding, L.; Xia, R., *Organic and solution-processed tandem solar cells with 17.3% efficiency*. *Science* **2018,** 361, 1094-1098.

68.   Grancini, G.; Roldán-Carmona, C.; Zimmermann, I.; Mosconi, E.; Lee, X.; Martineau, D.; Narbey, S.; Oswald, F.; De Angelis, F.; Graetzel, M., *One-Year stable perovskite solar cells by 2D/3D interface engineering*. *Nature communications* **2017,** 8, 15684.

69.   Rühle, S., *Tabulated values of the Shockley–Queisser limit for single junction solar cells*. *Solar Energy* **2016,** 130, 139-147.

70.   Choi, H.; Ko, J.-H.; Kim, Y.-H.; Jeong, S., *Steric-Hindrance-Driven Shape Transition in PbS Quantum Dots: Understanding Size-Dependent Stability*. *Journal of the American Chemical Society* **2013,** 135, 5278-5281.

71.   Moreels, I.; Justo, Y.; De Geyter, B.; Haustraete, K.; Martins, J. C.; Hens, Z., *Size-Tunable, Bright, and Stable PbS Quantum Dots: A Surface Chemistry Study*. *ACS Nano* **2011,** 5, 2004-2012.

72.   Hines, M. A.; Scholes, G. D., *Colloidal PbS Nanocrystals with Size-Tunable Near-Infrared Emission: Observation of Post-Synthesis Self-Narrowing of the Particle Size Distribution*. *Adv. Mater.* **2003,** 15, 1844.

73.   Yuan, M.; Liu, M.; Sargent, E. H., *Colloidal quantum dot solids for solution-processed solar cells*. **2016,** 1, 16016.

74.   Nozik, A. J. In *Multiple exciton generation in semiconductor quantum dots and novel molecules: Applications to third generation solar photon conversion*, 2008 17th IEEE International Symposium on the Applications of Ferroelectrics, 23-28 Feb. 2008, 2008; pp 1-2.

75.   Wang, X.; Koleilat, G. I.; Tang, J.; Liu, H.; Kramer, I. J.; Debnath, R.; Brzozowski, L.; Barkhouse, D. A. R.; Levina, L.; Hoogland, S., et al., *Tandem colloidal quantum dot solar cells employing a graded recombination layer*. *Nat. Photonics* **2011,** 5, 480-484.

76.   Choi, J. J.; Wenger, W. N.; Hoffman, R. S.; Lim, Y.-F.; Luria, J.; Jasieniak, J.; Marohn, J. A.; Hanrath, T., *Solution-Processed Nanocrystal Quantum Dot Tandem Solar Cells*. *Adv. Materials* **2011,** 23, 3144-3148.

77.   Shi, G.; Wang, Y.; Liu, Z.; Han, L.; Liu, J.; Wang, Y.; Lu, K.; Chen, S.; Ling, X.; Li, Y., et al., *Stable and Highly Efficient PbS Quantum Dot Tandem Solar Cells Employing a Rationally Designed Recombination Layer*. *Advanced Energy Materials* **2017**, 1602667.

78.   Konstantatos, G.; Howard, I.; Fischer, A.; Hoogland, S.; Clifford, J.; Klem, E.; Levina, L.; Sargent, E. H., *Ultrasensitive Solution-Cast Quantum Dot Photodetectors*. *Nature* **2006,** 442, 180.

79.   Huang, L.; Tu, C. C.; Lin, L. Y., *Colloidal Quantum Dot Photodetectors Enhanced by Self-Assembled Plasmonic Nanoparticles*. *Appl. Phys. Lett.* **2011,** 98, 113110.

80.   Keuleyan, S.; Lhuillier, E.; Brajuskovic, V.; Guyot-Sionnest, P., *Mid-Infrared HgTe Colloidal Quantum Dot Photodetectors*. *Nat. Photonics* **2011,** 5, 489.

81.   Li, L.; Pandey, A.; Werder, D. J.; Khanal, B. P.; Pietryga, J. M.; Klimov, V. I., *Efficient Synthesis of Highly Luminescent Copper Indium Sulfide-Based Core/Shell Nanocrystals with Surprisingly Long-Lived Emission*. *J. Am. Chem. Soc.* **2011,** 133, 1176.

82.   Qian, L.; Zheng, Y.; Xue, J.; Holloway, P. H., *Stable and Efficient Quantum-Dot Light-Emitting Diodes Based on Solution-Processed Multilayer Structures*. *Nat. Photonics* **2011,** 5, 543.

83.   Steckel, J. S.; Coe-Sullivan, S.; Bulović, V.; Bawendi, M. G., *1.3 μm to 1.55 μm Tunable Electroluminescence from PbSe Quantum Dots Embedded within an Organic Device*. *Adv. Mater.* **2003,** 15, 1862.

84.   Donegá, C. d. M., *Synthesis and Properties of Colloidal Heteronanocrystals*. *Chem. Soc. Rev.* **2011,** 40, 1512.

85.   Wise, F. W., *Lead Salt Quantum Dots: the Limit of Strong Quantum Confinement*. *Accounts of Chemical Research* **2000,** 33, 773-780.

86.   Kovalenko, M. V.; Scheele, M.; Talapin, D. V., *Colloidal Nanocrystals with Molecular Metal Chalcogenide Surface Ligands*. *Science* **2009,** 324, 1417-1420.

87.   Talapin, D. V.; Lee, J.-S.; Kovalenko, M. V.; Shevchenko, E. V., *Prospects of colloidal nanocrystals for electronic and optoelectronic applications*. *Chemical reviews* **2009,** 110, 389-458.

88.   Ip, A. H.; Thon, S. M.; Hoogland, S.; Voznyy, O.; Zhitomirsky, D.; Debnath, R.; Levina, L.; Rollny, L. R.; Carey, G. H.; Fischer, A., et al., *Hybrid passivated colloidal quantum dot solids*. *Nat Nanotechnol* **2012,** 7, 577-582.

89.   Zhang, J.; Gao, J.; Church, C. P.; Miller, E. M.; Luther, J. M.; Klimov, V. I.; Beard, M. C., *PbSe Quantum Dot Solar Cells with More Than 6% Efficiency Fabricated in Ambient Atmosphere*. *Nano Lett.* **2014,** 14, 6010.

90.   Murray, C. B.; Norris, D. J.; Bawendi, M. G., *Synthesis and Characterization of Nearly Monodisperse CdE (E = Sulfur, Selenium, Tellurium) Semiconductor Nanocrystallites*. *J. Am. Chem. Soc.* **1993,** 115, 8706.

91.   Park, J.; Joo, J.; Kwon, S. G.; Jang, Y.; Hyeon, T., *Synthesis of Monodisperse Spherical Nanocrystals*. *Angew. Chem., Int. Ed.* **2007,** 46, 4630.

92.   Thanh, N. T. K.; Maclean, N.; Mahiddine, S., *Mechanisms of Nucleation and Growth of Nanoparticles in Solution*. *Chem. Rev.* **2014,** 114, 7610.

93.   Reiss, H., *The Growth of Uniform Colloidal Dispersions*. *J. Chem. Phys.* **1951,** 19, 482.

94.   Carey, G. H.; Abdelhady, A. L.; Ning, Z.; Thon, S. M.; Bakr, O. M.; Sargent, E. H., *Colloidal Quantum Dot Solar Cells*. *Chemical Reviews* **2015,** 115, 12732-12763.

95.   Protesescu, L.; Yakunin, S.; Bodnarchuk, M. I.; Krieg, F.; Caputo, R.; Hendon, C. H.; Yang, R. X.; Walsh, A.; Kovalenko, M. V., *Nanocrystals of cesium lead halide perovskites (CsPbX3, X= Cl, Br, and I): novel optoelectronic materials showing bright emission with wide color gamut*. *Nano letters* **2015,** 15, 3692-3696.

96.   Kwon, S. G.; Piao, Y.; Park, J.; Angappane, S.; Jo, Y.; Hwang, N. M.; Park, J. G.; Hyeon, T., *Kinetics of Monodisperse Iron Oxide Nanocrystal Formation by "Heating-Up" Process*. *J. Am. Chem. Soc.* **2007,** 129, 12571.

97.   Pan, J.; El-Ballouli, A. O.; Rollny, L.; Voznyy, O.; Burlakov, V. M.; Goriely, A.; Sargent, E. H.; Bakr, O. M., *Automated Synthesis of Photovoltaic-Quality Colloidal Quantum Dots Using Separate Nucleation and Growth Stages*. *ACS Nano* **2013,** 7, 10158.

98.   Hines, M. A.; Scholes, G. D., *Colloidal PbS Nanocrystals with Size-Tunable Near-Infrared Emission: Observation of Post-Synthesis Self-Narrowing of the Particle Size Distribution*. *Advanced Materials* **2003,** 15, 1844-1849.

99.   Cademartiri, L.; Bertolotti, J.; Sapienza, R.; Wiersma, D. S.; Von Freymann, G.; Ozin, G. A., *Multigram scale, solventless, and diffusion-controlled route to highly monodisperse PbS nanocrystals*. *The Journal of Physical Chemistry B* **2006,** 110, 671-673.

100.   Brus, L., *Electronic Wave Functions in Semiconductor Clusters: Experiment and Theory*. *J. Phys. Chem.* **1986,** 90, 2555.

101.   Yu, W. W.; Qu, L.; Guo, W.; Peng, X., *Experimental Determination of the Extinction Coefficient of CdTe, CdSe, and CdS Nanocrystals*. *Chem. Mater.* **2003,** 15, 2854.

102.   Moreels, I.; Justo, Y.; De Geyter, B.; Haustraete, K.; Martins, J. C.; Hens, Z., *Size-Tunable, Bright, and Stable PbS Quantum Dots: A Surface Chemistry Study*. *ACS Nano* **2011,** 5, 2004.

103.   Kumar, S.; Nann, T., *Shape Control of II–VI Semiconductor Nanomaterials*. *Small* **2006,** 2, 316.

104.   Burda, C.; Chen, X.; Narayanan, R.; El-Sayed, M. A., *Chemistry and Properties of Nanocrystals of Different Shapes*. *Chem. Rev.* **2005,** 105, 1025.

105.   De Smet, Y.; Deriemaeker, L.; Finsy, R., *A Simple Computer Simulation of Ostwald Ripening*. *Langmuir* **1997,** 13, 6884.

106.   Talapin, D. V.; Rogach, A. L.; Haase, M.; Weller, H., *Evolution of an Ensemble of Nanoparticles in a Colloidal Solution: Theoretical Study*. *J. Phys. Chem. B* **2001,** 105, 12278.

107.   Tagliazucchi, M.; Tice, D. B.; Sweeney, C. M.; Morris-Cohen, A. J.; Weiss, E. A., *Ligand-Controlled Rates of Photoinduced Electron Transfer in Hybrid CdSe Nanocrystal/Poly(viologen) Films*. *ACS Nano* **2011,** 5, 9907.

108.   Sambur, J. B.; Riha, S. C.; Choi, D.; Parkinson, B. A., *Influence of Surface Chemistry on the Binding and Electronic Coupling of CdSe Quantum Dots to Single Crystal TiO2 Surfaces*. *Langmuir* **2010,** 26, 4839.

109.   King, L. A.; Riley, D. J., *Importance of QD Purification Procedure on Surface Adsorbance of QDs and Performance of QD Sensitized Photoanodes*. *J. Phys. Chem. C* **2012,** 116, 3349.

110.   Kalyuzhny, G.; Murray, R. W., *Ligand Effects on Optical Properties of CdSe Nanocrystals*. *J. Phys. Chem. B* **2005,** 109, 7012.

111.   Shen, Y.; Gee, M. Y.; Tan, R.; Pellechia, P. J.; Greytak, A. B., *Purification of Quantum Dots by Gel Permeation Chromatography and the Effect of Excess Ligands on Shell Growth and Ligand Exchange*. *Chem. Mater.* **2013,** 25, 2838.

112.   Shen, Y.; Tan, R.; Gee, M. Y.; Greytak, A. B., *Quantum Yield Regeneration: Influence of Neutral Ligand Binding on Photophysical Properties in Colloidal Core/Shell Quantum Dots*. *ACS Nano* **2015,** 9, 3345.

113.   Huang, J.; Kovalenko, M. V.; Talapin, D. V., *Alkyl Chains of Surface Ligands Affect Polytypism of CdSe Nanocrystals and Play an Important Role in the Synthesis of Anisotropic Nanoheterostructures*. *J. Am. Chem. Soc.* **2010,** 132, 15866.

114.   Yin, Y.; Alivisatos, A. P., *Colloidal Nanocrystal Synthesis and the Organic–Inorganic Interface*. *Nature* **2005,** 437, 664.

115.   García-Rodríguez, R.; Hendricks, M. P.; Cossairt, B. M.; Liu, H.; Owen, J. S., *Conversion Reactions of Cadmium Chalcogenide Nanocrystal Precursors*. *Chem. Mater.* **2013,** 25, 1233.

116.   Van Embden, J.; Mulvaney, P., *Nucleation and Growth of CdSe Nanocrystals in a Binary Ligand System*. *Langmuir* **2005,** 21, 10226.

117.   Manna, L.; Scher, E. C.; Alivisatos, A. P., *Synthesis of Soluble and Processable Rod-, Arrow-, Teardrop-, and Tetrapod-Shaped CdSe Nanocrystals*. *J. Am. Chem. Soc.* **2000,** 122, 12700.

118.   Qu, L.; Peng, X., *Control of Photoluminescence Properties of CdSe Nanocrystals in Growth*. *J. Am. Chem. Soc.* **2002,** 124, 2049.

119.   Klem, E. J. D.; MacNeil, D. D.; Cyr, P. W.; Levina, L.; Sargent, E. H., *Efficient Solution-Processed Infrared Photovoltaic Cells: Planarized All-Inorganic Bulk Heterojunction Devices via Inter-Quantum-Dot Bridging during Growth from Solution*. *Appl. Phys. Lett.* **2007,** 90, 183113.

120.   Diedenhofen, S. L.; Kufer, D.; Lasanta, T.; Konstantatos, G., *Integrated Colloidal Quantum Dot Photodetectors with Color-Tunable Plasmonic Nanofocusing Lenses*. *Light Sci. Appl.* **2015,** 4, e234.

121.   Huynh, W. U.; Dittmer, J. J.; Alivisatos, A. P., *Hybrid Nanorod-Polymer Solar Cells*. *Science* **2002,** 295, 2425.

122.   Li, Q.; Sun, B.; Kinloch, I. A.; Zhi, D.; Sirringhaus, H.; Windle, A. H., *Enhanced Self-Assembly of Pyridine-Capped CdSe Nanocrystals on Individual Single-Walled Carbon Nanotubes*. *Chem. Mater.* **2006,** 18, 164.

123. Zhang, C.; O'Brien, S.; Balogh, L., *Comparison and Stability of CdSe Nanocrystals Covered with Amphiphilic Poly(amidoamine) Dendrimers*. *J. Phys. Chem. B* **2002,** 106, 10316.

124. Liu, Y.; Gibbs, M.; Puthussery, J.; Gaik, S.; Ihly, R.; Hillhouse, H. W.; Law, M., *Dependence of Carrier Mobility on Nanocrystal Size and Ligand Length in PbSe Nanocrystal Solids*. *Nano Lett.* **2010,** 10, 1960.

125. Talgorn, E.; Moysidou, E.; Abellon, R. D.; Savenije, T. J.; Goossens, A.; Houtepen, A. J.; Siebbeles, L. D. A., *Highly Photoconductive CdSe Quantum-Dot Films: Influence of Capping Molecules and Film Preparation Procedure*. *J. Phys. Chem. C* **2010,** 114, 3441.

126. Sun, L.; Choi, J. J.; Stachnik, D.; Bartnik, A. C.; Hyun, B. R.; Malliaras, G. G.; Hanrath, T.; Wise, F. W., *Bright Infrared Quantum-Dot Light-Emitting Diodes through Inter-Dot Spacing Control*. *Nat. Nanotechnol.* **2012,** 7, 369.

127. Remacle, F., *On Electronic Properties of Assemblies of Quantum Nanodots*. *The Journal of Physical Chemistry A* **2000,** 104, 4739-4747.

128. Kovalenko, M. V.; Scheele, M.; Talapin, D. V., *Colloidal Nanocrystals with Molecular Metal Chalcogenide Surface Ligands*. *Science* **2009,** 324, 1417.

129. Jang, J.; Liu, W.; Son, J. S.; Talapin, D. V., *Temperature-Dependent Hall and Field-Effect Mobility in Strongly Coupled All-Inorganic Nanocrystal Arrays*. *Nano Lett.* **2014,** 14, 653.

130. Lee, J. S.; Kovalenko, M. V.; Huang, J.; Chung, D. S.; Talapin, D. V., *Band-like Transport, High Electron Mobility and High Photoconductivity in All-Inorganic Nanocrystal Arrays*. *Nat. Nanotechnol.* **2011,** 6, 348.

131. Liu, W.; Lee, J. S.; Talapin, D. V., *III–V Nanocrystals Capped with Molecular Metal Chalcogenide Ligands: High Electron Mobility and Ambipolar Photoresponse*. *J. Am. Chem. Soc.* **2012,** 135, 1349.

132. Kovalenko, M. V.; Schaller, R. D.; Jarzab, D.; Loi, M. A.; Talapin, D. V., *Inorganically Functionalized PbS–CdS Colloidal Nanocrystals: Integration into Amorphous Chalcogenide Glass and Luminescent Properties*. *J. Am. Chem. Soc.* **2012,** 134, 2457.

133. Jiang, C.; Lee, J. S.; Talapin, D. V., *Soluble Precursors for CuInSe2, CuIn1–xGaxSe2, and Cu2ZnSn(S,Se)4 Based on Colloidal Nanocrystals and Molecular Metal Chalcogenide Surface Ligands*. *J. Am. Chem. Soc.* **2012,** 134, 5010.

134. Baumgardner, W. J.; Whitham, K.; Hanrath, T., *Confined-but-connected quantum solids via controlled ligand displacement*. *Nano letters* **2013,** 13, 3225-3231.

135. Tang, J.; Kemp, K. W.; Hoogland, S.; Jeong, K. S.; Liu, H.; Levina, L.; Furukawa, M.; Wang, X.; Debnath, R.; Cha, D., *Colloidal-Quantum-Dot Photovoltaics Using Atomic-Ligand Passivation*. *Nat. Mater.* **2011,** 10, 765.

136. Anderson, N. C.; Owen, J. S., *Soluble, Chloride-Terminated CdSe Nanocrystals: Ligand Exchange Monitored by 1H and 31P NMR Spectroscopy*. *Chem. Mater.* **2012,** 25, 69.

137. Greaney, M. J.; Couderc, E.; Zhao, J.; Nail, B. A.; Mecklenburg, M.; Thornbury, W.; Osterloh, F. E.; Bradforth, S. E.; Brutchey, R. L., *Controlling the Trap State Landscape of Colloidal CdSe Nanocrystals with Cadmium Halide Ligands*. *Chem. Mater.* **2015,** 27, 744.

138. Ning, Z.; Ren, Y.; Hoogland, S.; Voznyy, O.; Levina, L.; Stadler, P.; Lan, X.; Zhitomirsky, D.; Sargent, E. H., *All-Inorganic Colloidal Quantum Dot Photovoltaics Employing Solution-Phase Halide Passivation*. *Adv. Mater.* **2012,** 24, 6295.

139. Zhang, J.; Gao, J.; Miller, E. M.; Luther, J. M.; Beard, M. C., *Diffusion-Controlled Synthesis of PbS and PbSe Quantum Dots with in Situ Halide Passivation for Quantum Dot Solar Cells*. *ACS Nano* **2013,** 8, 614.

140. Dirin, D. N.; Dreyfuss, S.; Bodnarchuk, M. I.; Nedelcu, G.; Papagiorgis, P.; Itskos, G.; Kovalenko, M. V., *Lead Halide Perovskites and Other Metal Halide Complexes as Inorganic Capping Ligands for Colloidal Nanocrystals*. *J. Am. Chem. Soc.* **2014,** 136, 6550.

141. Zhang, H.; Jang, J.; Liu, W.; Talapin, D. V., *Colloidal Nanocrystals with Inorganic Halide, Pseudohalide, and Halometallate Ligands*. *ACS Nano* **2014,** 8, 7359.

142.	Zhang, X.; Zhang, J.; Phuyal, D.; Du, J.; Tian, L.; Öberg, V. A.; Johansson, M. B.; Cappel, U. B.; Karis, O.; Liu, J., et al., *Inorganic CsPbI3 Perovskite Coating on PbS Quantum Dot for Highly Efficient and Stable Infrared Light Converting Solar Cells*. *Advanced Energy Materials* **2018,** 8, 1702049.

143.	Ip, A. H.; Thon, S. M.; Hoogland, S.; Voznyy, O.; Zhitomirsky, D.; Debnath, R.; Levina, L.; Rollny, L. R.; Carey, G. H.; Fischer, A., *Hybrid Passivated Colloidal Quantum Dot Solids*. *Nat. Nanotechnol.* **2012,** 7, 577.

144.	Ning, Z.; Voznyy, O.; Pan, J.; Hoogland, S.; Adinolfi, V.; Xu, J.; Li, M.; Kirmani, A. R.; Sun, J. P.; Minor, J., *Air-Stable n-Type Colloidal Quantum Dot Solids*. *Nat. Mater.* **2014,** 13, 822.

145.	Carey, G. H.; Levina, L.; Comin, R.; Voznyy, O.; Sargent, E. H., *Record Charge Carrier Diffusion Length in Colloidal Quantum Dot Solids via Mutual Dot-to-Dot Surface Passivation*. *Adv. Mater.* **2015,** 27, 3325.

146.	Milliron, D. J., *The surface plays a core role*. *Nature Materials* **2014,** 13, 772.

147.	Ning, Z.; Voznyy, O.; Pan, J.; Hoogland, S.; Adinolfi, V.; Xu, J.; Li, M.; Kirmani, A. R.; Sun, J. P.; Minor, J., et al., *Air-stable n-type colloidal quantum dot solids*. *Nat Mater* **2014,** 13, 822-828.

148.	Zhitomirsky, D.; Furukawa, M.; Tang, J.; Stadler, P.; Hoogland, S.; Voznyy, O.; Liu, H.; Sargent, E. H., *N-Type Colloidal-Quantum-Dot Solids for Photovoltaics*. *Advanced Materials* **2012,** 24, 6181-6185.

149.	Ning, Z.; Dong, H.; Zhang, Q.; Voznyy, O.; Sargent, E. H., *Solar cells based on inks of n-type colloidal quantum dots*. *ACS nano* **2014,** 8, 10321-10327.

150.	Brown, P. R.; Kim, D.; Lunt, R. R.; Zhao, N.; Bawendi, M. G.; Grossman, J. C.; Bulović, V., *Energy level modification in lead sulfide quantum dot thin films through ligand exchange*. *ACS nano* **2014,** 8, 5863-5872.

151.	Katsiev, K.; Ip, A. H.; Fischer, A.; Tanabe, I.; Zhang, X.; Kirmani, A. R.; Voznyy, O.; Rollny, L. R.; Chou, K. W.; Thon, S. M., et al., *The Complete In-Gap Electronic Structure of Colloidal Quantum Dot Solids and Its Correlation with Electronic Transport and Photovoltaic Performance*. *Advanced Materials* **2014,** 26, 937-942.

152.	Chuang, C. H. M.; Brown, P. R.; Bulović, V.; Bawendi, M. G., *Improved Performance and Stability in Quantum Dot Solar Cells through Band Alignment Engineering*. *Nat. Mater.* **2014,** 13, 796-801.

153.	Luther, J. M.; Law, M.; Song, Q.; Perkins, C. L.; Beard, M. C.; Nozik, A. J., *Structural, Optical, and Electrical Properties of Self-Assembled Films of PbSe Nanocrystals Treated with 1,2-Ethanedithiol*. *ACS Nano* **2008,** 2, 271-280.

154.	Koleilat, G. I.; Levina, L.; Shukla, H.; Myrskog, S. H.; Hinds, S.; Pattantyus-Abraham, A. G.; Sargent, E. H., *Efficient, Stable Infrared Photovoltaics Based on Solution-Cast Colloidal Quantum Dots*. *ACS Nano* **2008,** 2, 833-840.

155.	Pattantyus-Abraham, A. G.; Kramer, I. J.; Barkhouse, A. R.; Wang, X.; Konstantatos, G.; Debnath, R.; Levina, L.; Raabe, I.; Nazeeruddin, M. K.; Grätzel, M., *Depleted-Heterojunction Colloidal Quantum Dot Solar Cells*. *ACS Nano* **2010,** 4, 3374.

156.	Wang, R.; Shang, Y.; Kanjanaboos, P.; Zhou, W.; Ning, Z.; Sargent, E. H., *Colloidal quantum dot ligand engineering for high performance solar cells*. *Energy & Environmental Science* **2016,** 9, 1130-1143.

157.	Xu, J.; Voznyy, O.; Liu, M.; Kirmani, A. R.; Walters, G.; Munir, R.; Abdelsamie, M.; Proppe, A. H.; Sarkar, A.; García de Arquer, F. P., et al., *2D matrix engineering for homogeneous quantum dot coupling in photovoltaic solids*. *Nature Nanotechnology* **2018,** 13, 456-462.

158.	Gai, Y.; Peng, H.; Li, J., *Electronic Properties of Nonstoichiometric PbSe Quantum Dots from First Principles*. *The Journal of Physical Chemistry C* **2009,** 113, 21506-21511.

159.	Smith, D. K.; Luther, J. M.; Semonin, O. E.; Nozik, A. J.; Beard, M. C., *Tuning the Synthesis of Ternary Lead Chalcogenide Quantum Dots by Balancing Precursor Reactivity*. *ACS Nano* **2011,** 5, 183-190.

160.   Moreels, I.; Lambert, K.; De Muynck, D.; Vanhaecke, F.; Poelman, D.; Martins, J. C.; Allan, G.; Hens, Z., *Composition and Size-Dependent Extinction Coefficient of Colloidal PbSe Quantum Dots*. *Chemistry of Materials* **2007,** 19, 6101-6106.

161.   Hwang, G. W.; Kim, D.; Cordero, J. M.; Wilson, M. W. B.; Chuang, C.-H. M.; Grossman, J. C.; Bawendi, M. G., *Identifying and Eliminating Emissive Sub-bandgap States in Thin Films of PbS Nanocrystals*. *Advanced Materials* **2015,** 27, 4481-4486.

162.   Bozyigit, D.; Volk, S.; Yarema, O.; Wood, V., *Quantification of Deep Traps in Nanocrystal Solids, Their Electronic Properties, and Their Influence on Device Behavior*. *Nano Letters* **2013,** 13, 5284-5288.

163.   Yoon, W.; Boercker, J. E.; Lumb, M. P.; Placencia, D.; Foos, E. E.; Tischler, J. G., *Enhanced open-circuit voltage of PbS nanocrystal quantum dot solar cells*. *Scientific reports* **2013,** 3, 2225.

164.   Zhitomirsky, D.; Voznyy, O.; Hoogland, S.; Sargent, E. H., *Measuring Charge Carrier Diffusion in Coupled Colloidal Quantum Dot Solids*. *ACS Nano* **2013,** 7, 5282.

165.   Nagpal, P.; Klimov, V. I., *Role of mid-gap states in charge transport and photoconductivity in semiconductor nanocrystal films*. **2011,** 2, 486.

166.   Tang, J.; Kemp, K. W.; Hoogland, S.; Jeong, K. S.; Liu, H.; Levina, L.; Furukawa, M.; Wang, X.; Debnath, R.; Cha, D., *Colloidal-quantum-dot photovoltaics using atomic-ligand passivation*. *Nature materials* **2011,** 10, 765.

167.   Oh, S. J.; Berry, N. E.; Choi, J.-H.; Gaulding, E. A.; Paik, T.; Hong, S.-H.; Murray, C. B.; Kagan, C. R., *Stoichiometric control of lead chalcogenide nanocrystal solids to enhance their electronic and optoelectronic device performance*. *ACS nano* **2013,** 7, 2413-2421.

168.   Ip, A. H.; Thon, S. M.; Hoogland, S.; Voznyy, O.; Zhitomirsky, D.; Debnath, R.; Levina, L.; Rollny, L. R.; Carey, G. H.; Fischer, A., *Hybrid passivated colloidal quantum dot solids*. *Nature nanotechnology* **2012,** 7, 577.

169.   McDaniel, H.; Fuke, N.; Makarov, N. S.; Pietryga, J. M.; Klimov, V. I., *An integrated approach to realizing high-performance liquid-junction quantum dot sensitized solar cells*. *Nature communications* **2013,** 4, 2887.

170.   McDaniel, H.; Fuke, N.; Pietryga, J. M.; Klimov, V. I. In *Engineered CuInSexS2-x quantum dots for high efficiency sensitized solar cells*, ABSTRACTS OF PAPERS OF THE AMERICAN CHEMICAL SOCIETY, 2013; AMER CHEMICAL SOC 1155 16TH ST, NW, WASHINGTON, DC 20036 USA.

171.   Goodwin, E. D.; Straus, D. B.; Gaulding, E. A.; Murray, C. B.; Kagan, C. R., *The effects of inorganic surface treatments on photogenerated carrier mobility and lifetime in PbSe quantum dot thin films*. *Chemical Physics* **2016,** 471, 81-88.

172.   Lan, X.; Voznyy, O.; Kiani, A.; García de Arquer, F. P.; Abbas, A. S.; Kim, G.-H.; Liu, M.; Yang, Z.; Walters, G.; Xu, J., et al., *Passivation Using Molecular Halides Increases Quantum Dot Solar Cell Performance*. *Advanced Materials* **2016,** 28, 299-304.

173.   Ip, A. H.; Thon, S. M.; Hoogland, S.; Voznyy, O.; Zhitomirsky, D.; Debnath, R.; Levina, L.; Rollny, L. R.; Carey, G. H.; Fischer, A., et al., *Hybrid passivated colloidal quantum dot solids*. *Nat Nano* **2012,** 7, 577-582.

174.   Thon, S. M.; Ip, A. H.; Voznyy, O.; Levina, L.; Kemp, K. W.; Carey, G. H.; Masala, S.; Sargent, E. H., *Role of Bond Adaptability in the Passivation of Colloidal Quantum Dot Solids*. *ACS Nano* **2013,** 7, 7680-7688.

175.   Tang, J.; Kemp, K. W.; Hoogland, S.; Jeong, K. S.; Liu, H.; Levina, L.; Furukawa, M.; Wang, X.; Debnath, R.; Cha, D., et al., *Colloidal-quantum-dot photovoltaics using atomic-ligand passivation*. *Nat Mater* **2011,** 10, 765-771.

176.   McDonald, S. A.; Konstantatos, G.; Zhang, S.; Cyr, P. W.; Klem, E. J. D.; Levina, L.; Sargent, E. H., *Solution-Processed PbS Quantum Dot Infrared Photodetectors and Photovoltaics*. *Nat. Mater.* **2005,** 4, 138.

177.   Maria, A.; Cyr, P. W.; Klem, E. J. D.; Levina, L.; Sargent, E. H., *Solution-Processed Infrared Photovoltaic Devices with >10% Monochromatic Internal Quantum Efficiency*. *Appl. Phys. Lett.* **2005,** 87, 213112.

178.   Clifford, J. P.; Johnston, K. W.; Levina, L.; Sargent, E. H., *Schottky Barriers to Colloidal Quantum Dot Films*. *Appl. Phys. Lett.* **2007,** 91, 253117.

179.   Luther, J. M.; Law, M.; Beard, M. C.; Song, Q.; Reese, M. O.; Ellingson, R. J.; Nozik, A. J., *Schottky Solar Cells Based on Colloidal Nanocrystal Films*. *Nano Lett.* **2008,** 8, 3488.

180.   Koleilat, G. I.; Levina, L.; Shukla, H.; Myrskog, S. H.; Hinds, S.; Pattantyus-Abraham, A. G.; Sargent, E. H., *Efficient, Stable Infrared Photovoltaics Based on Solution-Cast Colloidal Quantum Dots*. *ACS Nano* **2008,** 2, 833.

181.   Tang, J.; Wang, X.; Brzozowski, L.; Barkhouse, D. A. R.; Debnath, R.; Levina, L.; Sargent, E. H., *Schottky Quantum Dot Solar Cells Stable in Air under Solar Illumination*. *Adv. Mater.* **2010,** 22, 1398.

182.   Choi, M. J.; Oh, J.; Yoo, J. K.; Choi, J.; Sim, D. M.; Jung, Y. S., *Tailoring of the PbS/Metal Interface in Colloidal Quantum Dot Solar Cells for Improvements of Performance and Air Stability*. *Energy Environ. Sci.* **2014,** 7, 3052.

183.   Zhao, N.; Osedach, T. P.; Chang, L. Y.; Geyer, S. M.; Wanger, D.; Binda, M. T.; Arango, A. C.; Bawendi, M. G.; Bulovic, V., *Colloidal PbS Quantum Dot Solar Cells with High Fill Factor*. *ACS Nano* **2010,** 4, 3743.

184.   Piliego, C.; Protesescu, L.; Bisri, S. Z.; Kovalenko, M. V.; Loi, M. A., *5.2% Efficient PbS Nanocrystal Schottky Solar Cells*. *Energy Environ. Sci.* **2013,** 6, 3054.

185.   Henry, C. H., *Limiting Efficiencies of Ideal Single and Multiple Energy Gap Terrestrial Solar Cells*. *J. Appl. Phys.* **1980,** 51, 4494.

186.   Luther, J. M.; Gao, J.; Lloyd, M. T.; Semonin, O. E.; Beard, M. C.; Nozik, A. J., *Stability Assessment on a 3% Bilayer PbS/ZnO Quantum Dot Heterojunction Solar Cell*. *Adv. Mater.* **2010,** 22, 3704.

187.   Tang, J.; Liu, H.; Zhitomirsky, D.; Hoogland, S.; Wang, X.; Furukawa, M.; Levina, L.; Sargent, E. H., *Quantum Junction Solar Cells*. *Nano Lett.* **2012,** 12, 4889.

188.   Liu, M.; de Arquer, F. P. G.; Li, Y.; Lan, X.; Kim, G.-H.; Voznyy, O.; Jagadamma, L. K.; Abbas, A. S.; Hoogland, S.; Lu, Z., et al., *Double-Sided Junctions Enable High-Performance Colloidal-Quantum-Dot Photovoltaics*. *Advanced Materials* **2016,** 28, 4142-4148.

189.   Lan, X.; Voznyy, O.; García de Arquer, F. P.; Liu, M.; Xu, J.; Proppe, A. H.; Walters, G.; Fan, F.; Tan, H.; Liu, M., et al., *10.6% Certified Colloidal Quantum Dot Solar Cells via Solvent-Polarity-Engineered Halide Passivation*. *Nano Letters* **2016,** 16, 4630-4634.

190.   Stavrinadis, A.; Pradhan, S.; Papagiorgis, P.; Itskos, G.; Konstantatos, G., *Suppressing Deep Traps in PbS Colloidal Quantum Dots via Facile Iodide Substitutional Doping for Solar Cells with Efficiency >10%*. *ACS Energy Letters* **2017,** 2, 739-744.

191.   Liu, M.; Voznyy, O.; Sabatini, R.; Garcia de Arquer, F. P.; Munir, R.; Balawi, A. H.; Lan, X.; Fan, F.; Walters, G.; Kirmani, A. R., et al., *Hybrid organic-inorganic inks flatten the energy landscape in colloidal quantum dot solids*. *Nat Mater* **2017,** 16, 258-263.

192.   Yuan, M.; Zhitomirsky, D.; Adinolfi, V.; Voznyy, O.; Kemp, K. W.; Ning, Z.; Lan, X.; Xu, J.; Kim, J. Y.; Dong, H., *Doping Control via Molecularly Engineered Surface Ligand Coordination*. *Adv. Mater.* **2013,** 25, 5586.

193.   Ko, D. K.; Brown, P. R.; Bawendi, M. G.; Bulović, V., *p-i-n Heterojunction Solar Cells with a Colloidal Quantum-Dot Absorber Layer*. *Adv. Mater.* **2014,** 26, 4845.

194.   Tikhomirov, G.; Hoogland, S.; Lee, P. E.; Fischer, A.; Sargent, E. H.; Kelley, S. O., *DNA-Based Programming of Quantum Dot Valency, Self-Assembly and Luminescence*. *Nat. Nanotechnol.* **2011,** 6, 485.

195.   Kramer, I. J.; Levina, L.; Debnath, R.; Zhitomirsky, D.; Sargent, E. H., *Solar Cells Using Quantum Funnels*. *Nano Lett.* **2011,** 11, 3701.

196.   Adinolfi, V.; Ning, Z.; Xu, J.; Masala, S.; Zhitomirsky, D.; Thon, S. M.; Sargent, E. H., *Electric Field Engineering Using Quantum-Size-Effect-Tuned Heterojunctions*. *Appl. Phys. Lett.* **2013,** 103, 011106.

197.   Wang, R.; Wu, X.; Xu, K.; Zhou, W.; Shang, Y.; Tang, H.; Chen, H.; Ning, Z., *Highly Efficient Inverted Structural Quantum Dot Solar Cells*. *Advanced Materials* **2018,** 30, 1704882.

198. Lu, K.; Wang, Y.; Yuan, J.; Cui, Z.; Shi, G.; Shi, S.; Han, L.; Chen, S.; Zhang, Y.; Ling, X., *Efficient PbS quantum dot solar cells employing a conventional structure*. *Journal of Materials Chemistry A* **2017,** 5, 23960-23966.

199. Aqoma, H.; Jang, S.-Y., *Solid-state-ligand-exchange free quantum dot ink-based solar cells with an efficiency of 10.9%*. *Energy & Environmental Science* **2018,** 11, 1603-1609.

200. Hu, L.; Zhang, Z.; Patterson, R. J.; Hu, Y.; Chen, W.; Chen, C.; Li, D.; Hu, C.; Ge, C.; Chen, Z., et al., *Achieving high-performance PbS quantum dot solar cells by improving hole extraction through Ag doping*. *Nano Energy* **2018,** 46, 212-219.

201. Kemp, K. W.; Labelle, A. J.; Thon, S. M.; Ip, A. H.; Kramer, I. J.; Hoogland, S.; Sargent, E. H., *Interface Recombination in Depleted Heterojunction Photovoltaics Based on Colloidal Quantum Dots*. *Adv. Energy Mater.* **2013,** 3, 917.

202. Yuan, M.; Voznyy, O.; Zhitomirsky, D.; Kanjanaboos, P.; Sargent, E. H., *Synergistic Doping of Fullerene Electron Transport Layer and Colloidal Quantum Dot Solids Enhances Solar Cell Performance*. *Adv. Mater.* **2015,** 27, 917.

203. Ehrler, B.; Musselman, K. P.; Böhm, M. L.; Morgenstern, F. S. F.; Vaynzof, Y.; Walker, B. J.; MacManus-Driscoll, J. L.; Greenham, N. C., *Preventing Interfacial Recombination in Colloidal Quantum Dot Solar Cells by Doping the Metal Oxide*. *ACS Nano* **2013,** 7, 4210.

204. Cao, Y.; Stavrinadis, A.; Lasanta, T.; So, D.; Konstantatos, G., *The role of surface passivation for efficient and photostable PbS quantum dot solar cells*. *Nature Energy* **2016,** 1, 16035.

205. Cao, Y.; Stavrinadis, A.; Lasanta, T.; So, D.; Konstantatos, G., *The Role of Surface Passivation for Efficient and Photostable PbS Quantum Dot Solar Cells*. *Nat. Energy* **2016,** 1, 16035.

206. Beard, M. C.; Luther, J. M.; Semonin, O. E.; Nozik, A. J., *Third Generation Photovoltaics based on Multiple Exciton Generation in Quantum Confined Semiconductors*. *Accounts of Chemical Research* **2013,** 46, 1252-1260.

207. Padilha, L. A.; Stewart, J. T.; Sandberg, R. L.; Bae, W. K.; Koh, W.-K.; Pietryga, J. M.; Klimov, V. I., *Carrier Multiplication in Semiconductor Nanocrystals: Influence of Size, Shape, and Composition*. *Accounts of Chemical Research* **2013,** 46, 1261-1269.

208. Davis, N. J. L. K.; Böhm, M. L.; Tabachnyk, M.; Wisnivesky-Rocca-Rivarola, F.; Jellicoe, T. C.; Ducati, C.; Ehrler, B.; Greenham, N. C., *Multiple-exciton generation in lead selenide nanorod solar cells with external quantum efficiencies exceeding 120%*. **2015,** 6, 8259.

209. Zhang, Z.; Chen, Z.; Zhang, J.; Chen, W.; Yang, J.; Wen, X.; Wang, B.; Kobamoto, N.; Yuan, L.; Stride, J. A., et al., *Significant Improvement in the Performance of PbSe Quantum Dot Solar Cell by Introducing a CsPbBr3 Perovskite Colloidal Nanocrystal Back Layer*. *Advanced Energy Materials* **2017,** 7, 1601773-n/a.

210. Hu, L.; Zhang, Z.; Patterson, R. J.; Shivarudraiah, S. B.; Zhou, Z.; Ng, M.; Huang, S.; Halpert, J. E., *PbSe Quantum Dot Passivated Via Mixed Halide Perovskite Nanocrystals for Solar Cells With Over 9% Efficiency*. *Solar RRL* **2018,** 2, 1800234.

211. Kim, S.; Marshall, A. R.; Kroupa, D. M.; Miller, E. M.; Luther, J. M.; Jeong, S.; Beard, M. C., *Air-Stable and Efficient PbSe Quantum-Dot Solar Cells Based upon ZnSe to PbSe Cation-Exchanged Quantum Dots*. *ACS Nano* **2015,** 9, 8157-8164.

212. Yanover, D.; Vaxenburg, R.; Tilchin, J.; Rubin-Brusilovski, A.; Zaiats, G.; Čapek, R. K.; Sashchiuk, A.; Lifshitz, E., *Significance of Small-Sized PbSe/PbS Core/Shell Colloidal Quantum Dots for Optoelectronic Applications*. *The Journal of Physical Chemistry C* **2014,** 118, 17001-17009.

213. Hu, L.; Geng, X.; Singh, S.; Shi, J.; Hu, Y.; Li, S.; Guan, X.; He, T.; Li, X.; Cheng, Z., et al., *Synergistic effect of electron transport layer and colloidal quantum dot solid enable PbSe quantum dot solar cell achieving over 10 % efficiency*. *Nano Energy* **2019,** 64, 103922.

214. Gur, I.; Fromer, N. A.; Geier, M. L.; Alivisatos, A. P., *Air-Stable All-Inorganic Nanocrystal Solar Cells Processed from Solution*. *Science* **2005,** 310, 462-465.

215. Jasieniak, J.; MacDonald, B. I.; Watkins, S. E.; Mulvaney, P., *Solution-Processed Sintered Nanocrystal Solar Cells via Layer-by-Layer Assembly*. *Nano Letters* **2011,** 11, 2856-2864.

216.   Panthani, M. G.; Kurley, J. M.; Crisp, R. W.; Dietz, T. C.; Ezzyat, T.; Luther, J. M.; Talapin, D. V., *High Efficiency Solution Processed Sintered CdTe Nanocrystal Solar Cells: The Role of Interfaces*. *Nano Letters* **2014,** 14, 670-675.

217.   Crisp, R. W.; Panthani, M. G.; Rance, W. L.; Duenow, J. N.; Parilla, P. A.; Callahan, R.; Dabney, M. S.; Berry, J. J.; Talapin, D. V.; Luther, J. M., *Nanocrystal Grain Growth and Device Architectures for High-Efficiency CdTe Ink-Based Photovoltaics*. *ACS Nano* **2014,** 8, 9063-9072.

218.   Townsend, T. K.; Heuer, W. B.; Foos, E. E.; Kowalski, E.; Yoon, W.; Tischler, J. G., *Safer salts for CdTe nanocrystal solution processed solar cells: the dual roles of ligand exchange and grain growth*. *Journal of Materials Chemistry A* **2015,** 3, 13057-13065.

219.   Zhang, H.; Kurley, J. M.; Russell, J. C.; Jang, J.; Talapin, D. V., *Solution-Processed, Ultrathin Solar Cells from CdCl3—Capped CdTe Nanocrystals: The Multiple Roles of CdCl3— Ligands*. *Journal of the American Chemical Society* **2016,** 138, 7464-7467.

220.   Kojima, A.; Teshima, K.; Shirai, Y.; Miyasaka, T., *Organometal Halide Perovskites as Visible-Light Sensitizers for Photovoltaic Cells*. *Journal of the American Chemical Society* **2009,** 131, 6050-6051.

221.   Nenon, D. P.; Christians, J. A.; Wheeler, L. M.; Blackburn, J. L.; Sanehira, E. M.; Dou, B.; Olsen, M. L.; Zhu, K.; Berry, J. J.; Luther, J. M., *Structural and chemical evolution of methylammonium lead halide perovskites during thermal processing from solution*. *Energy & Environmental Science* **2016,** 9, 2072-2082.

222.   Beal, R. E.; Slotcavage, D. J.; Leijtens, T.; Bowring, A. R.; Belisle, R. A.; Nguyen, W. H.; Burkhard, G. F.; Hoke, E. T.; McGehee, M. D., *Cesium Lead Halide Perovskites with Improved Stability for Tandem Solar Cells*. *The Journal of Physical Chemistry Letters* **2016,** 7, 746-751.

223.   Swarnkar, A.; Marshall, A. R.; Sanehira, E. M.; Chernomordik, B. D.; Moore, D. T.; Christians, J. A.; Chakrabarti, T.; Luther, J. M., *Quantum dot–induced phase stabilization of α-CsPbI$_3$ perovskite for high-efficiency photovoltaics*. *Science* **2016,** 354, 92-95.

224.   Sanehira, E. M.; Marshall, A. R.; Christians, J. A.; Harvey, S. P.; Ciesielski, P. N.; Wheeler, L. M.; Schulz, P.; Lin, L. Y.; Beard, M. C.; Luther, J. M., *Enhanced mobility CsPbI$_3$ quantum dot arrays for record-efficiency, high-voltage photovoltaic cells*. *Science Advances* **2017,** 3, eaao4204.

225.   Major, J. D.; Treharne, R. E.; Phillips, L. J.; Durose, K., *A low-cost non-toxic post-growth activation step for CdTe solar cells*. *Nature* **2014,** 511, 334-337.

226.   Reinhard, P.; Chirilă, A.; Blösch, P.; Pianezzi, F.; Nishiwaki, S.; Buecheler, S.; Tiwari, A. N., *Review of Progress Toward 20% Efficiency Flexible CIGS Solar Cells and Manufacturing Issues of Solar Modules*. *IEEE Journal of Photovoltaics* **2013,** 3, 572-580.

227.   Romanyuk, Y. E.; Hagendorfer, H.; Stücheli, P.; Fuchs, P.; Uhl, A. R.; Sutter-Fella, C. M.; Werner, M.; Haass, S.; Stückelberger, J.; Broussillou, C., et al., *All Solution-Processed Chalcogenide Solar Cells – from Single Functional Layers Towards a 13.8% Efficient CIGS Device*. *Advanced Functional Materials* **2015,** 25, 12-27.

228.   Santra, P. K.; Nair, P. V.; George Thomas, K.; Kamat, P. V., *CuInS2-sensitized quantum dot solar cell. Electrophoretic deposition, excited-state dynamics, and photovoltaic performance*. *The journal of physical chemistry letters* **2013,** 4, 722-729.

229.   Bernechea, M.; Miller, N. C.; Xercavins, G.; So, D.; Stavrinadis, A.; Konstantatos, G., *Solution-processed solar cells based on environmentally friendly AgBiS2 nanocrystals*. *Nat Photon* **2016,** 10, 521-525.

230.   Hirst, L. C.; Ekins‐Daukes, N. J., *Fundamental losses in solar cells*. *Progress in Photovoltaics: Research and Applications* **2011,** 19, 286-293.

231.   Shockley, W.; Queisser, H. J., *Detailed Balance Limit of Efficiency of p-n Junction Solar Cells*. *J. Appl. Phys.* **2004,** 32, 510.

232.   Leijtens, T.; Bush, K. A.; Prasanna, R.; McGehee, M. D., *Opportunities and challenges for tandem solar cells using metal halide perovskite semiconductors*. *Nature Energy* **2018,** 3, 828-838.

233.   Philipps, S. P.; Bett, A. W., *III-V Multi-junction solar cells and concentrating photovoltaic (CPV) systems*. *Advanced Optical Technologies* **2014,** 3, 469-478.

234.   Futscher, M. H.; Ehrler, B., *Modeling the Performance Limitations and Prospects of Perovskite/Si Tandem Solar Cells under Realistic Operating Conditions*. ACS Energy Letters **2017,** 2, 2089-2095.

235.   Yu, Z.; Leilaeioun, M.; Holman, Z., *Selecting tandem partners for silicon solar cells*. Nat. Energy **2016,** 1, 16137.

236.   Zheng, J.; Lau, C. F. J.; Mehrvarz, H.; Ma, F.-J.; Jiang, Y.; Deng, X.; Soeriyadi, A.; Kim, J.; Zhang, M.; Hu, L., et al., *Large area efficient interface layer free monolithic perovskite/homo-junction-silicon tandem solar cell with over 20% efficiency*. Energy & Environmental Science **2018,** 11, 2432-2443.

237.   Hörantner, M. T.; Leijtens, T.; Ziffer, M. E.; Eperon, G. E.; Christoforo, M. G.; McGehee, M. D.; Snaith, H. J., *The potential of multijunction perovskite solar cells*. ACS Energy Letters **2017,** 2, 2506-2513.

238.   Vatansever, D.; Siores, E.; Shah, T., *Alternative resources for renewable energy: piezoelectric and photovoltaic smart structures*. Global warming–impacts and future perspective **2012,** 263.

239.   Peters, I. M.; Sofia, S.; Mailoa, J.; Buonassisi, T., *Techno-economic analysis of tandem photovoltaic systems*. RSC Advances **2016,** 6, 66911-66923.

240.   Basore, P. A., *Understanding manufacturing cost influence on future trends in silicon photovoltaics*. IEEE Journal of Photovoltaics **2014,** 4, 1477-1482.

241.   Essig, S.; Steiner, M. A.; Allebe, C.; Geisz, J. F.; Paviet-Salomon, B.; Ward, S.; Descoeudres, A.; LaSalvia, V.; Barraud, L.; Badel, N., *Realization of GaInP/Si dual-junction solar cells with 29.8% 1-sun efficiency*. IEEE Journal of Photovoltaics **2016,** 6, 1012-1019.

242.   Grassman, T. J.; Carlin, A. M.; Grandal, J.; Ratcliff, C.; Yang, L.; Mills, M. J.; Ringel, S. A. In *Spectrum-optimized Si-based III-V multijunction photovoltaics*, Proc. SPIE, 2012; pp 82560R-82560R.

243.   Essig, S.; Benick, J.; Schachtner, M.; Wekkeli, A.; Hermle, M.; Dimroth, F., *Wafer-bonded GaInP/GaAs//Si solar cells with 30% efficiency under concentrated sunlight*. IEEE Journal of Photovoltaics **2015,** 5, 977-981.

244.   Hau, S. K.; Yip, H.-L.; Chen, K.-S.; Zou, J.; Jen, A. K.-Y., *Solution processed inverted tandem polymer solar cells with self-assembled monolayer modified interfacial layers*. Applied Physics Letters **2010,** 97, 253307.

245.   Chang, C.-Y.; Zuo, L.; Yip, H.-L; Li, Y.; Li, C.-Z.; Hsu, C.-S.; Cheng, Y.-J.; Chen, H.; Jen, A. K. Y., *A Versatile Fluoro-Containing Low-Bandgap Polymer for Efficient Semitransparent and Tandem Polymer Solar Cells*. Advanced Functional Materials **2013,** 23, 5084-5090.

246.   Chen, C.-C.; Chang, W.-H.; Yoshimura, K.; Ohya, K.; You, J.; Gao, J.; Hong, Z.; Yang, Y., *An Efficient Triple-Junction Polymer Solar Cell Having a Power Conversion Efficiency Exceeding 11%*. Advanced Materials **2014,** 26, 5670-5677.

247.   You, J.; Dou, L.; Yoshimura, K.; Kato, T.; Ohya, K.; Moriarty, T.; Emery, K.; Chen, C.-C.; Gao, J.; Li, G., et al., *A polymer tandem solar cell with 10.6% power conversion efficiency*. **2013,** 4, 1446.

248.   Li, W.; Furlan, A.; Hendriks, K. H.; Wienk, M. M.; Janssen, R. A. J., *Efficient Tandem and Triple-Junction Polymer Solar Cells*. Journal of the American Chemical Society **2013,** 135, 5529-5532.

249.   Boland, P.; Lee, K.; Dean, J.; Namkoong, G., *Design of organic tandem solar cells using low- and high-bandgap polymer:fullerene composites*. Solar Energy Materials and Solar Cells **2010,** 94, 2170-2175.

250.   Sista, S.; Park, M.-H.; Hong, Z.; Wu, Y.; Hou, J.; Kwan, W. L.; Li, G.; Yang, Y., *Highly Efficient Tandem Polymer Photovoltaic Cells*. Advanced Materials **2010,** 22, 380-383.

251.   Puetz, A.; Steiner, F.; Mescher, J.; Reinhard, M.; Christ, N.; Kutsarov, D.; Kalt, H.; Lemmer, U.; Colsmann, A., *Solution processable, precursor based zinc oxide buffer layers for 4.5% efficient organic tandem solar cells*. Organic Electronics **2012,** 13, 2696-2701.

252.   Zhang, K.; Gao, K.; Xia, R.; Wu, Z.; Sun, C.; Cao, J.; Qian, L.; Li, W.; Liu, S.; Huang, F., et al., *High-Performance Polymer Tandem Solar Cells Employing a New n-Type Conjugated Polymer as an Interconnecting Layer*. Advanced Materials **2016,** 28, 4817-4823.

253.	Martinez-Otero, A.; Liu, Q.; Mantilla-Perez, P.; Bajo, M. M.; Martorell, J., *An extremely thin and robust interconnecting layer providing 76% fill factor in a tandem polymer solar cell architecture*. *Journal of Materials Chemistry A* **2015,** 3, 10681-10686.

254.	Zuo, L.; Chang, C.-Y.; Chueh, C.-C.; Zhang, S.; Li, H.; Jen, A. K. Y.; Chen, H., *Design of a versatile interconnecting layer for highly efficient series-connected polymer tandem solar cells*. *Energy & Environmental Science* **2015,** 8, 1712-1718.

255.	Jiang, F.; Liu, T.; Luo, B.; Tong, J.; Qin, F.; Xiong, S.; Li, Z.; Zhou, Y., *A two-terminal perovskite/perovskite tandem solar cell*. *Journal of Materials Chemistry A* **2016,** 4, 1208-1213.

256.	Chen, C.-C.; Bae, S.-H.; Chang, W.-H.; Hong, Z.; Li, G.; Chen, Q.; Zhou, H.; Yang, Y., *Perovskite/polymer monolithic hybrid tandem solar cells utilizing a low-temperature, full solution process*. *Materials Horizons* **2015,** 2, 203-211.

257.	Mailoa, J. P.; Bailie, C. D.; Johlin, E. C.; Hoke, E. T.; Akey, A. J.; Nguyen, W. H.; McGehee, M. D.; Buonassisi, T., *A 2-terminal perovskite/silicon multijunction solar cell enabled by a silicon tunnel junction*. *Applied Physics Letters* **2015,** 106, 121105.

258.	Bailie, C. D.; Christoforo, M. G.; Mailoa, J. P.; Bowring, A. R.; Unger, E. L.; Nguyen, W. H.; Burschka, J.; Pellet, N.; Lee, J. Z.; Gratzel, M., et al., *Semi-transparent perovskite solar cells for tandems with silicon and CIGS*. *Energy & Environmental Science* **2015,** 8, 956-963.

259.	Loper, P.; Moon, S.-J.; Martin de Nicolas, S.; Niesen, B.; Ledinsky, M.; Nicolay, S.; Bailat, J.; Yum, J.-H.; De Wolf, S.; Ballif, C., *Organic-inorganic halide perovskite/crystalline silicon four-terminal tandem solar cells*. *Physical Chemistry Chemical Physics* **2015,** 17, 1619-1629.

260.	Bush, K. A.; Palmstrom, A. F.; Zhengshan, J. Y.; Boccard, M.; Cheacharoen, R.; Mailoa, J. P.; McMeekin, D. P.; Hoye, R. L.; Bailie, C. D.; Leijtens, T., *23.6%-efficient monolithic perovskite/silicon tandem solar cells with improved stability*. *Nature Energy* **2017,** 2, 17009.

261.	Crisp, R. W.; Pach, G. F.; Kurley, J. M.; France, R. M.; Reese, M. O.; Nanayakkara, S. U.; MacLeod, B. A.; Talapin, D. V.; Beard, M. C.; Luther, J. M., *Tandem Solar Cells from Solution-Processed CdTe and PbS Quantum Dots Using a ZnTe–ZnO Tunnel Junction*. *Nano Letters* **2017,** 17, 1020-1027.

262.	Zhang, Y.; Gu, M.; Li, N.; Xu, Y.; Ling, X.; Wang, Y.; Zhou, S.; Li, F.; Yang, F.; Ji, K., *Realizing solution-processed monolithic PbS QDs/perovskite tandem solar cells with high UV stability*. *Journal of Materials Chemistry A* **2018,** 6, 24693-24701.

263.	Bi, Y.; Pradhan, S.; Akgul, M. Z.; Gupta, S.; Stavrinadis, A.; Wang, J.; Konstantatos, G., *Colloidal quantum dot tandem solar cells using chemical vapor deposited graphene as an atomically thin intermediate recombination layer*. *ACS Energy Letters* **2018,** 3, 1753-1759.

264.	Sargent, E. H., *Infrared photovoltaics made by solution processing*. *Nat Photon* **2009,** 3, 325-331.

265.	Henry, C. H., *Limiting efficiencies of ideal single and multiple energy gap terrestrial solar cells*. *Journal of Applied Physics* **1980,** 51, 4494-4500.

266.	Brown, A. S.; Green, M. A., *Detailed balance limit for the series constrained two terminal tandem solar cell*. *Physica E: Low-dimensional Systems and Nanostructures* **2002,** 14, 96-100.

267.	Tong, J.; Yang, X.; Xu, Y.; Li, W.; Tang, J.; Song, H.; Zhou, Y., *Efficient Top-Illuminated Organic-Quantum Dots Hybrid Tandem Solar Cells with Complementary Absorption*. *ACS Photonics* **2017,** 4, 1172-1177.

268.	Kim, T.; Gao, Y.; Hu, H.; Yan, B.; Ning, Z.; Jagadamma, L. K.; Zhao, K.; Kirmani, A. R.; Eid, J.; Adachi, M. M., et al., *Hybrid tandem solar cells with depleted-heterojunction quantum dot and polymer bulk heterojunction subcells*. *Nano Energy* **2015,** 17, 196-205.

269.	Speirs, M.; Groeneveld, B.; Protesescu, L.; Piliego, C.; Kovalenko, M.; Loi, M., *Hybrid inorganic–organic tandem solar cells for broad absorption of the solar spectrum*. *Physical Chemistry Chemical Physics* **2014,** 16, 7672-7676.

270.	Aqoma, H.; Azmi, R.; Oh, S.-H.; Jang, S.-Y., *Solution-processed colloidal quantum dot/organic hybrid tandem photovoltaic devices with 8.3% efficiency*. *Nano Energy* **2017,** 31, 403-409.

271.   Kim, T.; Palmiano, E.; Liang, R.-Z.; Hu, H.; Murali, B.; Kirmani, A. R.; Firdaus, Y.; Gao, Y.; Sheikh, A.; Yuan, M., *Hybrid tandem quantum dot/organic photovoltaic cells with complementary near infrared absorption*. *Applied Physics Letters* **2017,** 110, 223903.

272.   Gong, X.; Yang, Z.; Walters, G.; Comin, R.; Ning, Z.; Beauregard, E.; Adinolfi, V.; Voznyy, O.; Sargent, E. H., *Highly efficient quantum dot near-infrared light-emitting diodes*. *Nature Photonics* **2016,** 10, 253-257.

273.   Kwak, J.; Bae, W. K.; Lee, D.; Park, I.; Lim, J.; Park, M.; Cho, H.; Woo, H.; Yoon, D. Y.; Char, K., et al., *Bright and efficient full-color colloidal quantum dot light-emitting diodes using an inverted device structure*. *Nano Lett* **2012,** 12, 2362-2366.

274.   Wood, V.; Panzer, M. J.; Chen, J.; Bradley, M. S.; Halpert, J. E.; Bawendi, M. G.; Bulović, V., *Inkjet-Printed Quantum Dot-Polymer Composites for Full-Color AC-Driven Displays*. *Advanced Materials* **2009,** 21, 2151-2155.

275.   Konstantatos, G.; Howard, I.; Fischer, A.; Hoogland, S.; Clifford, J.; Klem, E.; Levina, L.; Sargent, E. H., *Ultrasensitive solution-cast quantum dot photodetectors*. *Nature* **2006,** 442, 180-183.

276.   Lee, J.-S.; Kovalenko, M. V.; Huang, J.; Chung, D. S.; Talapin, D. V., *Band-like transport, high electron mobility and high photoconductivity in all-inorganic nanocrystal arrays*. *Nature Nanotechnology* **2011,** 6, 348.

277.   Ip, A. H.; Thon, S. M.; Hoogland, S.; Voznyy, O.; Zhitomirsky, D.; Debnath, R.; Levina, L.; Rollny, L. R.; Carey, G. H.; Fischer, A., et al., *Hybrid passivated colloidal quantum dot solids*. *Nature Nanotechnology* **2012,** 7, 577.

278.   Kim, G.-H.; García de Arquer, F. P.; Yoon, Y. J.; Lan, X.; Liu, M.; Voznyy, O.; Yang, Z.; Fan, F.; Ip, A. H.; Kanjanaboos, P., et al., *High-Efficiency Colloidal Quantum Dot Photovoltaics via Robust Self-Assembled Monolayers*. *Nano Letters* **2015,** 15, 7691-7696.

279.   Kim, Y.; Bicanic, K.; Tan, H.; Ouellette, O.; Sutherland, B. R.; Garcia de Arquer, F. P.; Jo, J. W.; Liu, M.; Sun, B.; Liu, M., et al., *Nanoimprint-Transfer-Patterned Solids Enhance Light Absorption in Colloidal Quantum Dot Solar Cells*. *Nano Lett* **2017,** 17, 2349-2353.

280.   Chuang, C.-H. M.; Brown, P. R.; Bulović, V.; Bawendi, M. G., *Improved performance and stability in quantum dot solar cells through band alignment engineering*. *Nature Materials* **2014,** 13, 796.

281.   Havid, A.; Muhibullah, A. M.; Tantyo, H. W.; Eun‐Hye, L.; Tae‐Wook, K.; Kyu, A. T.; Seung‐Hwan, O.; Sung‐Yeon, J., *High‐Efficiency Photovoltaic Devices using Trap‐Controlled Quantum‐Dot Ink prepared via Phase‐Transfer Exchange*. *Advanced Materials* **2017,** 29, 1605756.

282.   Maraghechi, P.; Labelle, A. J.; Kirmani, A. R.; Lan, X.; Adachi, M. M.; Thon, S. M.; Hoogland, S.; Lee, A.; Ning, Z.; Fischer, A., et al., *The Donor–Supply Electrode Enhances Performance in Colloidal Quantum Dot Solar Cells*. *ACS Nano* **2013,** 7, 6111-6116.

283.   H., C. G.; Larissa, L.; Riccardo, C.; Oleksandr, V.; H., S. E., *Record Charge Carrier Diffusion Length in Colloidal Quantum Dot Solids via Mutual Dot‐To‐Dot Surface Passivation*. *Advanced Materials* **2015,** 27, 3325-3330.

284.   Xinzheng, L.; Oleksandr, V.; Amirreza, K.; Pelayo, G. d. A. F.; Saud, A. A.; Gi‐Hwan, K.; Mengxia, L.; Zhenyu, Y.; Grant, W.; Jixian, X., et al., *Passivation Using Molecular Halides Increases Quantum Dot Solar Cell Performance*. *Advanced Materials* **2016,** 28, 299-304.

285.   Tang, J.; Liu, H.; Zhitomirsky, D.; Hoogland, S.; Wang, X.; Furukawa, M.; Levina, L.; Sargent, E. H., *Quantum junction solar cells*. *Nano Lett* **2012,** 12, 4889-4894.

286.   Shao, S.; Zheng, K.; Pullerits, T.; Zhang, F., *Enhanced performance of inverted polymer solar cells by using poly(ethylene oxide)-modified ZnO as an electron transport layer*. *ACS Appl Mater Interfaces* **2013,** 5, 380-385.

287.   Ehrler, B.; Musselman, K. P.; Böhm, M. L.; Morgenstern, F. S. F.; Vaynzof, Y.; Walker, B. J.; MacManus-Driscoll, J. L.; Greenham, N. C., *Preventing Interfacial Recombination in Colloidal Quantum Dot Solar Cells by Doping the Metal Oxide*. *ACS Nano* **2013,** 7, 4210-4220.

288.   Ha, Y. E.; Jo, M. Y.; Park, J.; Kang, Y.-C.; Yoo, S. I.; Kim, J. H., *Inverted Type Polymer Solar Cells with Self-Assembled Monolayer Treated ZnO*. *The Journal of Physical Chemistry C* **2013,** 117, 2646-2652.

289.   Jo, S. B.; Lee, J. H.; Sim, M.; Kim, M.; Park, J. H.; Choi, Y. S.; Kim, Y.; Ihn, S.-G.; Cho, K., *High Performance Organic Photovoltaic Cells Using Polymer-Hybridized ZnO Nanocrystals as a Cathode Interlayer*. *Advanced Energy Materials* **2011,** 1, 690-698.

290.   Ratcliff, E. L.; Zacher, B.; Armstrong, N. R., *Selective Interlayers and Contacts in Organic Photovoltaic Cells*. *The Journal of Physical Chemistry Letters* **2011,** 2, 1337-1350.

291.   Hau, S. K.; Yip, H.-L.; Baek, N. S.; Zou, J.; O'Malley, K.; Jen, A. K.-Y., *Air-stable inverted flexible polymer solar cells using zinc oxide nanoparticles as an electron selective layer*. *Applied Physics Letters* **2008,** 92, 253301.

292.   White, M. S.; Olson, D. C.; Shaheen, S. E.; Kopidakis, N.; Ginley, D. S., *Inverted bulk-heterojunction organic photovoltaic device using a solution-derived ZnO underlayer*. *Applied Physics Letters* **2006,** 89, 143517.

293.   Steim, R.; Choulis, S. A.; Schilinsky, P.; Brabec, C. J., *Interface modification for highly efficient organic photovoltaics*. *Applied Physics Letters* **2008,** 92, 093303.

294.   Hau, S. K.; Yip, H.-L.; Ma, H.; Jen, A. K.-Y., *High performance ambient processed inverted polymer solar cells through interfacial modification with a fullerene self-assembled monolayer*. *Applied Physics Letters* **2008,** 93, 233304.

295.   Seo, J. H.; Gutacker, A.; Sun, Y.; Wu, H.; Huang, F.; Cao, Y.; Scherf, U.; Heeger, A. J.; Bazan, G. C., *Improved High-Efficiency Organic Solar Cells via Incorporation of a Conjugated Polyelectrolyte Interlayer*. *Journal of the American Chemical Society* **2011,** 133, 8416-8419.

296.   Gadisa, A.; Liu, Y.; Samulski, E. T.; Lopez, R., *Minimizing interfacial losses in inverted organic solar cells comprising Al-doped ZnO*. *Applied Physics Letters* **2012,** 100, 253903.

297.   Yoshinori, K.; Tsuyoshi, A.; Katsuhiko, F., *Cathode buffer composed of fullerene–ethylenediamine adduct for an organic solar cell*. *Japanese Journal of Applied Physics* **2017,** 56, 021601.

298.   Randi, A.; Havid, A.; Tantyo, H. W.; Jin‐Mun, Y.; Soyeon, Y.; Kyungkon, K.; Rag, D. Y.; Seung‐Hwan, O.; Sung‐Yeon, J., *Low‐Temperature‐Processed 9% Colloidal Quantum Dot Photovoltaic Devices through Interfacial Management of p−n Heterojunction*. *Advanced Energy Materials* **2016,** 6, 1502146.

299.   Jagadamma, L. K.; Abdelsamie, M.; El Labban, A.; Aresu, E.; Ngongang Ndjawa, G. O.; Anjum, D. H.; Cha, D. K.; Beaujuge, P.; Amassian, A., *Efficient inverted bulk-heterojunction solar cells from low-temperature processing of amorphous ZnO buffer layers*. *Journal of Materials Chemistry A*.

300.   Sai, B.; Yizheng, J.; Xiaoyong, L.; Zhizhen, Y.; Zhongwei, W.; Baoquan, S.; Zaifei, M.; Zheng, T.; Jianpu, W.; Uli, W., et al., *Ethanedithiol Treatment of Solution‐Processed ZnO Thin Films: Controlling the Intragap States of Electron Transporting Interlayers for Efficient and Stable Inverted Organic Photovoltaics*. *Advanced Energy Materials* **2015,** 5, 1401606.

301.   H., R. P.; Sehoon, C.; Marcus, C. C. H.; Weon, H. G.; G., B. M.; Silvija, G., *Enhanced Photocurrent in PbS Quantum Dot Photovoltaics via ZnO Nanowires and Band Alignment Engineering*. *Advanced Energy Materials* **2016,** 6, 1600848.

302.   Mengxia, L.; García, d. A. F. P.; Yiying, L.; Xinzheng, L.; Gi‐Hwan, K.; Oleksandr, V.; Krishnan, J. L.; Saud, A. A.; Sjoerd, H.; Zhenghong, L., et al., *Double‐Sided Junctions Enable High‐Performance Colloidal‐Quantum‐Dot Photovoltaics*. *Advanced Materials* **2016,** 28, 4142-4148.

303.   Z., H. R. L.; Bruno, E.; L., B. M.; David, M. R.; M., A. R.; Y., A. A.; Yana, V.; Aditya, S.; Giorgio, E.; C., G. N., et al., *Improved Open‐Circuit Voltage in ZnO−PbSe Quantum Dot Solar Cells by Understanding and Reducing Losses Arising from the ZnO Conduction Band Tail*. *Advanced Energy Materials* **2014,** 4, 1301544.

304.   Correa Baena, J. P.; Steier, L.; Tress, W.; Saliba, M.; Neutzner, S.; Matsui, T.; Giordano, F.; Jacobsson, T. J.; Srimath Kandada, A. R.; Zakeeruddin, S. M., et al., *Highly efficient planar perovskite solar cells through band alignment engineering*. *Energy & Environmental Science* **2015,** 8, 2928-2934.

305. Robel, I.; Kuno, M.; Kamat, P. V., *Size-Dependent Electron Injection from Excited CdSe Quantum Dots into TiO2 Nanoparticles*. *Journal of the American Chemical Society* **2007,** 129, 4136-4137.

306. Choi, J.; Kim, Y.; Jo, J. W.; Kim, J.; Sun, B.; Walters, G.; Garcia de Arquer, F. P.; Quintero-Bermudez, R.; Li, Y.; Tan, C. S., et al., *Chloride Passivation of ZnO Electrodes Improves Charge Extraction in Colloidal Quantum Dot Photovoltaics*. *Adv Mater* **2017,** 29, 1702350.

307. Long, H.; Deng‐Bing, L.; Liang, G.; Hua, T.; Chao, C.; Kanghua, L.; Min, L.; Jun‐Bo, H.; Haisheng, S.; Huan, L., et al., *Graphene Doping Improved Device Performance of ZnMgO/PbS Colloidal Quantum Dot Photovoltaics*. *Advanced Functional Materials* **2016,** 26, 1899-1907.

308. Zhang, X.; Santra, P. K.; Tian, L.; Johansson, M. B.; Rensmo, H.; Johansson, E. M. J., *Highly Efficient Flexible Quantum Dot Solar Cells with Improved Electron Extraction Using MgZnO Nanocrystals*. *ACS Nano* **2017,** 11, 8478-8487.

309. Beek, W. J. E.; Wienk, M. M.; Kemerink, M.; Yang, X.; Janssen, R. A. J., *Hybrid Zinc Oxide Conjugated Polymer Bulk Heterojunction Solar Cells*. *The Journal of Physical Chemistry B* **2005,** 109, 9505-9516.

310. Liu, M.; Voznyy, O.; Sabatini, R.; García de Arquer, F. P.; Munir, R.; Balawi, Ahmed H.; Lan, X.; Fan, F.; Walters, G.; Kirmani, Ahmad R., et al., *Hybrid organic–inorganic inks flatten the energy landscape in colloidal quantum dot solids*. *Nature Materials* **2016,** 16, 258.

311. R., B. D. A.; Ratan, D.; J., K. I.; David, Z.; G., P. A. A.; Larissa, L.; Lioz, E.; Michael, G.; H., S. E., *Depleted Bulk Heterojunction Colloidal Quantum Dot Photovoltaics*. *Advanced Materials* **2011,** 23, 3134-3138.

312. Weidman, M. C.; Beck, M. E.; Hoffman, R. S.; Prins, F.; Tisdale, W. A., *Monodisperse, Air-Stable PbS Nanocrystals via Precursor Stoichiometry Control*. *ACS Nano* **2014,** 8, 6363-6371.

313. Khan, M.; Naqvi, A. H.; Ahmad, M., *Comparative study of the cytotoxic and genotoxic potentials of zinc oxide and titanium dioxide nanoparticles*. *Toxicology Reports* **2015,** 2, 765-774.

314. Long, T.; Yin, S.; Takabatake, K.; Zhnag, P.; Sato, T., *Synthesis and Characterization of ZnO Nanorods and Nanodisks from Zinc Chloride Aqueous Solution*. *Nanoscale Res Lett* **2008,** 4, 247-253.

315. Pholnaka, C.; Sirisathitkula, C.; Suwanboonb, S.; Hardinga, D. J., *Effects of Precursor Concentration and Reaction Time on Sonochemically Synthesized ZnO Nanoparticles*. *Materials Research* **2014,** 17, 405-411.

316. Zhang, Z.; Lu, X.; Wang, T.; Yan, Y.; Pan, F., *The dehydration of MgCl2· 6H2O in MgCl2· 6H2O– KCl–NH4Cl system*. *Journal of Analytical and Applied Pyrolysis* **2014,** 110, 248-253.

317. Kipcak, A.; Gurses, P.; Kunt, K.; Derun, E. M.; Piskin, S., *Magnesium Borate Synthesis by Microwave Method Using MgCl2. 6H2O and H3BO3*.

318. Ferchaud, C. J.; Zondag, H. A.; Veldhuis, J. B. J.; Boer, R. d., *Study of the reversible water vapour sorption process of MgSO4.7H2O and MgCl2.6H2O under the conditions of seasonal solar heat storage*. *Journal of Physics: Conference Series* **2012,** 395, 012069.

319. Persson, K., Materials Data on MgCl2 (SG:166) by Materials Project. ; LBNL Materials Project; Lawrence Berkeley National Lab. (LBNL), Berkeley, CA (United States): 2014.

320. Umehara, H.; Takaya, M.; Terauchi, S., *Chrome-free surface treatments for magnesium alloy*. *Surface and Coatings Technology* **2003,** 169-170, 666-669.

321. Mouanga, M.; Berçot, P.; Rauch, J. Y., *Comparison of corrosion behaviour of zinc in NaCl and in NaOH solutions. Part I: Corrosion layer characterization*. *Corrosion Science* **2010,** 52, 3984-3992.

322. Klein, J. C.; Hercules, D. M., *Surface characterization of model Urushibara catalysts*. *Journal of Catalysis* **1983,** 82, 424-441.

323. Nefedov, V. I.; Salyn, Y. V.; Leonhardt, G.; Scheibe, R., *A comparison of different spectrometers and charge corrections used in X-ray photoelectron spectroscopy*. *Journal of Electron Spectroscopy and Related Phenomena* **1977,** 10, 121-124.

324. van Dijken, A.; Meulenkamp, E. A.; Vanmaekelbergh, D.; Meijerink, A., *Influence of Adsorbed Oxygen on the Emission Properties of Nanocrystalline ZnO Particles*. *The Journal of Physical Chemistry B* **2000,** 104, 4355-4360.

325.   van Dijken, A.; Meulenkamp, E. A.; Vanmaekelbergh, D.; Meijerink, A., *The Kinetics of the Radiative and Nonradiative Processes in Nanocrystalline ZnO Particles upon Photoexcitation*. *The Journal of Physical Chemistry B* **2000,** 104, 1715-1723.

326.   V., I.; S., P.; D., G.; V., S.; K., F.; M., D., *Zinc Oxide Nanoparticles with Defects*. *Advanced Functional Materials* **2005,** 15, 1945-1954.

327.   Viezbicke, B. D.; Patel, S.; Davis, B. E.; Birnie III, D. P., *Evaluation of the Tauc method for optical absorption edge determination: ZnO thin films as a model system*. *physica status solidi (b)* **2015,** 252, 1700-1710.

328.   Hou, B.; Cho, Y.; Kim, B. S.; Hong, J.; Park, J. B.; Ahn, S. J.; Sohn, J. I.; Cha, S.; Kim, J. M., *Highly Monodispersed PbS Quantum Dots for Outstanding Cascaded-Junction Solar Cells*. *ACS Energy Lett* **2016,** 1, 834-839.

329.   Yeon, D. H.; Lee, S. M.; Jo, Y. H.; Moon, J.; Cho, Y. S., *Origin of the enhanced photovoltaic characteristics of PbS thin film solar cells processed at near room temperature*. *J. Mater. Chem. A* **2014,** 2, 20112-20117.

330.   De Vos, A., *Detailed balance limit of the efficiency of tandem solar cells*. *Journal of Physics D: Applied Physics* **1980,** 13, 839.

331.   Jiang, C.-W.; Green, M. A., *Silicon quantum dot superlattices: Modeling of energy bands, densities of states, and mobilities for silicon tandem solar cell applications*. *Journal of Applied Physics* **2006,** 99, 114902.

332.   Zheng, J.; Lau, C. F. J.; Mehrvarz, H.; Ma, F.-J.; Jiang, Y.; Deng, X.; Soeriyadi, A.; Kim, J.; Zhang, M.; Hu, L., *Large area efficient interface layer free monolithic perovskite/homo-junction-silicon tandem solar cell with over 20% efficiency*. *Energy & Environmental Science* **2018,** 11, 2432-2443.

333.   Zhitomirsky, D.; Voznyy, O.; Levina, L.; Hoogland, S.; Kemp, K. W.; Ip, A. H.; Thon, S. M.; Sargent, E. H., *Engineering colloidal quantum dot solids within and beyond the mobility-invariant regime*. *Nat Commun* **2014,** 5, 3803.

334.   Faraj, M. G., *Effect of thickness on the structural and electrical properties of spray pyrolysed lead sulfide thin films*. *American journal of condensed matter Physics* **2015,** 5, 51-55.

335.   Fu, Y.; Dinku, A. G.; Hara, Y.; Miller, C. W.; Vrouwenvelder, K. T.; Lopez, R., *Modeling photovoltaic performance in periodic patterned colloidal quantum dot solar cells*. *Optics express* **2015,** 23, A779-A790.

336.   Ahmed, R.; Zhao, L.; Mozer, A. J.; Will, G.; Bell, J.; Wang, H., *Enhanced electron lifetime of CdSe/CdS quantum dot (QD) sensitized solar cells using ZnSe core–shell structure with efficient regeneration of quantum dots*. *The Journal of Physical Chemistry C* **2015,** 119, 2297-2307.

337.   Jeong, K. S.; Tang, J.; Liu, H.; Kim, J.; Schaefer, A. W.; Kemp, K.; Levina, L.; Wang, X.; Hoogland, S.; Debnath, R., *Enhanced mobility-lifetime products in PbS colloidal quantum dot photovoltaics*. *ACS nano* **2011,** 6, 89-99.

338.   Hours, J.; Senellart, P.; Peter, E.; Cavanna, A.; Bloch, J., *Exciton radiative lifetime controlled by the lateral confinement energy in a single quantum dot*. *Physical Review B* **2005,** 71, 161306.

339.   Bacher, G.; Weigand, R.; Seufert, J.; Kulakovskii, V.; Gippius, N.; Forchel, A.; Leonardi, K.; Hommel, D., *Biexciton versus exciton lifetime in a single semiconductor quantum dot*. *Physical Review Letters* **1999,** 83, 4417.

340.   Zhang, X.; Hägglund, C.; Johansson, E. M. J., *Highly efficient, transparent and stable semitransparent colloidal quantum dot solar cells: a combined numerical modeling and experimental approach*. *Energy Environ. Sci.* **2017,** 10, 216-224.

341.   Zhang, X.; Johansson, E. M., *Reduction of charge recombination in PbS colloidal quantum dot solar cells at the quantum dot/ZnO interface by inserting a MgZnO buffer layer*. *Journal of Materials Chemistry A* **2017,** 5, 303-310.

342.   Lu, K.; Wang, Y.; Liu, Z.; Han, L.; Shi, G.; Fang, H.; Chen, J.; Ye, X.; Chen, S.; Yang, F., *High－Efficiency PbS Quantum－Dot Solar Cells with Greatly Simplified Fabrication Processing via "Solvent－Curing"*. *Advanced Materials* **2018,** 30, 1707572.

343.	Zhang, Y.; Gu, M.; Li, N.; Xu, Y.; Ling, X.; Wang, Y.; Zhou, S.; Li, F.; Yang, F.; Ji, K., et al., *Realizing solution-processed monolithic PbS QDs/perovskite tandem solar cells with high UV stability*. *Journal of Materials Chemistry A* **2018,** 6, 24693-24701.

344.	Timmreck, R.; Meyer, T.; Gilot, J.; Seifert, H.; Mueller, T.; Furlan, A.; Wienk, M. M.; Wynands, D.; Hohl-Ebinger, J.; Warta, W., *Characterization of tandem organic solar cells*. *Nature Photonics* **2015,** 9, 478-479.

345.	Bi, Y.; Pradhan, S.; Gupta, S.; Akgul, M. Z.; Stavrinadis, A.; Konstantatos, G., *Infrared Solution-Processed Quantum Dot Solar Cells Reaching External Quantum Efficiency of 80% at 1.35 microm and Jsc in Excess of 34 mA cm(-2)*. *Adv Mater* **2018,** 30.

346.	Karani, A.; Yang, L.; Bai, S.; Futscher, M. H.; Snaith, H. J.; Ehrler, B.; Greenham, N. C.; Di, D., *Perovskite/Colloidal Quantum Dot Tandem Solar Cells: Theoretical Modeling and Monolithic Structure*. *ACS Energy Letters* **2018,** 3, 869-874.

347.	Kramer, I. J.; Levina, L.; Debnath, R.; Zhitomirsky, D.; Sargent, E. H., *Solar cells using quantum funnels*. *Nano Lett* **2011,** 11, 3701-3706.

348.	Kim, J.; Ouellette, O.; Voznyy, O.; Wei, M.; Choi, J.; Choi, M. J.; Jo, J. W.; Baek, S. W.; Fan, J.; Saidaminov, M. I., *Butylamine‐Catalyzed Synthesis of Nanocrystal Inks Enables Efficient Infrared CQD Solar Cells*. *Advanced Materials* **2018**, 30, 1803830.

349.	Gao, Y.; Patterson, R.; Hu, L.; Yuan, L.; Zhang, Z.; Hu, Y.; Chen, Z.; Teh, Z. L; Conibeer, G.; Huang, S., *MgCl2 passivated ZnO electron transporting layer to improve PbS quantum dot solar cells*. *Nanotechnology* **2018,** 30, 085403.

350.	Chuang, C.-H. M.; Brown, P. R.; Bulović, V.; Bawendi, M. G., *Improved performance and stability in quantum dot solar cells through band alignment engineering*. *Nat Mater* **2014,** 13, 796-801.